Internal Waves in the Western Arctic Ocean

Hayley V. Dosser

A dissertation
submitted in partial fulfillment of the
requirements for the degree of

Doctor of Philosophy

University of Washington

2015

Reading Committee:

Luc Rainville, Chair

Rebecca Woodgate

Eric Kunze

Program Authorized to Offer Degree:
University of Washington School of Oceanography

University of Washington

Abstract

Internal Waves
in the
Western Arctic Ocean

Hayley V. Dosser

Chair of the Supervisory Committee:
Principal Oceanographer Luc Rainville
Applied Physics Laboratory

The importance of internal waves in the Western Arctic Ocean is assessed using a combination of observations from Ice-Tethered Profilers drifting in the Canada Basin between Fall 2005 and Fall 2014 and numerical simulations of internal wave propagation and stability in measured stratifications typical of the Western Arctic.

The Ice-Tethered Profiler dataset provides the first decade-long record, with broad spatial coverage, for the near-inertial internal wave field in the Arctic Ocean. Since the Ice-Tethered Profiler sampling pattern only marginally resolves the near-inertial frequency, complex demodulation is used to estimate wave amplitudes from vertical isopycnal displacements.

Using this technique, a seasonal cycle in average near-inertial wave vertical displacement amplitude is identified for the upper ocean. Waves are largest during summer when sea-ice extent and speed are at a minimum, with a second peak in early winter associated with strong storms. Seasonal variations in wave amplitude are connected to changes in sea-ice properties that affect how readily the ice responds to wind forcing.

In addition to seasonal variability, near-inertial wave amplitude has a slight increasing trend paralleling the decline in sea-ice extent over the last decade. Variance in the distribution of wave amplitudes doubled between 2005-2007 and 2012-2014, with larger-than-average waves generated more frequently in both summer and winter.

Numerical solutions for the vertical structure of internal waves propagating through observed stratification profiles from the Canada Basin indicate that the double-diffusive staircase within the Atlantic Water layer significantly modifies the internal wave field, causing reflection for discrete vertical wavenumber bands and amplifying wave energy at depths where constructive interference occurs.

Near-inertial internal waves of average amplitude are predicted to be stable within the Atlantic Water layer, but the fraction of larger-than-average waves that are potentially shear unstable has more than doubled over the last decade. An increase in episodic internal wave mixing events is predicted in the Canada Basin. The internal wave field in the Western Arctic Ocean will likely continue to evolve as sea-ice extent and thickness decline, and multiyear ice is replaced by first-year ice.

TABLE OF CONTENTS

LIST OF FIGURES

LIST OF TABLES

ACKNOWLEDGMENTS

This work would not have been possible without the guidance and support of my advisor, Luc Rainville. I want to thank him for taking me on as his first graduate student, and for the many challenges and opportunities he has provided me, both at sea and on land.

I would like to thank my committee members: Rebecca Woodgate, Eric Kunze, Parker MacCready, Jody Deming and Jim Thomson, for their time, helpful suggestions, and interest in my research. Particular thanks to my reading committee, whose constructive criticism has greatly improved this thesis.

Special thanks to my graduate cohort, all of whom I now count as friends: Cynthia Travers, Jamie Shutta, Jacob Wenegrat, John Guthrie, Melinda Webster, and especially Andrew Shao, who is amazing in so many ways.

Last but certainly not least, I want to thank my family for their patience, love, and endless support. My sister Alexandra, my grandmother Mildred, and most especially my mother Patricia, who is the reason I became a scientist, and who has never stopped believing in me.

DEDICATION

to Ryan and Andrew, for being there

Chapter 1
INTRODUCTION

The overall goal of my PhD research is to assess the importance of internal waves in the Western Arctic Ocean; to determine how the internal wave field varies spatially and temporally and where the energy transported by surface generated internal waves ultimately ends up.

1.1 Internal wave basics

Internal waves are oscillatory disturbances in stably stratified fluid, in which the density of the fluid varies with depth due to changes in salinity or temperature. Internal waves propagate both horizontally and vertically, transporting energy through the fluid, which is deposited at the location of wave breaking or dissipation. Internal waves are restricted to frequencies in a range between the Brunt-Väisälä or buoyancy frequency N - the natural frequency of oscillation of the stratified fluid - and the Coriolis or inertial frequency f - the resonant planetary frequency. An internal wave with a frequency $\omega \approx N$ causes oscillations within the fluid at a slight angle to the vertical, as fluid is displaced due to a combination of buoyancy and gravity forces.

Internal waves near the inertial frequency, $\omega \approx f$, known as near-inertial waves, are additionally affected by the Earth's rotation. Purely inertial motion is horizontal rotation in circles caused by the Coriolis force. Near-inertial internal wave motion occurs in tilted ellipses at a slight angle to the horizontal, with slow vertical propagation through the fluid. Near-inertial waves are primarily wind generated, and these surface-generated waves rotate clockwise in the Northern Hemisphere. The near-inertial frequency band, $f < \omega \leq 1.1f$, has

been shown to contain most of the variance in the wind-generated internal wave spectrum (Garrett and Munk, 1972; Garrett, 2001), making near-inertial waves particularly important to oceanic energy transport.

The local inertial frequency increases with latitude, with the inertial period approaching 12 hours in the Arctic. Since internal waves cannot propagate freely if their frequency falls below the local inertial frequency (provided $N > f$), near-inertial waves are generally restricted from propagating poleward. In the Arctic Ocean, near-inertial internal waves have horizontal wavelengths on the order of 10-100km, vertical wavelengths on the order of 10-100m, and horizontal velocities of a few centimeters per second (Pinkel, 2005, 2008; Cole et al., 2014).

1.2 Global relevance of internal waves

Ocean internal waves are important globally due to their role in transporting energy from the winds and tides - both vertically into the ocean interior and horizontally across ocean basins. When these internal waves dissipate or cause mixing as they overturn and break, their energy is transferred to smaller scales.

The large-scale ocean circulation requires small-scale mixing to vertically transport heat to the cold, dense water in the abyssal ocean, allowing upwelling towards the surface, in order to balance the sinking of dense near-surface water at high latitudes (Wunsch and Ferrari, 2004). The total estimated energy required is roughly 2TW (Munk, 1966; Munk and Wunsch, 1998), with about 1TW each from the tides and the wind.

The diffusivity associated with the required energy transport is about 10^{-4} m^2/s (Munk and Wunsch, 1998). Observed diffusivities due to internal wave breaking are typically in the range 10^{-5} m^2/s to 10^{-4} m^2/s (Gregg, 1989; Waterhouse et al., 2014), with higher values found at 'hot spots' such as regions of rough topography where tidal flow generates energetic internal waves (e.g.: Garrett and Kunze (2007)).

In the majority of the world's oceans, wind generated near-inertial waves carry significant energy from wind forcing, particularly winter storms, (D'Asaro et al., 1995) vertically

downward into the ocean interior. Wind generation of near-inertial waves occurs when wind stress resonantly forces the air-water (or air-ice) interface at or near the inertial frequency, which is the frequency most efficient at transferring energy. In the Northern Hemisphere, the Coriolis force acts to displace fluid to the right, therefore anti-cyclonic or clockwise inertial oscillations are set up in the mixed layer. These purely horizontal inertial oscillations create disturbances at the base of the mixed layer, generating a freely propagating near-inertial wave in the stratified water column below (D'Asaro, 1985).

Globally, wind driven near-inertial currents in the mixed layer are estimated to contain 0.3-1.4TW of energy available to generate downward propagating internal waves (Alford et al., 2012), suggesting that near-inertial waves may be an important consideration in the global energy budget. The mixing caused when these waves break is episodic and spatially variable (Alford, 2003), vertically transporting heat, salt, and nutrients.

1.3 Arctic internal wave history

The earliest investigation of Arctic internal waves was likely by Ekman (1905), who hypothesized that the 'dead water' encountered by Nansen's Arctic expedition in 1883 on the Fram was a result of internal waves generated by the ship's passage, carrying energy away and limiting the ship's forward motion. Observations of Arctic internal waves from ice camps during the 1980s and 1990s found a quiescent Arctic Ocean with limited vertical mixing (e.g.: the Arctic Internal Waves Experiment, AIWEX Spring 1985 - Levine et al. (1987); D'Asaro and Morehead (1991); Merrifield and Pinkel (1996), and the Surface Heat Budget of the Arctic experiment, SHEBA 1997-1998 - Pinkel (2005)). The energy level of the observed internal wave field is an order of magnitude or more below that at lower latitudes (Levine et al., 1985, 1987), with diffusivities closer to 10^{-6} m^2/s (Rainville and Winsor, 2008; Fer, 2009), consistent with the diffusivity necessary to produce the observed Arctic Ocean stratification (Steele et al., 2001; Zhang and Steele, 2007).

Within the main Arctic basins, internal wave energy levels are lower in part due to weak tidal forcing and the lack of a freely propagating internal tide. Tidally forced internal waves

are generated when the barotropic tide sloshes back and forth over topographic features, launching upward propagating internal wave beams at the tidal frequency. The M2 and S2 semi-diurnal tidal frequencies in the Arctic fall within the near-inertial band, making internal tides difficult to distinguish from wind-generated near-inertial waves. However, the majority of the Arctic Ocean lies north of the critical latitude for the dominant semi-diurnal lunar M2 tide (74.5^oN), so that internal tides cannot propagate freely, and dissipate locally (Simmons et al., 2004). Localized topographic mixing associated with internal tides may be important (D'Asaro and Morison, 1992; Fer et al., 2010; Lenn et al., 2011), but likely occurs primarily at isolated topographic 'hot spots' far from the interior of the main Arctic basins.

Low internal wave energy levels in the Arctic are also attributed to the influence of sea-ice cover. Sea ice acts as a barrier between the wind the and ocean surface, requiring wind forcing to accelerate the ice in order to generate inertial currents in the mixed layer and near-inertial waves in the stratified water column below. Sea ice may also limit momentum transfer from wind forcing to the internal wave field by acting as a rigid lid on the water column below and thus reducing vertical oscillations (Plueddemann et al., 1998), although this assumes a rigid, nearly immobile ice pack. Dissipation of internal waves in the turbulent boundary layer under the sea ice may limit internal wave propagation across the Arctic by preventing internal wave reflection from the sea ice, and reducing energy transfer into the ocean interior (Morison et al., 1985; Pinkel, 2005).

1.4 Arctic internal wave generation

Near-inertial waves in the Arctic are generated by wind forcing on open water or on sea ice, with the resulting motion leading to inertial currents in the mixed layer. Horizontal variations in velocity cause convergence and divergence within the mixed layer at the inertial frequency, which drives vertical 'inertial pumping' at the base of the mixed layer and excites internal waves in the stratified water column below.

Wind forcing drives clockwise inertial rotation of sea-ice floes and spatially inhomogeneous sub-inertial ice drift. The rough bottom of the ice can impulsively force the water

column, with horizontal variations in bottom roughness that result in a pattern of forcing moving at the ice velocity (D'Asaro and Morehead, 1991; McPhee and Kantha, 1989). Ice motion generates inertial currents in the mixed layer, with impulse or sub-inertial forcing also generating motion at frequencies in the inertial range, but less efficiently than continual forcing of the mixed layer by wind or ice motion at the inertial frequency.

Momentum transfer between the wind and sea ice, and between the ice and ocean, depends critically on the properties of the sea ice, which may include its extent, thickness, age, roughness, and ability to deform. Thin, patchy first-year ice, with large melt ponds and areas of open water, will move very differently in response to wind forcing than will thick, rigid multiyear ice, rafted into large ridges, with high internal ice stress.

1.5 Changing Arctic conditions

During the last decades, conditions in the Arctic Ocean have changed dramatically, with significant reductions in sea-ice area and volume. The decline in sea ice has accelerated during the last decade in particular, with sharp decreases in summer extent (Serreze et al., 2007; Stroeve et al., 2012), overall ice thickness (Rothrock et al., 2008; Lindsay and Schweiger, 2015), and ice age, as multiyear ice has melted out (Comiso, 2002). In the Western Arctic, the ice pack has evolved from perennially ice-covered with predominantly thick, multiyear ice to seasonally ice free with extensive regions of thin, weak, first-year ice.

Ice motion is influenced by internal ice stress, and air-ice and ice-ocean drag, which are themselves affected by ice extent, thickness, and deformation (Hakkinen et al., 2008). As the characteristics of the sea ice have evolved during the last 30 years, the magnitude of inertial oscillations in the sea ice has increased (Gimbert et al., 2012a,b). Spreen et al. (2011) and Rampal et al. (2009) both observed increased sea-ice drift speeds in recent decades, and a sharp increase in ice deformation. Winter storms in the Arctic may also be increasing in frequency and intensity (Serreze et al., 1997; McCabe et al., 2001; Zhang et al., 2004), increasing the strength of the wind forcing on the sea ice, and potentially causing an increase in sea-ice drift speeds (Hakkinen et al., 2008). It has been suggested that these changes in

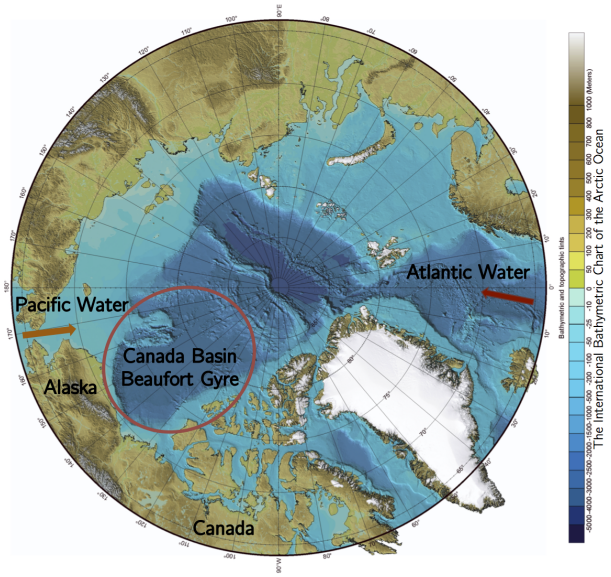

Figure 1.1: Bathymetric map of the Arctic Ocean (Jakobson and et al., 2012), with inflow of Pacific and Atlantic waters indicated. General location of the study region in the Canada Basin is circled in red.

sea-ice extent and ice motion could be causing an increase in the energy of the Arctic internal wave field, particularly during the increasingly ice-free summer months, but this has not been well quantified (Gimbert et al., 2012a; Rainville et al., 2011).

1.6 Study region

This research seeks to address, in part, how changes in Arctic conditions over the last decade have affected the near-inertial internal wave field in the Western Arctic. In particular, the study area is the Beaufort Gyre region in the Canada Basin, from roughly 72^{o}N to 82^{o}N and roughly 130^{o}W to 160^{o}W. This Basin is a smooth abyssal plain, averaging roughly 3500m deep, with the continental slope of Canada and Alaska to the south, the Canadian Arctic Archipelago to the east, and the Northwind Ridge separating it from the Chukchi to the west. The Beaufort Gyre is the main circulation feature, with large-scale atmospheric and oceanic circulation typically in the anti-cyclonic direction during the last decade.

The density stratification in the central Canada Basin is set primarily by salinity. A shallow near-surface mixed layer extends to between ∼10 m and ∼50 m depth (Toole et al., 2010), above a sharp halocline. The seasonal Near-Surface Temperature Maximum (NSTM) (Jackson et al., 2010; Steele et al., 2011) lies between the mixed layer and the local temperature maximum associated with Pacific Summer Water. At a depth of roughly 200m, the Atlantic Water layer begins, characterized by a strongly stratified halocline within which temperature and salinity increase monotonically with depth. In the Beaufort Gyre, the temperature maximum is found near 400m depth. Above the Atlantic Water temperature maximum, double-diffusive processes create a staircase-like stratification feature (Padman and Dillon, 1987, 1988, 1989) composed of multiple mixed layers, separated by thin stratified interfaces. Below this double-diffusive staircase, interleaving Atlantic water layers are created by thermohaline intrusions (Walsh and Carmack, 2003; McLaughlin et al., 2009).

1.7 Recent Arctic internal wave observations

Recent measurements of the internal wave field in the Western Arctic Ocean display seasonal variations, with more energetic waves associated with reduced sea ice. Using a mooring array on the Beaufort Continental Slope, Martini et al. (2014) observed enhanced near-inertial wave energy during ice-free and ice-forming periods, with a peak in internal wave energy during ice formation in the fall, corresponding to <90% ice concentration. Rainville and Woodgate (2009) found enhanced inertial velocity and shear during ice-free periods in the shallow Chukchi Sea. In the fall and early winter of 2009 in the Canada Basin, Cole et al. (2014) measured elevated near-inertial wave energy relative to that in late winter. However, Guthrie et al. (2013) compared historic data records with recent CTD measurements in the Beaufort Sea, and found no trend in internal wave energy over the last 30 years. Many observations in the Arctic are limited temporally (e.g. summer research cruises and short term drifting ice camps), or spatially (e.g. moorings), and rarely have the high temporal resolution and long duration required to quantify the seasonal or interannual evolution of the internal wave field.

1.8 Impacts of Arctic internal waves

1.8.1 Heat flux

Increases in internal wave energy could potentially increase mixing and dissipation rates, with implications for the vertical transport of heat and nutrients. Within the Canada Basin, the presence of a strongly stratified halocline limits vertical heat flux from the Pacific and Atlantic water layers to the mixed layer and thus the sea ice (Toole et al., 2010). The overall heat content within the Atlantic Water layer in the central Canada Basin is sufficient to completely melt the sea ice, however the presence of a double-diffusive staircase that is laterally coherent over more than 800km (Timmermans et al., 2008a) indicates extremely limited vertical mixing at those depths. In fact, the estimated vertical heat flux from the top of the Atlantic Water layer is only one tenth that from the mixed layer to the sea ice in the central Canada Basin (Timmermans et al., 2008a).

Heat flux from the Pacific Water most likely does contribute to sea-ice melt. Shimada et al. (2006) hypothesized that increased momentum transfer from wind forcing to the upper ocean in the presence of reduced or weakened sea-ice cover on the Beaufort Slope affects the large-scale circulation of Pacific Summer Water in recent years and locally increases sea-ice melt. Yang et al. (2004) found that storm-driven mixing events in the Beaufort Sea penetrate into the halocline, particularly in winter and spring when the stratification is weak, driving episodic fluxes of warm water from the thermocline to the surface. However, Peralta-Ferriz and Woodgate (2015) found correlations between wind forcing and mixed layer deepening explained only 1-20% of the variance in mixed layer depth, particularly in the Western Arctic when the near-surface is strongly stratified.

1.8.2 Nutrient transport

Biological productivity of phytoplankton and ice algae in the Western Arctic Ocean is controlled by the depth of the euphotic zone relative to the depth of the nutricline (Palmer et al., 2013). In the Canada Basin, the euphotic zone is typically 50-60m deep during summer, and

the nutricline is typically 60m deep or more. The depth of the nutricline may be increasing in the central Canada Basin, as nutrient utilization on the shelves increases and the Beaufort Gyre strengthens (McLaughlin and Carmack, 2010). The limiting nutrient in the Arctic is typically nitrogen (Tremblay and Gagnon, 2009), which is supplied by a combination of buoyancy driven winter mixing and the inflow of Pacific and Atlantic waters. Currently, the nutrient rich Pacific Water (Walsh and et al., 1989) is not experiencing persistent vertical mixing within the central Canada Basin (Woodgate et al., 2010), although it is hypothesized that intermittent mixing due to severe storms and internal waves may be important (Tremblay and Gagnon, 2009).

In Fall of 2013, in the shallow Chukchi Sea, Nishino et al. (2015) observed an increase in vertical nutrient fluxes and primary productivity during three storm events, which they attribute to a vertically displaced halocline combined with wind driven near-inertial waves causing turbulent mixing. However, in the southeast Beaufort Sea in the fall and winter of 2004, Tremblay et al. (2008) found that storm-driven mixing did not significantly increase nutrient flux to the surface, due to the strength of the halocline in that region. Ardyna et al. (2014), by contrast, found an increase in fall phytoplankton blooms in the Arctic Ocean over the last 15 years, which they link to a combination of increased open water in September and October and increased frequency and intensity of fall storms, suggesting an increase in wind-driven vertical mixing causing nutrient transport.

Any increase in mixing due to an increase in internal wave energy in the Canada Basin could affect the vertical flux of heat or nutrients, either directly or by weakening the stratification enough to permit increased storm-driven mixing. Mixing due to internal waves also has the potential to draw heat downward from the surface ocean. The implications for sea-ice melt and biological primary productivity are uncertain, but potentially significant.

This thesis investigates the changing internal wave field in the Western Arctic Ocean. This is accomplished by, first, quantifying variations in the near-inertial internal wave field spatially, seasonally, and interannually using the Ice-Tethered Profiler dataset, and connecting observed variations in wave energy to changing sea-ice conditions. The ultimate fate

of the energy transported by the internal waves is then investigated using a 1-D numerical model to assess the evolution of the waves as they propagate through the unusual stratification in the Western Arctic Ocean. This approach also allows for an assessment of internal wave stability and thus the potential for mixing at different depths.

Chapter 2

NEAR-INERTIAL INTERNAL WAVE FIELD IN THE CANADA BASIN FROM ICE-TETHERED PROFILERS

Published citation: Hayley V. Dosser, Luc Rainville, and John M. Toole, 2014: Near-Inertial Internal Wave Field in the Canada Basin from Ice-Tethered Profilers. J. Phys. Oceanogr., 44, 413426. doi: http://dx.doi.org/10.1175/JPO-D-13-0117.1

2.1 Abstract

Salinity and temperature profiles from drifting Ice-Tethered Profilers in the Beaufort Gyre region of the Canada Basin are used to characterize and quantify the regional near-inertial internal wave field over one year. Vertical displacements of potential density surfaces from

the surface to 750 m depth are tracked from Fall 2006 to Fall 2007. Due to the time resolution and irregular sampling of the Ice-Tethered Profilers, near-inertial frequency signals are marginally resolved. Complex demodulation is used to determine variations with a timescale of several days in the amplitude and phase of waves at a specified near-inertial frequency. Characteristics and variability of the wave field over the course of the year are investigated quantitatively and related to changes in surface wind forcing and sea-ice cover.

2.2 Introduction

The Arctic Ocean is undergoing rapid changes. The reduction in summer sea-ice cover in recent years (Serreze et al., 2007), coupled with an increase in ocean surface forcing by storms (Hakkinen et al., 2008), may be driving an increase in seasonal internal wave generation (Rainville et al., 2011), though this correlation has not been well quantified. As the Arctic Ocean continues to respond to a changing climate, there is an expectation of increased mixing associated with internal waves over both the shelves and in the deep basins, particularly for wind-generated motions whose frequency is close to the local inertial frequency. As such, the need for multi-year time series of internal wave activity in the Arctic is increasing.

Surface generation of internal waves in the Arctic is primarily a result of surface forcing by wind and the motion of sea ice (D'Asaro, 1985), both of which transfer momentum to the ocean surface mixed layer. This forcing results in perturbations at the base of the mixed layer and in the halocline. These density perturbations define an internal wave propagating in both the vertical and horizontal directions. Free internal waves in a resting ocean have frequencies that fall between the local inertial frequency f and the background buoyancy frequency N. Typically, there is a peak in wave energy and shear associated with near-inertial waves at the low frequency end of the spectrum: frequencies between f and roughly $1.1f$ (Garrett, 2001). These near-inertial waves have horizontal wavelengths on the order of kilometers, vertical wavelengths on the order of 10-100 m, and have been observed to dominate the internal wave field in the Arctic (Pinkel, 2005).

Previous observations of internal waves in the Arctic have been temporally as well as

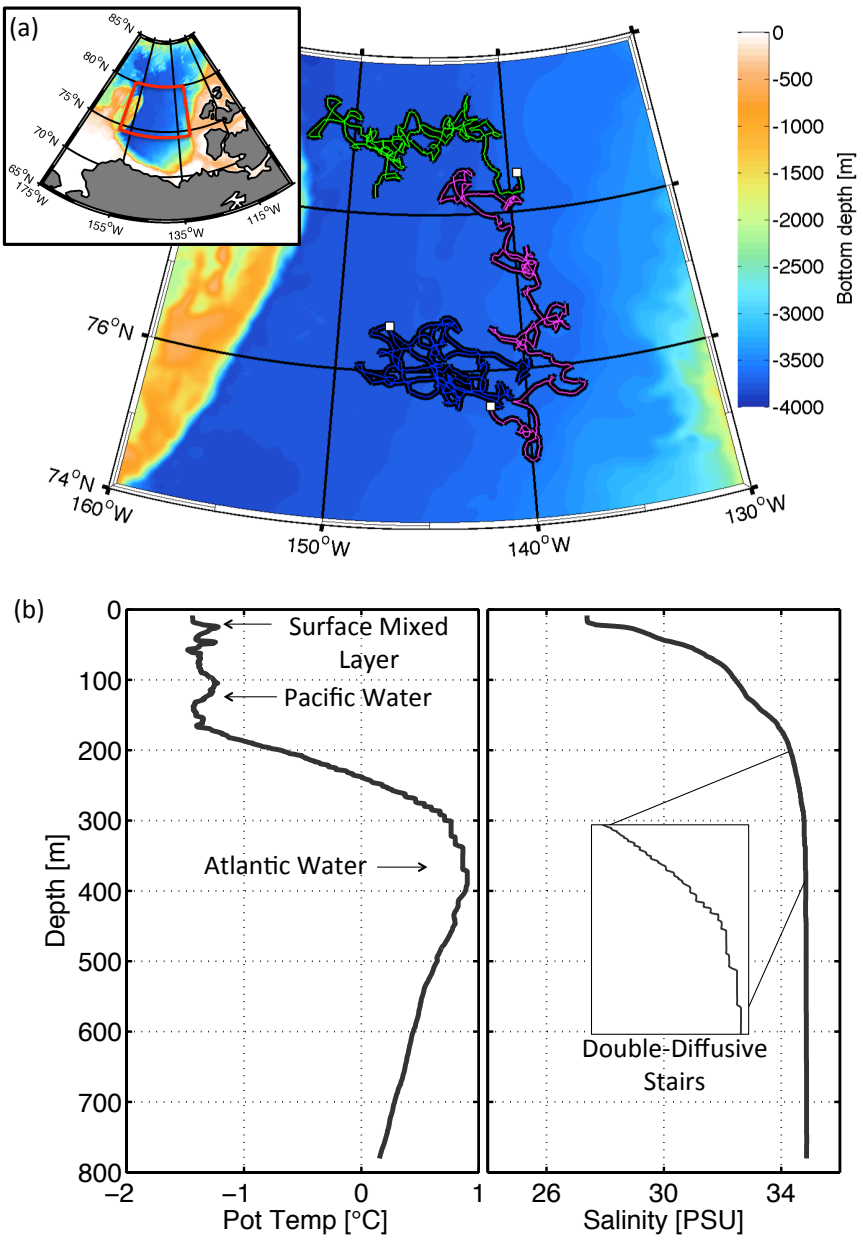

Figure 2.1: (a) Trajectories of ITP 4 (green), ITP 5 (blue), and ITP 6 (pink) in the Beaufort Gyre region (inset) of the Canada Basin from early September, 2006 to early September, 2007. White squares mark the end of each record. Colours show bathymetry. (b) Typical ITP potential temperature and salinity profiles for the Canada Basin from September 6^{th}, 2006. The double-diffusive staircase stratification extends from the top of the Atlantic layer to the Atlantic Water temperature maximum.

spatially limited, lacking year-round or multi-year time series. Observations from ice camps, such as the Arctic Internal Waves Experiment (AIWEX Spring 1985) (Levine et al., 1987; D'Asaro and Morehead, 1991; Merrifield and Pinkel, 1996) and the Surface Heat Budget of the Arctic (SHEBA 1997-1998) experiment (Pinkel, 2005) have provided information on the propagation characteristics and spectral distribution of Arctic internal waves.

Under ice cover, Arctic internal waves typically have an energy level one to two orders of magnitude lower than that seen in other oceans (Levine et al., 1985, 1987). The importance of localized topographic mixing and increased heat flux associated with the internal wave field has been highlighted by measurements from research vessels during summer cruises, such as those of D'Asaro and Morison (1992), and more recently Rainville and Winsor (2008), Fer et al. (2010), and Lenn et al. (2011). There is also the potential for mixing due to internal waves to modify the unique stratification features found in the Beaufort Gyre region, which are described in detail in Section 2.3. Current observational efforts, for example the ICORTAS moorings on the Beaufort Shelf [Personal communication; Harper Simmons and Kim Martini] and the expendable current profilers deployed near the North Pole (Guthrie et al., 2013), aim to provide temporal information about the wave field and its forcing.

The focus of the present work is the quantification of near-inertial internal wave amplitudes from Ice-Tethered Profiler (ITP) observations (Krishfield et al., 2008; Toole et al., 2011) collected in the Canada Basin region of the Arctic Ocean. The ITP instruments are moored in large ice floes, and drift with the ice throughout the year. They record vertical CTD profiles with high vertical resolution from near the ice-ocean interface to the base of the Atlantic Water layer. ITPs have collected year-round continuous time series since 2004, with data from over 60 instruments publicly available, and new instruments deployed each year (*http://www.whoi.edu/itp*). A significant number of these ITPs collected data in the Beaufort Gyre region of the Canada Basin, many as part of the Beaufort Gyre Exploration Project (*http://www.whoi.edu/beaufortgyre*). Year-round and multi-year ITP measurements with wide spatial coverage can provide a quantitative picture of the seasonality and longterm

time evolution of the internal wave field in the Arctic Ocean.

ITPs have been used to study large-scale and mesoscale properties of the Beaufort Gyre under sea-ice cover, including fresh water content and stratification changes over the past decade (Proshutinsky et al., 2009), seasonal mixed layer evolution (Toole et al., 2010), and the eddy field of the Canada Basin (Timmermans et al., 2008b). An ITP equipped with a velocity sensor has recently been deployed in the Arctic and used to estimate high frequency motions associated with internal waves (Cole et al., 2014). Most ITPs, however, only measure scalar fields and extracting the near-inertial internal wave field from a typical ITP dataset is non-trivial. The sampling schedule of the ITPs is generally not designed to capture internal waves, but rather to mostly eliminate aliasing due to motions at the semi-diurnal tidal frequency and near the inertial (or Coriolis) frequency, f, while still sampling infrequently enough to provide measurements over a year or more. The goal of this study is to demonstrate that, despite these limitations, it is possible to accurately quantify near-inertial wave properties using the existing ITP dataset. The instrument and dataset are discussed in Section 2.3, while the technique used to determine vertical displacement amplitudes associated with the near-inertial waves is described in Section 2.4. Uncertainty in the wave amplitude estimates is quantified in Section 2.5, while the resulting near-inertial wave field and connections to atmospheric forcing and sea-ice cover are presented in Section 2.6.

2.3 Data

The ITP data used herein were collected by 3 instruments, (ITP 4, ITP 5, and ITP 6), that drifted in the Beaufort Gyre region of the Canada Basin between early September 2006 and early September 2007. The region traversed by these three instruments has relatively simple bathymetry (Fig. 2.1a). ITPs are anchored in the sea ice by a surface buoy, and sample the water column from $\sim$7 m below the surface to 750 m depth. Temperature and conductivity are measured at 1 Hz by a Sea-Bird CTD, and these data are transmitted by an inductive link to a surface unit, where they are relayed to shore by the Iridium satellite system (Krishfield et al., 2008). The ITP data are mapped to a pressure grid using 1-dbar bin-averaging. While

the instrument itself remains moored in a perennial ice floe, the surrounding sea-ice cover changes seasonally, with thinner, patchier ice in the summer.

Stratification in the central Beaufort Gyre is determined primarily by salinity, with several distinct water masses (Fig. 2.1b). The near-surface mixed-layer extends from the surface to between ∼10 m and ∼50 m depth, frequently terminating in a sharp halocline, as discussed by Toole et al. (2010). Below this is the seasonal Near-Surface Temperature Maximum (NSTM) (Jackson et al., 2010; Steele et al., 2011), observed above the local temperature maximum caused by the intrusion of Pacific Summer Water (PSW). A strongly stratified halocline associated with the Atlantic Water layer begins at a depth of about 200 m, within which temperature and salinity increase monotonically with depth. In the Beaufort Gyre, the Atlantic Water temperature maximum is found near 400 m depth.

Above the Atlantic Water temperature maximum, double-diffusive processes create a staircase-like stratification profile (Timmermans et al., 2008a). The staircase is composed of multiple density layers in which both temperature and salinity are constant, separated by thin interfaces in which both temperature and salinity increase with depth. Layers can range in thickness from one meter to tens of meters. Below the double-diffusive staircase are interleaving Atlantic water layers characterized by thermohaline intrusions (Walsh and Carmack, 2003; McLaughlin et al., 2009).

The typical sampling schedule for the ITP instruments is two one-way vertical profiles per day beginning at 00:00 and at 06:00 UTC. The instrument moves vertically along the wire at approximately ∼0.25 m/s; profiles to 750 m typically take less than 1 hour. The time separation at a given depth between pairs of profiles is thus depth dependent, with samples near the surface separated by less than 6 hours, and samples at depth by more than 6 hours. This uneven sampling schedule was designed so that each pair of profiles is separated by roughly half a semi-diurnal tidal/inertial period (which are within 2% of each other in the central Arctic): a near-inertial wave crest measured at 00:00 would be followed by a wave trough at around 06:00. Within the Canada Basin, the inertial period varies between $T_f = 12.15$ hours at $80°N$ to $T_f = 12.45$ hours at $74°N$. The time-resolution from

the ITP is not sufficient to determine daily variations in the near-inertial wave field, nor to perform an accurate frequency decomposition. This paper demonstrates that it is possible, however, to use ITP data to quantify variations in the amplitude of near-inertial waves over a timescale of a few days.

2.4 Method

A linear near-inertial wave is associated with a sinusoidal vertical displacement $\eta_I(t) = A_\eta \cos(-\omega t + \phi)$, where ω is wave frequency and ϕ is phase. This signal is captured, although poorly, by most ITPs deployed to date. To obtain an estimate of the near-inertial wave amplitude $A_\eta(z,t)$, equivalent to half the maximum peak-to-trough vertical displacement, vertical displacements of isopycnals are tracked through time and a complex demodulation is performed on the sub-daily displacements. Simply taking the difference between pairs of profiles separated by $\sim$ 6 hours would result in a systematic underestimation of wave amplitudes (by 36% on average).

The total vertical displacements of the isopycnals,

$$\eta(z,t)_{tot} = \eta_{low} + \eta_I + \eta_{IWS} + \epsilon, \tag{2.1}$$

are a combination of low frequency (sub-inertial) vertical heaving, η_{low}, random noise in the data (uncertainty in isopycnal depth), ϵ, and high frequency oscillations, which can be expressed as a superposition of near-inertial internal waves, η_I, and (super-inertial) motions associated with the continuum internal wave spectrum, η_{IWS}. Plueddemann et al. (1998) noted that near-inertial oscillations dominate on timescales of less than a day. The impact of η_{IWS} and ϵ on the accuracy of the near-inertial displacement estimates is discussed in Section 2.5.

In the Canada Basin, the M_2 and S_2 tidal frequencies fall within the near-inertial band. Barotropic tides in the Beaufort Gyre are generally weak (Kowalik and Proshutinsky, 1994; Padman and Erofeeva, 2004), and are not expected to generated large internal tides, par-

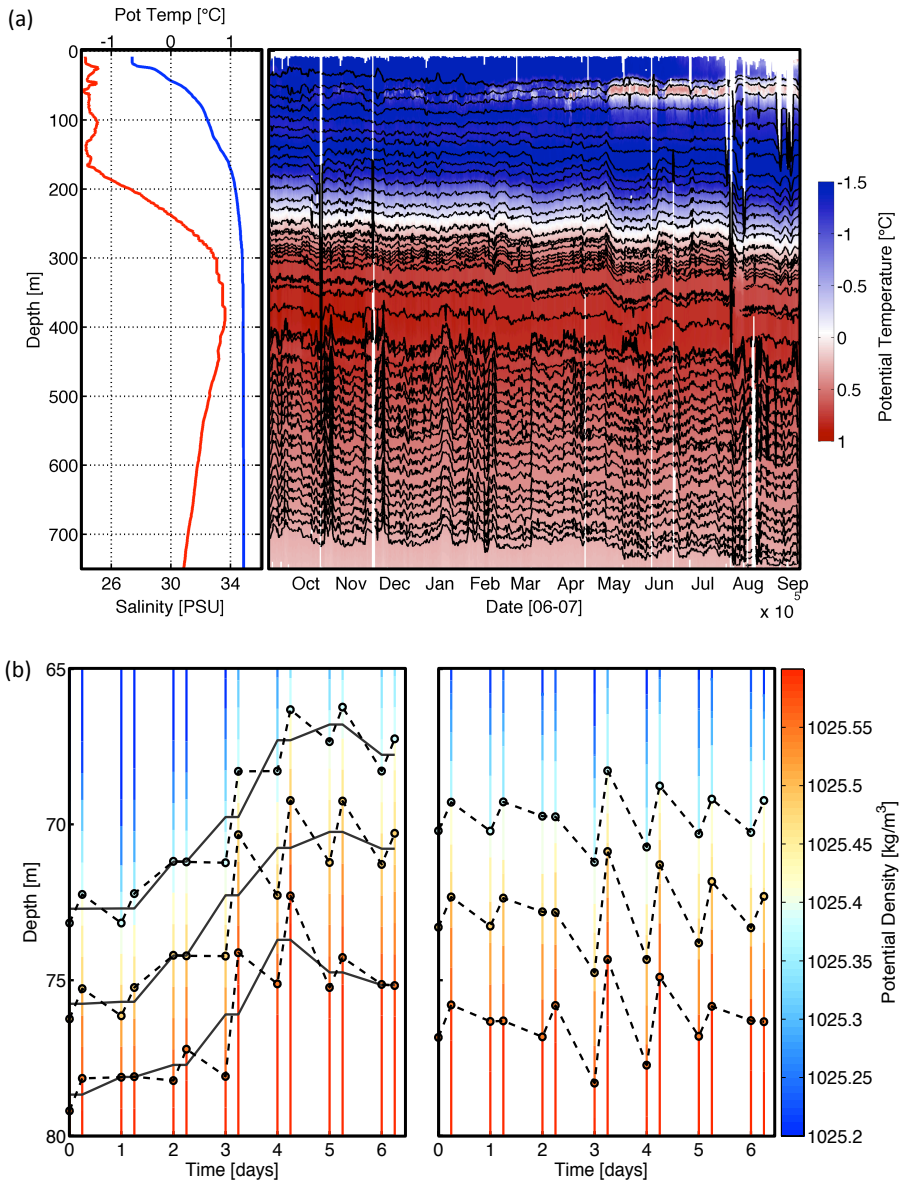

Figure 2.2: (a) Left panel: Potential temperature (red) and salinity (blue) profiles as in Fig. 2.1b. Right panel: Depths for a subset of isopycnals (black lines - plotted roughly every 15m) for ITP 6. The colours indicate potential temperature. (b) Left panel: Three sample isopycnals over a 7 day period. The coloured vertical lines are potential density values, the dashed black lines show the depths of the isopycnals, and the thick grey line shows the mean vertical displacement calculated as a 'daily average'. Right panel: The same three isopycnals with the mean removed, leaving only displacements near the inertial frequency.

ticularly considering the smooth bathymetry of the central Canada Basin. Furthermore, because most of the Canada Basin lies above the critical latitudes for the semidiurnal and diurnal tides, remotely generated internal tides cannot propagate across the basin and do not contribute to the observed isopycnal displacements for the three ITPs discussed here. Topographically trapped internal tides (e.g., Fer et al., 2010) will not be present away from rough topography. Vertical isopycnal displacements are therefore assumed to be primarily associated with wind-driven inertial motions.

2.4.1 Isopycnal displacements

Vertical displacements of isopycnals throughout the sampled water column (Fig. 2.2a) are estimated by tracking potential density (henceforth referred to as 'density') surfaces corresponding to the initial profile for each ITP, from early September, 2006. Potential density is calculated relative to the surface from the base of the mixed layer to the base of the double-diffusive staircase at 400 m, and calculated relative to 400 m for the remainder to the water column. This deeper reference level ensures that the derived potential density profile for lateral density intrusions below the Atlantic Water temperature maximum increases monotonically with depth. The choice of 400 m does not impact the resulting vertical displacement estimates.

Tracked isopycnals were initially separated by 1 m in the vertical, with the exception of the double-diffusive staircase in which individual density steps were tracked instead. No value is recorded if an isopycnal is statically unstable at a given time. Isopycnal depths can be determined for over 90% of all data points over the course of the year.

Within the double-diffusive staircase, vertical displacements are estimated by tracking the depth of the top and bottom of each constant density step, for which the second derivative of potential temperature with depth is at a minimum or a maximum respectively. This secondary condition on potential temperature is used in addition to density to avoid issues with conductivity sensor lag at sharp density interfaces (Johnson et al., 2007). This procedure is also used for the interleaving Atlantic Water layers immediately below the staircase.

Following the idea that the average of two profiles taken exactly half an inertial period apart would exclude the inertial signal, low frequency heaving with periods of a day and more is removed (Fig. 2.2b) by subtracting the average of each pair of profiles,

$$\eta = \eta_{tot} - \eta_{low} = \eta_{tot} - \frac{1}{2}(\eta_{0:00} + \eta_{6:00}). \tag{2.2}$$

This is similar to how Leaman and Sanford (1975) separate the inertial signal from low-frequency motions. This decomposition is not perfect, particularly because of the finite time the instrument requires to profile and because the inertial period is not exactly 12 h. Presumably a small amount of non-inertial high-frequency variance, η_{IWS}, is also mapped into η_{low} and removed. However, this decomposition takes advantage of the sampling of the ITP and provides a consistent definition of the low-frequency field with minimal aliasing of the inertial displacements.

2.4.2 Complex demodulation

Slow time variations in amplitude, A, and phase, ϕ, for periodic motions at frequency ω are estimated using complex demodulation (Emery and Thompson, 1998). Least-squares harmonic fits are applied to overlapping segments of isopycnal displacements, $\eta(t)$ (Eqn. 2.2), using a cosine wave of the form $A_\eta \cos(-\omega t + \phi)$. Near-inertial waves are assumed to be coherent for at least ~ 8 wave periods, so that a 4 day window of data can be used for each cosine fit. This technique can be used with unevenly spaced data, and requires only that the segment of data be longer than one wave period, and that the number of points be much higher than the number of frequencies to fit.

The near-inertial frequency used is $\omega = 1.05f$, (where f is the local inertial frequency, which varies with latitude as the ITP drifts). It was determined that $\omega = 1.05f$ explained the most variance in the data overall. The amplitude estimates were, however, relatively insensitive to the particular choice of near-inertial frequency ω, in the range $0.9f$ to $1.1f$.

Vertical displacements for each isopycnal are combined with those of the isopycnals im-

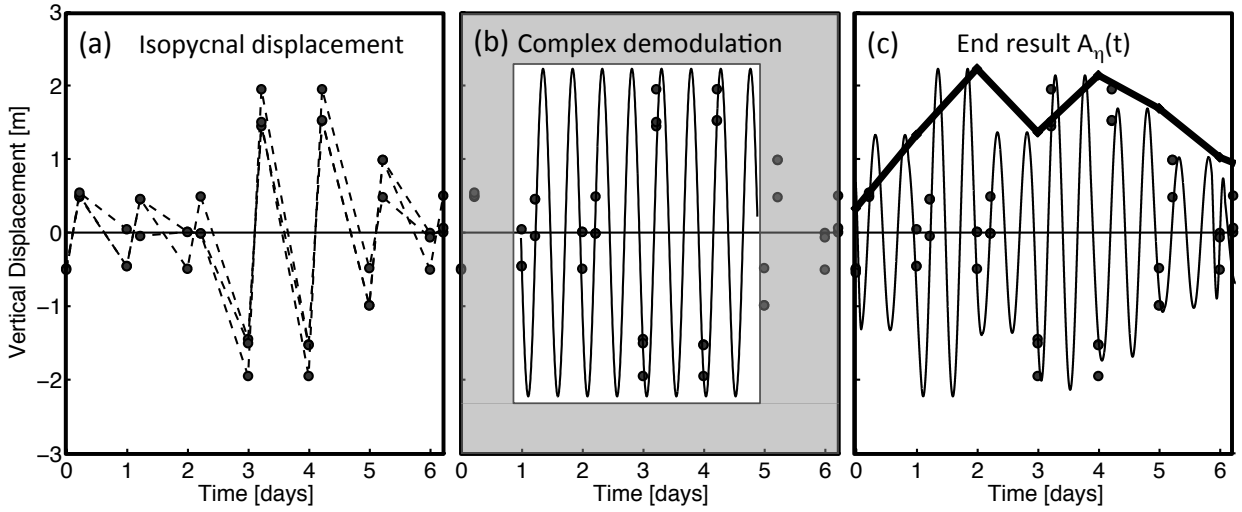

Figure 2.3: (a) Data: Vertical displacements for an isopycnal from Fig. 2.2b combined with the isopycnals immediately above and below to give 24 data points (grey dots) per four day window. (b) Method: A harmonic least-squares fit ($\omega = 1.05f$) to each window of data gives the amplitude and phase of the ideal cosine (thin black line) that best explains the variance in the data. (c) Result: The complex demodulation procedure produces a slowly varying wave amplitude (thick black line) $A_\eta(t)$ and phase ϕ(t) (not shown) corresponding to a near-inertial wave (thin black line - extrapolated using linear interpolation between daily values for A_η and ϕ).

mediately above and below, tripling the number of data points per fit and reducing the impact of random noise. This assumes wave coherence over $\sim$ 2-5 m in the vertical. For each time window, the amplitude and phase of the near-inertial wave that best explains the data are obtained (Fig. 2.3). The window is then shifted forward in time by one day, and a new amplitude and phase estimate are determined.

Waves with a frequency very different than the fitted frequency, or waves that are coherent for less than roughly 4 days, are not well captured using this technique. Cosine fits that explain little variance in the data are excluded based on the R^2 value. The coefficient of determination R^2 is calculated from:

$$R^2 = 1 - \frac{\sum(\eta_{data} - \eta_{fit})^2}{\sum(\eta_{data} - \overline{\eta_{data}})^2}, \tag{2.3}$$

where, for each segment of time, η_{data} gives measured vertical displacements, η_{fit} gives vertical displacements of the ideal cosine wave, the overbar denotes the time average of η_{data}, and the sum is taken over the 24 points in a given four day window (2 profiles per day, over 4 days, for 3 isopycnals). Any fit with an R^2 value of ≤ 0.25 (explaining 25% or less of the variance in the data) is excluded from the results. The amplitude A_η of any fit is also restricted to be less than 1.5 times the maximum measured displacement over the four day window.

The average R^2 value for the entire wave field for ITP 6 is $R^2 = 0.6$; in other words, 60% of the variance in the observed near-inertial vertical displacements can be explained by slowly-varying near-inertial waves (Fig. 2.4). Values are comparable for ITPs 4 and 5.

2.5 Uncertainty analysis

Several factors contribute to the uncertainty of the near-inertial wave field estimated using the method outlined in the previous section. This section investigates uncertainty caused by errors in the determination of isopycnal depths, by the presence of motions at super-inertial frequencies (internal wave continuum), and by the range of near-inertial frequencies present in the wave field (relative to the specified frequency of $1.05f$).

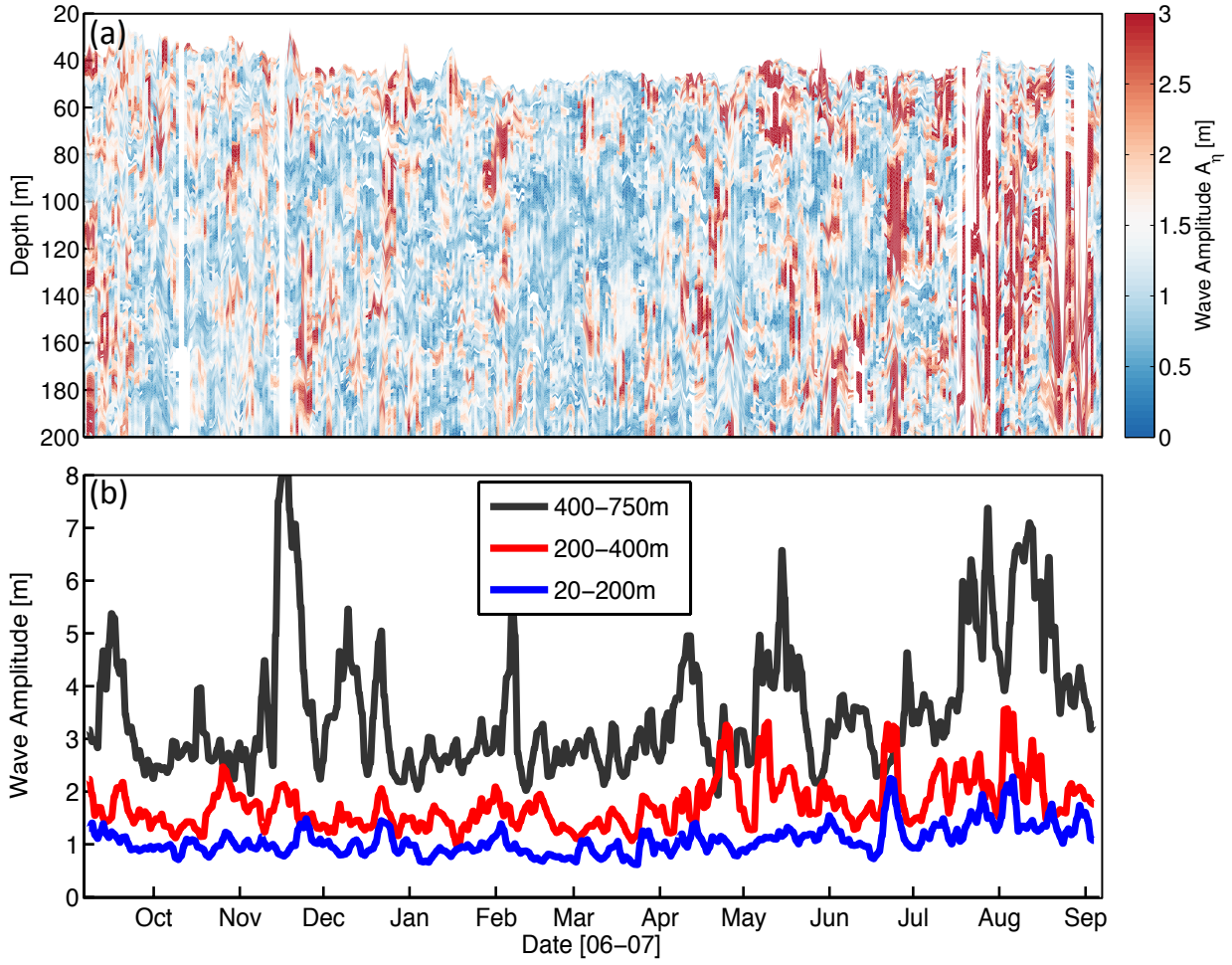

Figure 2.4: (a) Vertical displacement wave amplitude field for one full year of data from ITP 6, over the top 200 m of the water column. Waves with larger vertical displacements are red. Gaps are regions without data, or for which $R^2 < 0.25$. (b) Depth-averaged vertical displacement wave amplitude for the top 200 m (blue line), the double-diffusive staircase region from 200-400 m (red line), and the lower water column from 400-750 m (grey line).

The determination of isopycnal depths is limited by instrument noise. It is also limited by the vertical spacing between the processed salinity and temperature data provided by the ITP group (1 dbar). Because dissipation is so small in the Arctic Ocean, observed density inversions are likely instrument noise as opposed to actual overturns (Johnson and Garrett, 2004). The Thorpe displacements (Thorpe, 1977) are thus used as a measure of uncertainty in isopycnal depth (ϵ in Eqn 2.1).

Above the thermohaline staircase, the depth of an isopycnal is known to within 1 m, while for the water column below it is known to within 2 m. These values are comparable to the vertical spacing of the data points. Within the double-diffusive staircase it is difficult to determine the noise, ϵ, however it is expected to be of the same order as in the water column above. The possibility of a small systematic bias between the upward and downward ITP profiles used to determine isopycnal depth was investigated, but was found to contribute negligibly to the overall error in the wave field.

To account for potential aliasing of high-frequency internal waves into the near-inertial wave estimates, isopycnal displacements consistent with the spectral shape of the Garrett-Munk (GM) model of internal waves (Garrett and Munk, 1972; Gregg and Kunze, 1991), but an order of magnitude smaller [(Levine et al., 1985), Appendix], are included in the uncertainty analysis.

Statistical estimates of uncertainty in the near-inertial wave amplitudes are obtained using Monte-Carlo simulations. The complex demodulation method is applied to an ensemble of 300 known test waves with arbitrary phase and a specified (near-inertial) frequency of $1.05f$. Each test wave is subsampled to match the ITP sampling as outlined in the previous section. The uncertainty, δA_η, is taken to be two standard deviations (95% confidence interval) from the mean difference between the amplitude estimates and the known test wave amplitude. This procedure is repeated for every latitude and sampling interval considered in the analysis of the ITP data.

Variance in the data not associated with near-inertial waves is accounted for by adding random noise consistent with the uncertainty in isopycnal depth, ϵ, and variance consistent

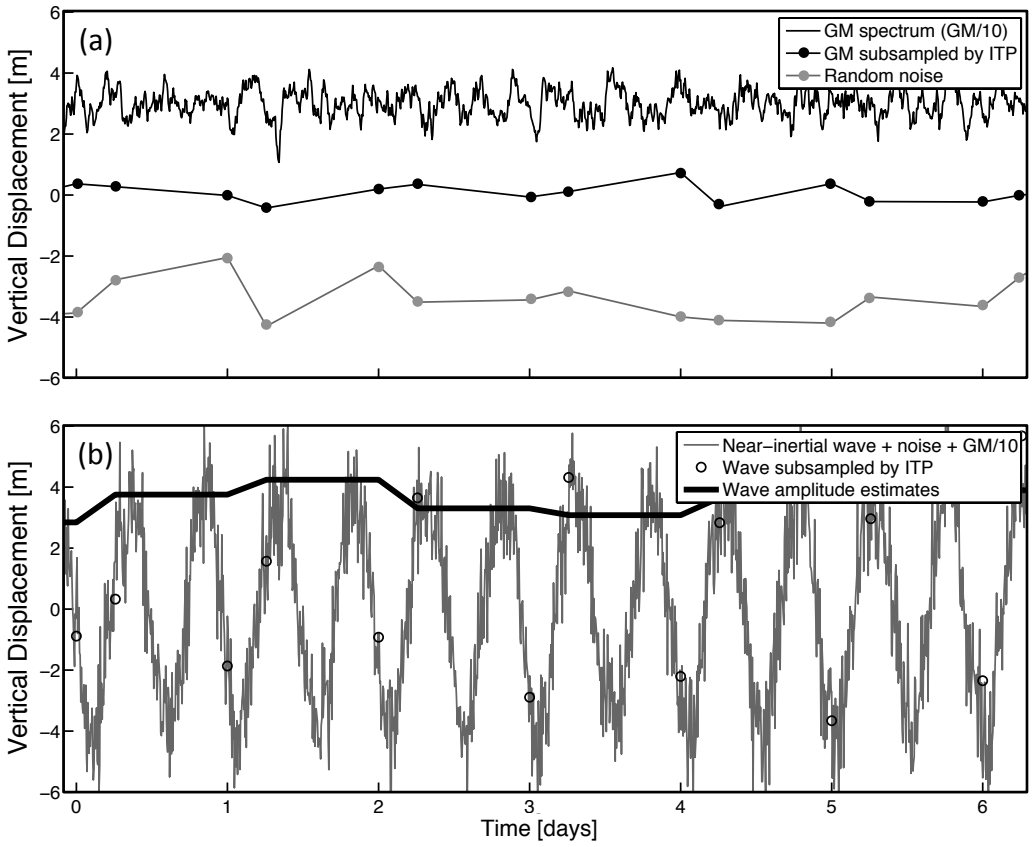

Figure 2.5: (a) Time series consistent with variance at the GM/10 spectral level (black line - vertically offset by 3 m), sub-sampled to match the ITP (black dotted line), appears similar to random noise (grey dotted line - vertically offset by -3 m). (b) Time series for a known near-inertial test wave with an amplitude of 4 m with GM/10 and random noise superimposed (grey line). This wave is subsampled to match the ITP (black circles), and wave amplitudes estimates are determined using complex demodulation (thick black line).

with the continuum internal wave spectrum, $\eta_{IWS} = GM/10$, onto a known test wave. This causes an absolute error in wave amplitude of ± 0.5 m above the double-diffusive staircase, ± 1.0 m within the staircase, and ± 1.5 m below. The variation with depth is a result of the increase in ϵ and the decrease in stratification with depth. In the absence of a near-inertial wave, the complex demodulation method is unable to find an appropriate cosine fit to $\epsilon + \eta_{IWS}$ over 90% of the time, as expected. When sub-sampled to match the ITP, a time series consistent with GM/10 appears similar to random noise, (Fig. 2.5), resulting in wave amplitude estimates that are statistically indistinguishable from zero.

Varying the frequency of the known test wave between f and $1.1f$ (relative to the specified cosine fit frequency of $1.05f$) causes a relative (percent) uncertainty in the wave amplitude of between $25\%A_\eta$ and $40\%A_\eta$ (Fig. 2.6a). This relative uncertainty varies slightly with depth due to the changing sampling interval between pairs of data points, but is predominantly affected by the latitudinal dependence of the local inertial frequency, f. Uncertainties are higher when the time-interval between measurements is almost equal to half the local inertial period. The restrictions on the R^2 value for a given fit and on the maximum amplitude relative to the measured displacements ensure that fits which are badly constrained are excluded from the wave amplitude estimates. A typical relative uncertainty is $\sim 30\%A_\eta$.

The uncertainty reported in Section 2.6 includes both the absolute and relative uncertainty. This uncertainty is ± 2 m or less for most amplitude estimates. The average is ± 1 m, with 95% of amplitudes inferred from the dataset accurate to within ± 3 m or better (± 1 m for the top 200 m). The large majority of wave amplitude estimates (Section 2.6) are thus statistically significant and are a good representation of the variance in the data points regardless of associated uncertainty (Fig. 2.6).

Uncertainties from the Monte-Carlo simulations do not represent a measure of disagreement between the amplitude estimates and the variance in the data points, which is quantified by the coefficient of determination R^2 (Section 2.4). Rather, they characterize how accurately the ITP measurements are able to capture the wave field in the presence of numerous sources of uncertainty.

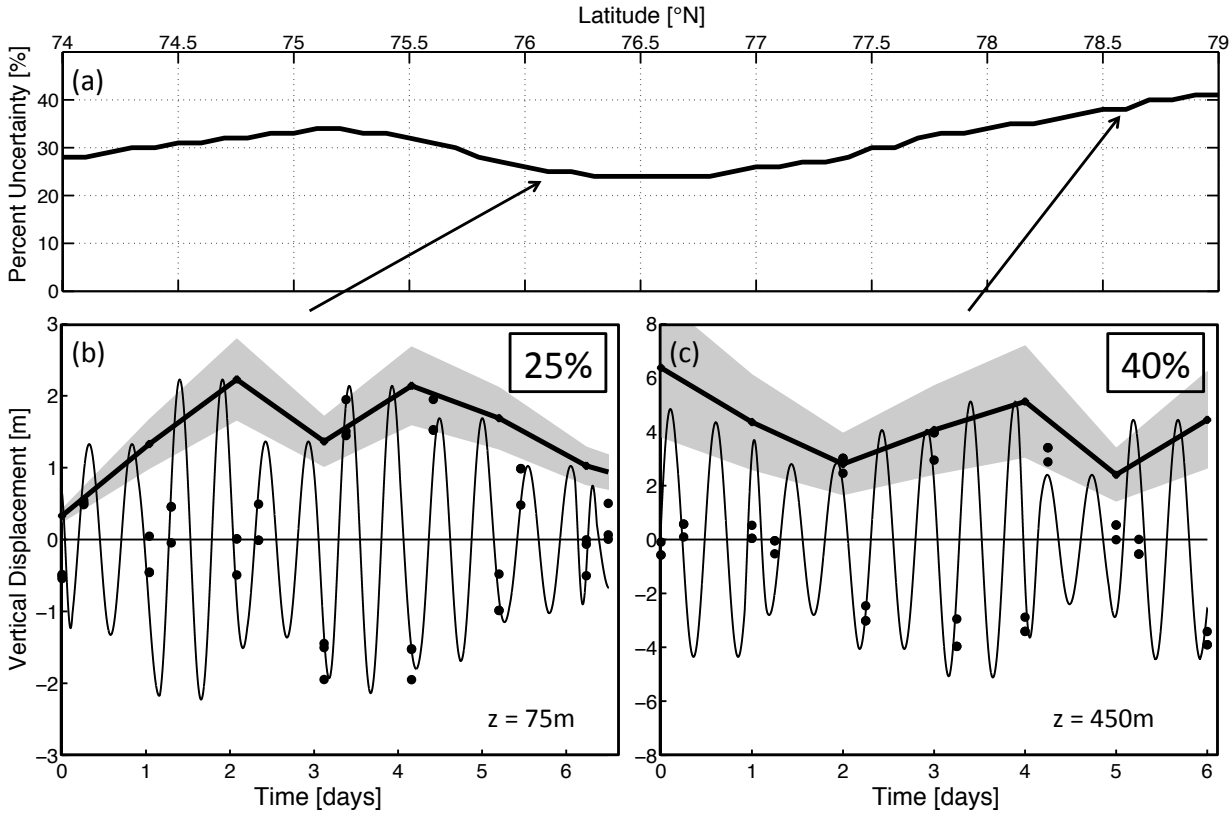

Figure 2.6: (a) Percent uncertainty in the wave amplitude estimates as a function of latitude based on Monte-Carlo simulations. (b) Example of 25% uncertainty in amplitude. Black dots are near-inertial vertical displacements from ITP 6 over 7 days measured near the surface. The thin black line shows the cosine wave fits determined using complex demodulation. The thick black line gives the associated vertical displacement amplitude estimates. The grey band shows the uncertainty in these estimates through time. (c) As in panel (b), but for an uncertainty of 40%.

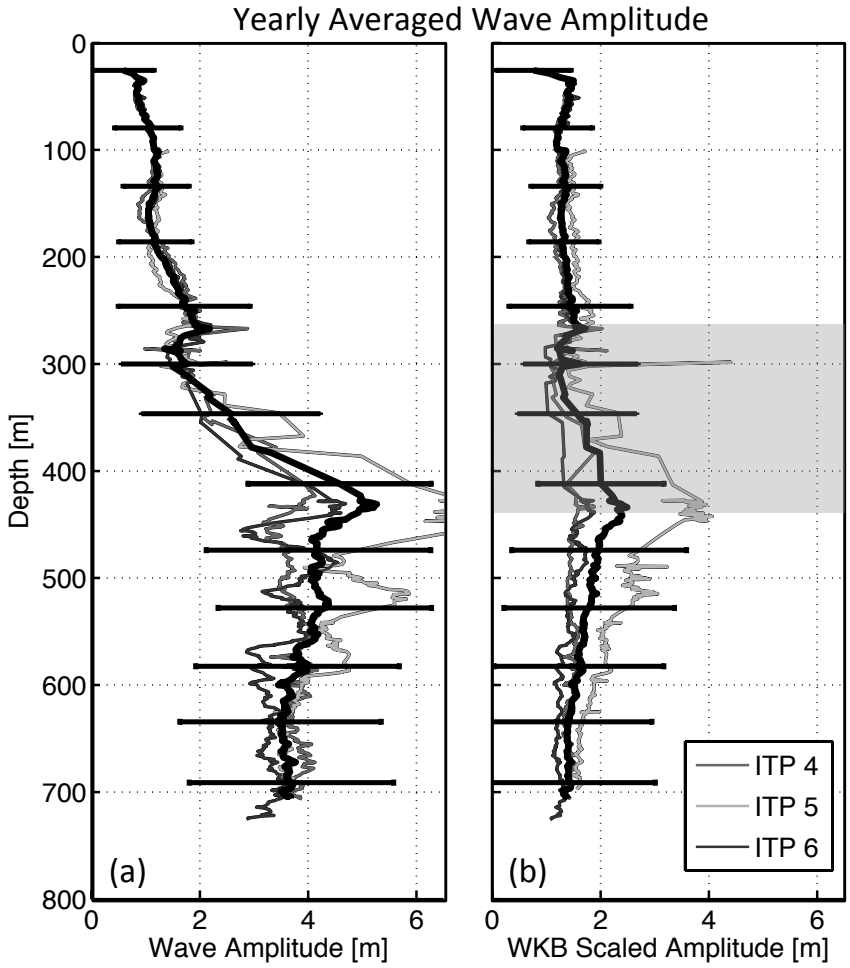

Figure 2.7: (a) Time-averaged vertical displacement amplitude $< A_\eta >$ vs. average isopycnal depth for ITPs 4, 5, and 6. The thick black line is the average of the three. The black horizontal lines show the combined error range. (b) As in (a), but for the WKB-scaled time-averaged vertical displacement amplitude, $< A_\eta \sqrt{(N(z)/N_0)} >$. The grey panel indicates depths within the double-diffusive staircase for which WKB-normalization is not truly applicable due to sharp changes in $N(z)$.

2.6 Discussion

The goal of this work is to quantify the near-inertial wave field from ITP data. The vertical displacement amplitude for near-inertial waves, and its associated uncertainty, is estimated for three ITPs that sampled in the central Canada Basin during 2006-2007. This field, shown in Fig. 2.4a for the top 200 m of the water column sampled by ITP 6, can be connected to physical processes influencing the waves, such as sea-ice cover and wind forcing.

During winter, wind speeds are typically higher, and fractional sea-ice cover is typically nearly 100% in the Beaufort Gyre region. During summer, the fractional sea-ice cover and ice thickness in the area around the ITP can decrease significantly. The instrument itself remains moored in a large ice floe ideally composed of thick multi-year ice. Wind speeds in summer are typically lower. The ITP drifts with the ice, whose motion is primarily a result of surface wind stress. This results in a strong inertial component to the ice motion, particularly for thinner, patchier summer sea ice, as investigated by Gimbert et al. (2012a). The near-inertial wave field will therefore be impacted by both wind forcing and sea-ice cover, on a range of timescales.

The amplitudes of the near-inertial waves observed increase with depth as shown in Fig 2.4b, reaching 3-5 m on average below 400 m (Fig. 2.7a), although highly variable, often as large as 10 m or more. [1] When the effects of decreasing stratification are taken into account via Wentzel-Kramers-Brillouin (WKB)-normalization [e.g., Pedlosky (2003)], most of the large-scale vertical variations in wave amplitude are eliminated (Fig. 2.7b). WKB-normalization, $A_\eta\sqrt{(N(z)/N_0)}$, in which N_0 is the average buoyancy frequency, assumes that the background buoyancy profile $N(z)$ varies slowly and smoothly on a vertical scale much larger than that of the waves.

Depth-averaged WKB-scaled near-inertial wave amplitudes are spatially distributed fairly evenly over all latitudes and longitudes traversed by the ITPs. Topographically-generated waves are unlikely due to the smooth bathymetry in the central Canada Basin. The WKB-

[1] For a wave with an amplitude of 3-5m at depths below 400m, a typical uncertainty is $\pm$2m.

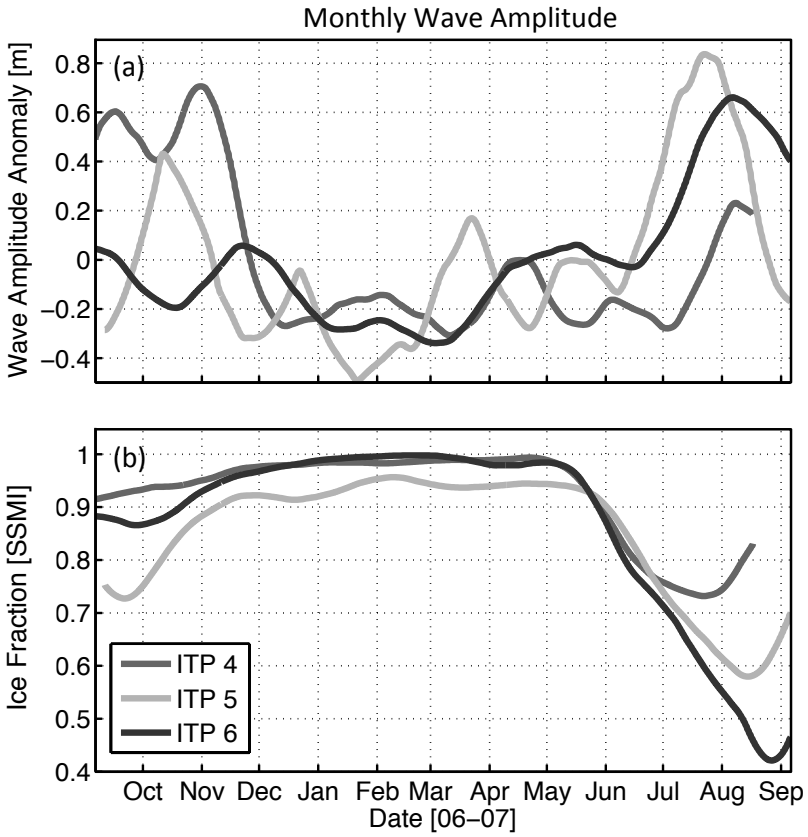

Figure 2.8: (a) WKB-scaled depth-averaged vertical displacement wave amplitude for the three ITPs, $< A_\eta \sqrt{(N(z)/N_0)} >$, plotted vs. time. The mean has been subtracted for each ITP and a 30-day low pass filter has been applied. The value of the mean for each ITP: 1.4 m for ITP 4, 2.2 m for ITP 5, and 1.4 m for ITP 6. (b) Fractional sea-ice cover around the ITPs over the course of the year, derived from SSM/I ice concentration satellite data and smoothed using a 30-day low pass filter.

scaled amplitude varies temporally on timescales from days to many months. On a seasonal timescale, wave energy is lower during winter, and increases significantly during summer (Fig. 2.8a). These variations may reflect seasonal changes in sea-ice cover (Fig. 2.8b). Fractional sea-ice cover around the ice floe drifting with each ITP was derived from SSM/I ice concentration satellite data (Cavalieri et al., 1996, updated 2008), gridded in 25 km x 25 km boxes. The mean was removed from each wave amplitude time series and both fields were smoothed using a 30-day low-pass filter. The average percent uncertainty in the depth-averaged WKB-scaled wave amplitude is $\sim 30\%$, resulting in an overall uncertainty of ± 1 m.

As sea ice around the ITPs decreases during summer (July to September), a corresponding increase in wave energy is observed, with an increase in the average wave amplitude of 0.45 m relative to winter (January to March). This change in amplitude represents $\sim 20\%$ of the total variance in the wave field over the course of the year. [2] In the Beaufort Gyre region of the Canada Basin, winds and storms are weaker during summer and increase during winter (Overland, 2009). In other words, near-inertial wave energy is observed to be highest during summer when winds are weakest, but sea-ice cover is reduced.

On a daily timescale, wave energy is higher and more variable during periods of less than 100% sea-ice cover (Fig. 2.9). Increases in wave amplitude tend to be episodic, with sudden jumps in energy associated with sudden decreases in ice fraction around the ITP. During periods of 100% ice cover, wave energy is lower and less variable. The WKB-scaled vertical displacement amplitude from ITP 6 (shown depth-averaged over the top 200 m in Fig. 2.9), has an overall uncertainty of ± 1 m.

High wind events were frequently associated with peaks in near-inertial wave amplitude (Fig. 2.10). [3] During winter, sea-ice cover inhibits direct wind forcing of the ocean surface and damps near-inertial waves, which may help explain the mismatch between the strength

[2]The remaining variance in the wave field is due variations on shorter than seasonal timescales, with interannual variability explored in Chapter 3: Dosser and Rainville (2015).

[3]Similar to observations of inertial velocity by Rainville and Woodgate (2009) in the Chukchi Sea.

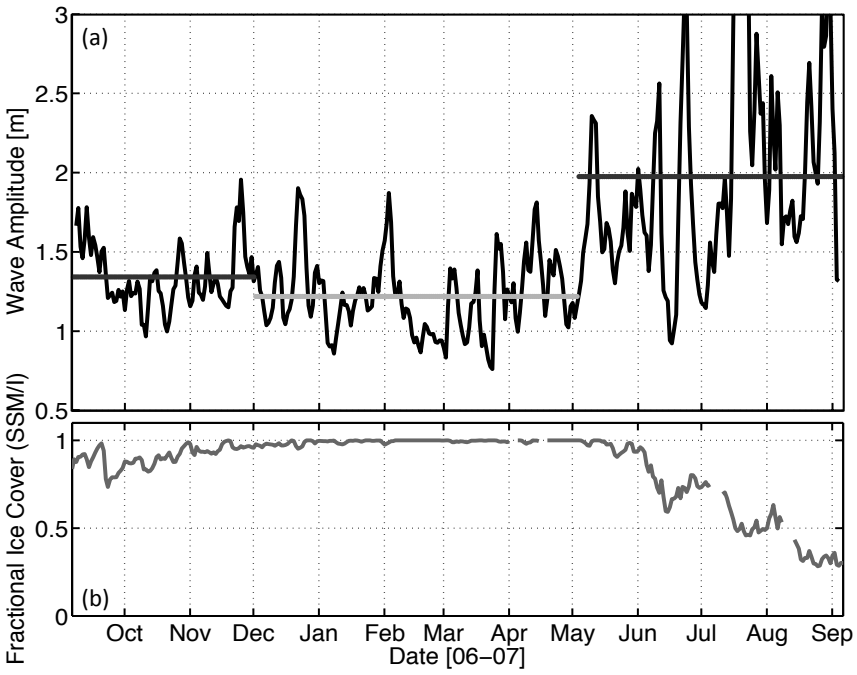

Figure 2.9: (a) Daily WKB-scaled vertical displacement wave amplitude, $< A_\eta \sqrt{(N(z)/N_0)} >$, from ITP 6, depth-averaged over the top 200 m. The dark and light grey lines show the mean wave amplitude during periods of $< 100\%$ sea-ice cover and 100% sea-ice cover, respectively. (b) The fractional sea-ice cover around the ITP over the course of the year, derived from daily SSM/I ice concentration satellite data.

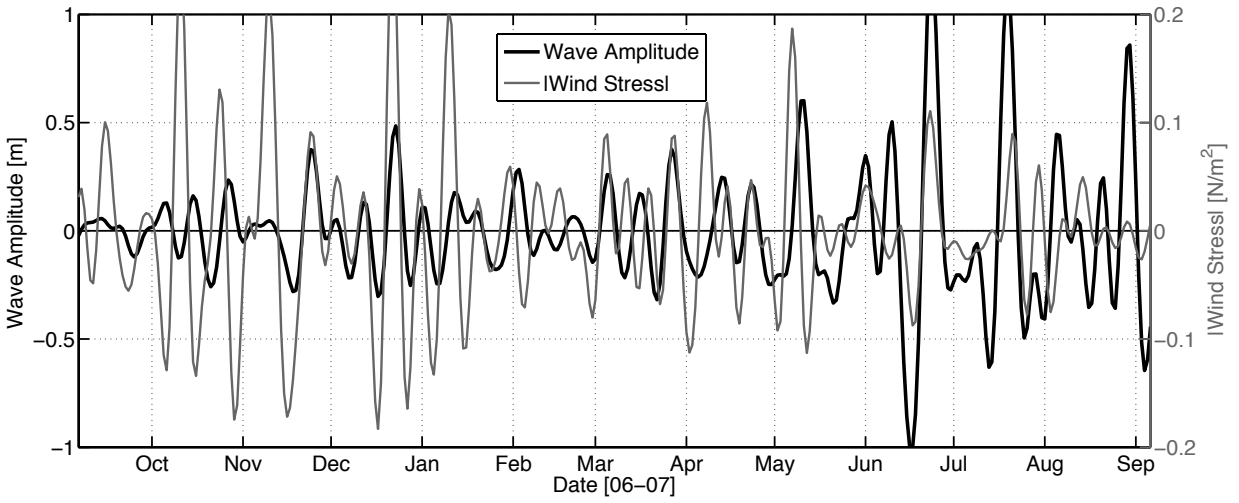

Figure 2.10: Time series of WKB-scaled vertical displacement amplitude for ITP 6 (black line), depth-averaged over the top 200 m, and the magnitude of the daily wind stress following the track of ITP 6 (thin grey line). Both fields have been band-pass filtered between 1/30 cpd and 1/7 cpd.

of the wind forcing and the strength of the wave response. Wind stress was determined using NCEP/ NCAR 10-m winds from the NCEP (National Centers for Environmental Prediction) Reanalysis project (Kalnay et al., 1996; Kanamitsu et al., 2002), interpolated from the global grid to the drifting ITP position. At high latitudes, this reanalysis wind data lacks the resolution to resolve the spatial and temporal patterns most efficient at generating near-inertial waves [(Alford, 2003), Personal communication; Harper Simmons and Kim Martini].

Despite these limitations, wave amplitude is observed to covary with surface wind forcing (Fig. 2.10). The depth-averaged WKB-scaled wave amplitude over the top 200 m is weakly correlated with the magnitude of surface wind stress from daily NCEP/ NCAR data, following the track of ITP 6 (correlation is R = 0.3, statistically significant at the 95% confidence level). Both fields have been bandpass-filtered between 1/30 cpd and 1/7 cpd to partially account for the mismatch in seasonal variability. [4]

[4]This filtering ensures the wave amplitude and wind records have equal degrees of freedom.

If only summer months (July - September) are considered, the correlation value rises to R = 0.5, significant at the 95% confidence level. For only winter months (January - March), the correlation is R = 0.3. If a slight lag of 1-2 days is used during winter, presumably reflecting the time needed for the wind to transfer momentum through the sea ice to the water below [5] , the correlation rises to R = 0.4.

The relationship between wind, sea ice, and near-inertial waves is complex, and much remains to be done before a comprehensive understanding of internal wave generation and propagation is reached for the Canada Basin. In the present work, the near-inertial wave field has been quantified using the ITP dataset, and shown to have clear connections to physical processes on multiple timescales.

2.7 Summary

The near-inertial internal wave field in the central Canada Basin from Sept. 2006 to Sept. 2007 is estimated using three Ice Tethered Profiler instruments. This paper demonstrates that it is possible to use the ITP dataset to extract and quantify the near-inertial wave field at all depths, including regions of complex stratification such as the double-diffusive staircase found in the Canada Basin. The results are accurate, physically reasonable, and the magnitude of the near-inertial wave field can be linked to sea-ice cover and surface wind forcing.

On timescales of days to weeks, fluctuations in wave energy are connected to both increased surface wind forcing and decreased sea-ice cover, with a weak correlation between wind stress and wave amplitude. On a seasonal timescale, decreased sea ice around the ITP during summer is linked to increased wave energy. Thick winter ice may prevent momentum transfer from winter storms to the ocean, damping wave motion and resulting in a mismatch between wind forcing and the wave response. During summer, thin, patchy ice may allow more direct wind forcing of the surface ocean and increased near-inertial wave generation.

[5] The impact of sea-ice properties on wind forced internal wave generation is discussed further in Chapter 3: Dosser and Rainville (2015).

There is a quantifiable connection between seasonal changes in sea ice and wave energy for the Canada Basin during 2006-2007, with $\sim 20\%$ of the total variance in the depth-averaged wave field explained by changes in sea-ice cover.

As seasonal sea-ice cover continues to decrease, and the Canada Basin becomes ice-free during the summer, it is expected that direct wind forcing on the ocean's surface will significantly alter the properties of the internal wave field, particularly in the near-inertial band. The potential impacts of an evolving internal wave field are significant, and include increased vertical heat flux due to wave breaking and an increase in the associated mixing, as well as potential erosion of stratification features such as the double-diffusive staircase and the summer halocline. The extent and magnitude of such changes in the annual and interannual variability of the wave field are currently unknown.

Building on the work presented here, it is possible to investigate and quantify such changes using the greater ITP dataset. The full ITP dataset is extensive, with wide spatial coverage and over 8 years of observations. There are currently several ITPs deployed in the Canada Basin, with more deployments likely during the next several years. Despite their limitations, ITPs provide the best opportunity to investigate the relative roles of wind forcing, sea-ice cover, and stratification on the near-inertial wave field in the Arctic Ocean, providing insight into the impact of rapid climate change.

2.8 Appendix: Arctic internal wave spectrum

This section presents observations from a mooring deployed in the central Canada Basin, which confirm that the internal wave continuum in the Arctic is at least one order of magnitude less energetic than at lower latitudes.[6] As part of the Beaufort Gyre Exploration Project (BGEP, see Proshutinsky et al., 2009), a bottom-anchored mooring has been deployed near 74°N, 140°W (site "D") since 2002. In addition to a moored profiler sampling the properties of the water column between 50 and 2000 m on a time scale of a day, BGEP

[6]Note also the sharp peak in both velocity (a) and vertical displacement (b) at the inertial frequency f.

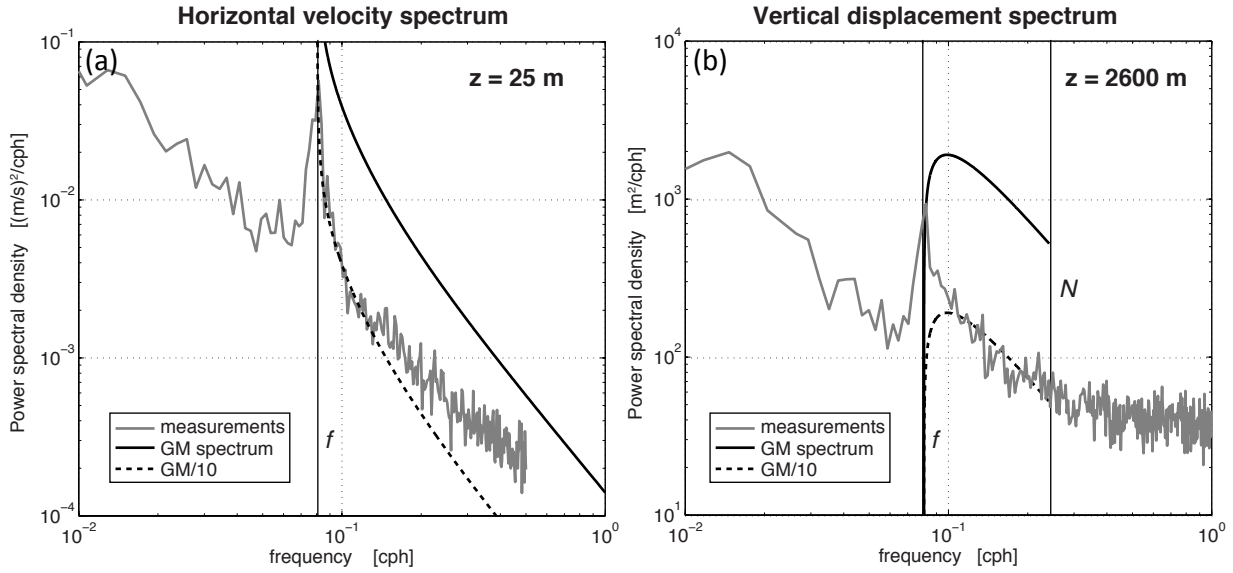

Figure 2.11: (a) Horizontal velocity spectrum at 25 m, and (b) vertical displacement spectrum near 2600 m, measured from a mooring deployed near 74°N, 140°W in 2007-2008. In both cases, the measured spectra (gray) are about 10 times less energetic than the Garrett-Munk spectral model (black lines).

mooring-D was equipped in 2007-2008 with an up-looking Acoustic Doppler Current Profiler (ADCP) mounted on the 50-m sub-surface buoyancy sphere, and with fixed-depth temperature sensors in the deep bottom thermohaline staircase (Timmermans et al., 2010). These instruments sampled fast and accurately, providing velocity estimates every hour for the ADCP and temperature every 3 min at depth.

While the ADCP does not provide estimates of isopycnal displacements, it allows us to estimate the near-surface horizontal velocity spectrum (Fig. 2.11a). The annual mean amplitude of the inertial currents, rotating clockwise in time, at this location is 1.5 cm s^{-1}, with maximum values reaching 6 cm s^{-1} (not shown). These measured inertial currents are of the same order as those measured by Plueddemann et al. (1998). The buoyancy frequency near 25 m depth is about 6 cph. Assuming a near-inertial frequency of $1.05f$, the mean vertical displacements associated with these waves are roughly 1 m, in agreement with

values found using the ITP data.

Deeper, the time series measured by the temperature sensor chain is coherent in depth, consistent with low-mode vertical heaving of the water column (Timmermans et al., 2010). Converting the temperature anomalies to a vertical displacement by using the mean vertical gradients, the spectrum of vertical displacement shows high sub-inertial energy, and a well-defined inertial peak (Fig. 2.11b). The near-inertial peak in displacement is what the method outlined in the paper captures (in the upper ocean). The buoyancy frequency near 2600 m is about 0.25 cph. In both cases the energy level of the internal wave continuum (between f and N) is about one order of magnitude smaller than the Garrett-Munk spectral level, as observed previously (e.g., Levine et al., 1985, 1987). Note that the Garrett-Munk spectrum has no energy for displacements at the inertial frequency, but a large amount of near-inertial variance is observed in the deep ocean.

2.9 Acknowledgments

We gratefully acknowledge the Ice-Tethered Profiler Program and the Beaufort Gyre Exploration Program based at the Woods Hole Oceanographic Institution (in collaboration with researchers from Fisheries and Oceans Canada at the Institute of Ocean Sciences) for deploying and maintaining the ITPs and the BGEP moorings, as well as processing the data and making it available to the scientific community (*http://www.whoi.edu/itp* and *http://www.whoi.edu/beaufortgyre*). The ITP program and J. Toole's contributions were supported by the National Science Foundation Office of Polar Programs Arctic Observing Network. We acknowledge the support of the Office of Naval Research (grant N00014-11-1-0454) for this study. Support for H. Dosser was also provided by the Natural Sciences and Engineering Research Council of Canada. NCEP Reanalysis Derived data was provided by NOAA/OAR/ESRL PSD, Boulder, Colorado, USA, from their Web site at *http://www.esrl.noaa.gov/psd/*. Sea-ice concentrations from Nimbus-7 SMMR and DMSP SSM/I-SSMIS passive microwave data was provided by the National Snow and Ice Data Center, Boulder, Colorado USA.

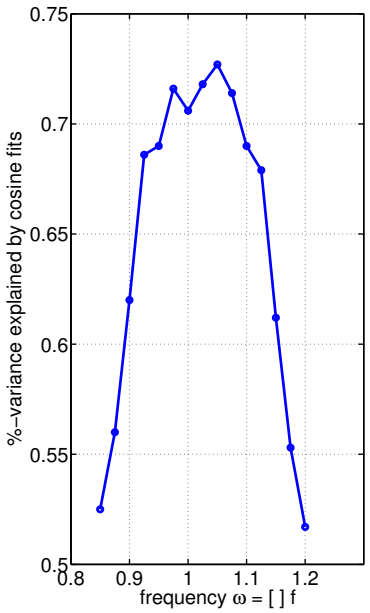

Figure 2.12: Percentage of variance in measured isopycnal displacements from ITPs explained by cosine wave fits with various frequencies within the near-inertial band.

2.10 Appendix: Unpublished material

2.10.1 Choice of near-inertial frequency

The complex demodulation technique to determine near-inertial wave vertical displacement amplitude uses least-squares harmonic fits to overlapping segments of isopycnal displacements, $\eta(t)$, with cosine waves of the form $A_\eta \cos(-\omega t + \phi)$. The near-inertial frequency used, $\omega = 1.05f$, explaines the most variance in the measured isopycnal displacements (Figure 2.12). However, any near-inertial frequency ω, in the range $0.9f$ to $1.1f$ results in similar values for the vertical displacement amplitude estimates.

Chapter 3

DYNAMICS OF THE CHANGING NEAR-INERTIAL INTERNAL WAVE FIELD IN THE ARCTIC OCEAN

Note: Chapter is in revision in the AMS Journal of Physical Oceanography as of August 2015.
Citation: Hayley V. Dosser and Luc Rainville: Dynamics of the changing near-inertial internal wave field in the Arctic Ocean. J. Phys. Oceanogr.

3.1 Abstract

The dynamics of the wind-generated near-inertial internal wave field in the Canada Basin of the Arctic Ocean are investigated using the drifting Ice-Tethered Profiler dataset for the years 2005 to 2014, during a decade when sea-ice extent and thickness decreased dramatically. This time series, with nearly ten years of measurements and broad spatial coverage, is used to quantify a seasonal cycle and interannual trend for internal waves in the Arctic, using estimates of the amplitude of near-inertial waves derived from isopycnal displacements. The internal wave field is found to be most energetic in summer when sea ice is at a minimum, with a second maximum in early winter during the period of maximum wind speed. Amplitude distributions for the near-inertial waves are quantifiably different during summer and winter, due primarily to seasonal changes in sea-ice properties that affect how the ice responds to the wind, which can be expressed through the 'wind factor' - the ratio of sea-ice drift speed to wind speed. A small positive interannual trend in near-inertial wave energy is linked to the pronounced sea-ice decline during the last decade. The overall variability in the internal wave field increases significantly over the second half of the record, with an increased probability of larger-than-average waves in both summer and winter. This is linked to an overall increase

in variability in the wind factor and sea-ice drift speeds, and reflects a shift in year-round sea-ice characteristics in the Arctic, with potential implications for dissipation and mixing associated with internal waves.

3.2 Introduction

The standard picture of Arctic internal waves derives from observations made during the 1980s and 1990s (e.g., the Arctic Internal Waves Experiment - AIWEX Spring 1985, Levine et al. (1987); D'Asaro and Morehead (1991); Merrifield and Pinkel (1996), and the Surface Heat Budget of the Arctic Experiment - SHEBA 1997 to 1998, Pinkel (2005)), which found a quiescent Arctic Ocean with an internal wave field energy level an order of magnitude or more below that at lower latitudes (Levine et al., 1985, 1987).

Low internal wave energy levels in the Arctic are attributed to the presence of sea ice, which causes dissipation of internal waves in the under-ice surface boundary layer, limiting energy propagation across the Arctic (Morison et al., 1985; Pinkel, 2005; Fer, 2014). It has been suggested that sea ice impedes momentum transfer from the wind to the water column (Plueddemann et al., 1998), with ice deformation being of more importance to internal wave generation (Halle and Pinkel, 2003).

At lower latitudes, internal waves carrying wind energy through the water column are associated with significant diapycnal mixing, resulting in water mass modification and redistribution of ocean properties (Munk and Wunsch, 1998). The impact of rapid Arctic sea-ice decline on internal wave generation, propagation, energy, and the associated mixing rates is largely unknown. This paper presents long-term estimates of the internal wave climate in the Canada Basin, and seeks to address the question of changes in internal wave energy in the Arctic by quantifying the relationship between sea-ice properties and the amplitude of near-inertial internal waves, both spatially and temporally.

Near-inertial waves in the Arctic

The near-inertial frequency band, from roughly $f - 1.1f$, where f is the local Coriolis frequency, contains most of the energy in the internal wave field (Garrett and Munk, 1972; Garrett, 2001), matching observations of the internal wave spectrum in the Arctic Ocean (Halle and Pinkel, 2003; Fer, 2014; Cole et al., 2014). Near-inertial internal waves are likely whenever wind stress resonantly forces the air-ice or air-water interface at or near the inertial frequency. In the Northern Hemisphere, anti-cyclonic or clockwise inertial oscillations are set up in the sea ice and mixed layer. These purely horizontal oscillations create disturbances at the base of the mixed layer, generating a freely propagating near-inertial wave in the stratified water column below (D'Asaro, 1985). The result is vertical propagation of energy through the water column to depths at which the internal waves can become unstable and break (Gregg et al., 1986; Hebert and Moum, 1994).

Near-inertial internal waves can also be generated as a result of the motion of drifting sea ice. The rough bottom of the ice impulsively forces the water column, or there may be horizontal variations in bottom roughness that cause vertical motion of the fluid below. The resulting pattern of forcing moves at the sea-ice velocity, and can generate near-inertial waves with horizontal and spatial scales consistent with observations (D'Asaro and Morehead, 1991) and related to ice roughness and ice-ocean drag (McPhee and Kantha, 1989).

In the presence of sea ice, the transfer of momentum from the wind to internal waves is also complicated by variations in the air-ice drag coefficient. The drag coefficient for thick, rigid multiyear ice, rafted into peaks and ridges and possibly covered in deep snow, is very different from that for thin, patchy first-year ice, with large melt ponds and surrounded by areas of open water. Yet the ice concentration as measured by satellite can be the same for both. Martin et al. (2014) found that modelled momentum transfer was at a maximum for $\sim$80% ice concentration, since sea ice provides a rougher surface than open water. Andreas et al. (2010) considered changes in sea-ice form drag associated with leads and melt ponds in the marginal ice zone and found maximum momentum transfer for $\sim$50% ice cover. These

studies were not considering ice motion at the inertial frequency or the generation of internal waves by sea ice. Nevertheless, energy in the internal wave field is expected to be closely linked to sea-ice characteristics that affect the drift speeds or deformation of the ice.

In most of the world's oceans, internal waves at tidal frequencies are a dominant contributor to the oceanic variance (Garrett and Kunze, 2007). These 'internal tides' are generated when the barotropic tide sloshes back and forth over topographic features such as the Northwind Ridge or the Yermak Plateau, launching upward propagating internal wave beams at the tidal frequency. In the Arctic Ocean, the M2 and S2 tidal frequencies fall within the near-inertial frequency band. However, because the majority of the Arctic Ocean lies north of the critical latitude for the dominant semi-diurnal lunar M2 tide (74.5^oN), topographically generated internal tides are evanescent and must dissipate locally (Simmons et al., 2004). Localized topographic mixing associated with the internal tides may therefore be important (D'Asaro and Morison, 1992; Plueddemann, 1992; Fer et al., 2010; Lenn et al., 2011; Rippeth et al., 2015), but a significant internal tide within the central Canada Basin, away from the basin boundaries, is not expected.

Changes in the Arctic

In recent decades, the Arctic Ocean has undergone rapid changes. Sea ice decline has accelerated over the last decade, with significant decreases in summer sea-ice extent (Serreze et al., 2007; Stroeve et al., 2012) and thickness (Rothrock et al., 2008; Lindsay and Schweiger, 2015), and less multiyear ice overall (Comiso, 2002). Winter storms may be increasing in frequency and intensity (Serreze et al., 1997; McCabe et al., 2001; Zhang et al., 2004) with an associated increase in sea-ice drift speeds (Hakkinen et al., 2008).

Ice speed varies roughly linearly with wind speed, and is influenced by internal ice stress and air-ice and ice-ocean drag, which are in turn related to the concentration, thickness, and deformation of the ice cover (Hakkinen et al., 2008). Spreen et al. (2011) and Rampal et al. (2009) both reported increased sea-ice drift speeds in recent decades, as well as a sharp increase in ice deformation rate (Rampal et al., 2009). The magnitude of inertial oscillations

in the sea-ice has also increased during the last 30 years (Gimbert et al., 2012b), due to the changing characteristics of the sea ice (Gimbert et al., 2012a). It has been suggested that these changes could cause an increase in the energy of the Arctic internal wave field, particularly during the summer months, but this has not been readily apparent (Gimbert et al., 2012a; Rainville et al., 2011).

Previous measurements of the internal wave field in the Arctic Ocean have shown indications of a seasonal cycle related to sea-ice cover (Plueddemann et al., 1998; Halle and Pinkel, 2003; Rainville and Woodgate, 2009). Martini et al. (2014) observed a seasonal cycle in near-inertial wave energy using a mooring array on the Beaufort continental slope, and found a peak in internal wave energy during ice formation in the fall, corresponding to <90% ice concentration. Cole et al. (2014) found elevated near-inertial wave energy in the Canada Basin in the fall and early winter of 2009 relative to that in late winter. Dosser et al. (2014) found indications of a seasonal cycle in near-inertial vertical displacement wave amplitude, with larger waves during periods of $< 100\%$ sea-ice concentration. However, comparisons of historic data with recent XCP and CTD measurements by Guthrie et al. (2013) found no trend in internal wave energy in the Beaufort Sea over the last 30 years, which they attribute to an increase in the strength of the near-surface stratification.

Estimating the internal wave field in the Western Arctic

This paper presents the first multiyear record of internal waves in the Arctic Ocean, with spatial coverage over much of the Canada Basin. Observations of Arctic internal waves have typically been spatially and temporally limited, due to the difficulty of making wintertime measurements and the battery power required to obtain the necessary time resolution from a mooring or profiler. Ice-Tethered Profiler (ITP) data provides a nearly decade-long record, from 2005 to 2014, with year-round measurements from just below the mixed layer to ∼750m depth. Spatially, the ITPs provide coverage over much of the study region; the Beaufort Gyre region of the Canada Basin, from roughly 72^oN to 82^oN and from roughly 130^oW to 160^oW (Figure 3.1).

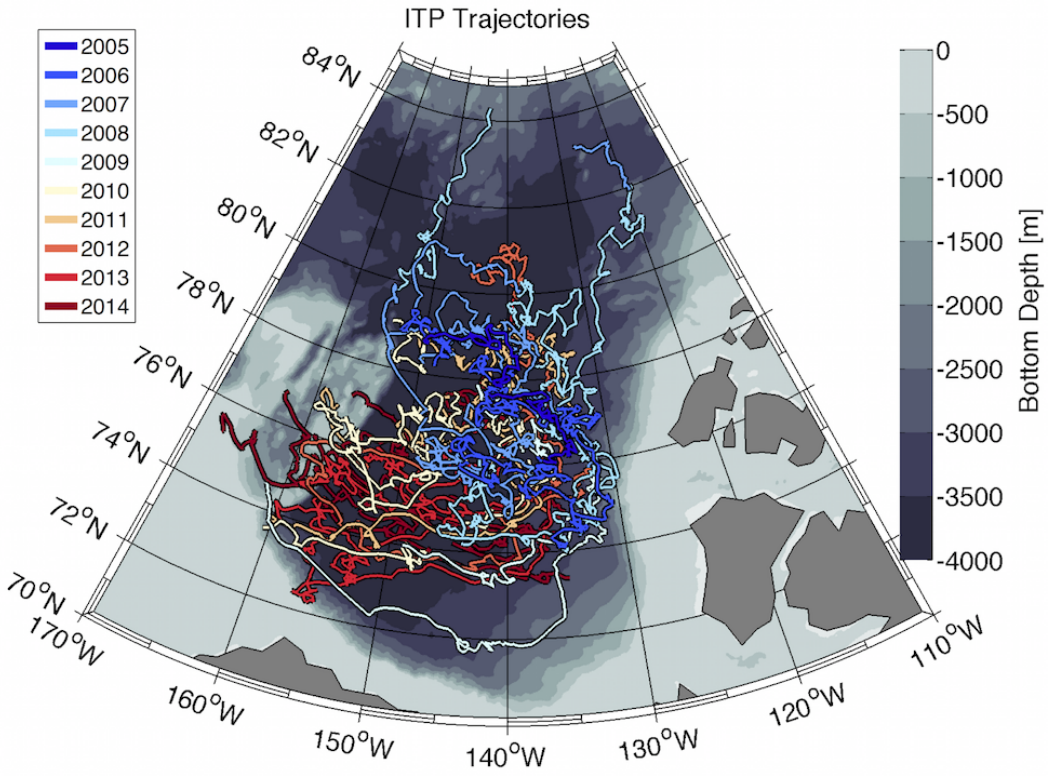

Figure 3.1: ITP trajectories in the Canada Basin from 2005 to 2014 (coloured by year). Bathymetry is given by grey-scale contours, with land in dark grey.

The paper is organized as follows: In Section 3.3, the data products used are described. The methods used to calculate the near-inertial wave field are explained in Section 3.4. A clear spatial trend in near-inertial wave amplitude with latitude is investigated in Section 3.5.1. Seasonal variations in the wave field are quantified and compared to changes in the wind factor, which relates to wind speed and ice speed, in Section 3.5.2, and increasing interannual trends in near-inertial wave energy and variability are shown to correspond to trends in sea-ice properties in Section 3.5.3. In Section 3.6, air-ice-ocean dynamics pertaining to wave generation are discussed and connected to the observed seasonal and interannual variations.

3.3 Data

3.3.1 Ice-Tethered Profiler

The data used herein were collected by 27 ITPs that drifted in the Beaufort Gyre region of the Canada Basin between Fall 2005 and Fall 2014 (Appendix), completing a total of just over 30000 density profiles. This represents a subset of the total ITP dataset, but includes the majority of profiles in the Canada Basin. Excluded were ITPs that stopped profiling after a month or two (to minimize a seasonal bias in number of measurements), and those with drift tracks outside of the chosen study region.

ITPs are anchored in a perennial ice floe by a surface buoy, and report temperature and conductivity at 1Hz, corresponding to roughly every 0.25m in the vertical, from ∼7m below the surface to ∼750m depth. The data are transmitted by an inductive link to a surface unit, where they are relayed to shore by the Iridium satellite system (Krishfield et al., 2008). Most ITPs sample the water column twice per day, with one-way vertical profiles beginning at 00:00 and 06:00 UTC. Other sampling schedules include 4 profiles per day, and others have more frequent sampling of the upper water column. The profiling instrument moves vertically at ∼0.25m s^{-1}, so that a 750m profile takes about 1 hour to complete. Each surface unit also reports hourly GPS position data.

Raw temperature, conductivity, and pressure profiles from all 27 ITPs are processed following similar techniques to those used by the ITP group at the Woods Hole Oceanographic Institution (*www.whoi.edu/itp*, Krishfield et al. (2006)). Processing steps include identification and removal of unphysical data, corrections for the sensor response behaviour (including thermistor lag, temperature and conductivity sensor physical separation, and conductivity thermal mass). As noted in Krishfield et al. (2006), a pressure correction is needed because of geometry, and because the CTD sensors are in the wake of the instrument during down profiling. However, here that correction is chosen to be a pressure offset that can only vary linearly with time (calculated over the length of each deployment, to allow for sensor drift). In contrast to the WHOI processing, the correction used here is independent of drift speed, as no solid correlation between ice speed and pressure offset was found for the entire ITP dataset. The processing also ensures that the time-mean density profiles from all up and down profiles are the same. The spatial and temporal patterns and conclusions discussed herein are not changed if the WHOI correction (empirically relating pressure offset to ice drift speed) is applied instead.

3.3.2 Wind Velocity

Wind velocity was obtained from ERA-interim 10-m winds from the European Centre for Medium-Range Weather Forecasts (ECMWF) reanalysis (Dee et al., 2011), which is calculated on a 0.75×0.75 degree grid. Comparisons (not shown) with 10-m winds from the NCEP (National Centers for Environmental Prediction) Reanalysis project (Kalnay et al., 1996; Kanamitsu et al., 2002), calculated on a 2.5×2.5 degree grid, did not significantly alter the results presented herein. The wind velocity data currently available from reanalysis products is gridded every 6 hours, and so cannot resolve the inertial frequency band partially responsible for wave generation (Alford, 2003; Martini et al., 2014).

3.3.3 Sea-ice concentration

SSM/I satellite passive microwave data (Cavalieri et al., 1996, updated 2008), provided 25km×25km gridded sea-ice concentration. Sea-ice concentration in a 125km×125km box around the ITP was selected for the analysis herein, as 125km is of the same order as the horizontal resolution of the wind velocity data, is a reasonable horizontal scale for wind forcing by storms, and is comparable to the expected horizontal extent of the internal waves themselves (a typical horizontal wavelength for a near-inertial wave with vertical wavelength between 10-100m would be roughly 5-50km). Average sea-ice concentration is generally not very sensitive to the choice of box size, from 25km up to values of several hundred kilometres. The average values of sea-ice concentration reported herein are not necessarily representative of the overall Canada Basin average as ITPs do not sample uniformly; regions of open water, for example, are very rarely sampled.

3.3.4 Sea-ice velocity

The motion of the ITP surface unit provides the velocity of the ice floe in which the instrument is anchored. Each ITP track is determined from hourly GPS measurements, and frequently shows the ITP moving in inertial circles and/or traveling rapidly in a given direction. Sea-ice velocity is separated into sub-inertial ($< 0.9f$, herein referred to as 'ice drift speed' or 'sub-inertial ice drift speed') and near-inertial ($0.9 - 1.1f$) bands, with the near-inertial band further separated into the clockwise (CW) and counter-clockwise (CCW) components of motion using rotary spectral analysis. The inertial CW component of sea-ice velocity dominates over CCW for most time periods.

3.3.5 Barotropic tide

The AODTM-5 barotropic forward tide model for the Arctic Ocean (Padman and Erofeeva, 2004) is used to determine the tidal current velocity associated with the semi-diurnal tidal components (M2, S2, N2, K2) in the Canada Basin. The model provides values on a 5km

regular grid based on solving the shallow water equations following Egbert and Erofeeva (2002). Tidal current speeds are determined along each ITP track for the full semi-diurnal tidal signal, and for specific components of interest.

3.4 Methods

The typical ITP sampling scheme poorly resolves isopycnal displacements associated with near-inertial waves. Each day, a pair of profiles separated by ∼6 hours is collected, an interval chosen to minimize 'potential biases' associated with inertial waves in daily averages. The near-inertial signal can be extracted from the data by taking advantage of the coherence of near-inertial waves over a few days, and the fact that the inertial period is not exactly 12 hours. Dosser et al. (2014) describes how complex demodulation can be used to estimate the vertical displacement amplitude of near-inertial internal waves from ITP data. This procedure is briefly summarized here.

Instantaneous depths for isopycnals initially separated by ∼25cm in the vertical are determined for each ITP, and a daily mean is subtracted to retain higher-frequency vertical isopycnal displacements. A sinusoid with a specified frequency (chosen to be $\omega = 1.05f$) is least-squares fit to four-day segments of vertical displacement data. Sliding the sinusoid in one-day increments provides daily vertical displacement amplitude estimates A_η, which vary on a timescale of four days. To reduce the effect of instrument noise, data points from 5 adjacent isopycnals above and below each fit (spanning ∼3-9m in the vertical) are combined to provide 10x as many data points. This procedure assumes a typical wave is coherent over roughly 8 inertial periods and about 5m in the vertical.

In the analysis described herein, near-inertial wave amplitude estimates have been restricted to the upper water column, from just below the near-surface mixed layer, between ∼10m and ∼50m depth (Toole et al., 2010), to the top of the Atlantic Water layer at roughly 200m depth (Figure 3.2). This near-surface depth range is most relevant to an investigation of the interactions between wind, sea-ice, and ocean dynamics. The deepest density included in the analysis corresponds to the 1027.1kg m^{-3} isopycnal, chosen since it is consistently above

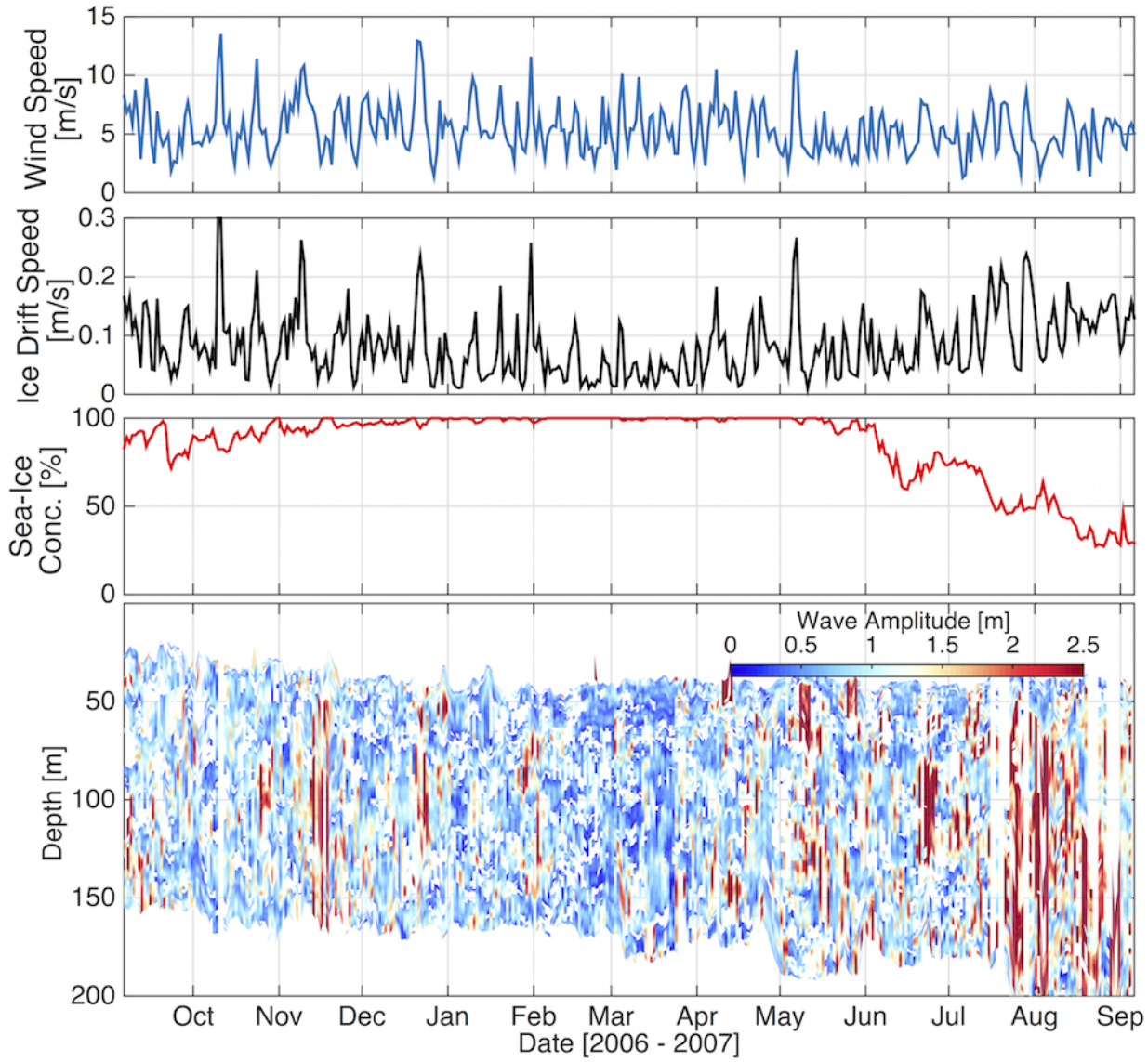

Figure 3.2: One year of data from a single ITP instrument (ITP 6) for wind speed, sea-ice drift speed, percent sea-ice concentration, and near-inertial internal wave vertical displacement amplitude from below the mixed layer down to roughly 200m depth.

the Atlantic Water layer.

The significance of each amplitude estimate is characterized by the R^2 value of the least-squares fit; amplitudes from fits explaining 25% or less of the variance in the data are excluded. Uncertainty in the remaining estimates (95% confidence interval) is determined from ensemble Monte-Carlo simulations, which account for instrument noise and uncertainty in isopycnal depth, aliasing of high-frequency motions associated with the internal wave continuum, and the effect of specifying a particular frequency for the fit. $\omega = 1.05f$ explains the most variance in the measured isopycnal displacements. However the results are fairly insensitive to this choice, with a reduction in variance explained of 5% or less for ω in the range $0.9 - 1.1f$. The energy in a near-inertial wave is proportional to the vertical displacement amplitude squared, but highly dependent on intrinsic wave frequency. While an increase in the average wave amplitude indicates an increase in the overall energy of the wave field, values of energy cannot be precisely quantified using ITP data since exact wave frequencies cannot be determined.

The total uncertainty in a given amplitude estimate A_η is the sum of a relative uncertainty of $\pm$25-40% A_η, which varies by latitude due to the changing Coriolis frequency, and an absolute uncertainty of between $\pm$0.5-1.5m, with 95% of amplitudes accurate to within $\pm$1m or better. The majority of wave amplitude estimates are statistically significant and explain on average 60% of the variance in the data points. Amplitude estimates for a given time are likely not independent over the depth range considered, and are also dependent over the four-day segment used for the fit. Accounting for this, the total number of amplitude estimates included in (for example) a monthly average results in negligible total uncertainty.

The distribution of calculated wave amplitudes over the upper water column is non-normal, with a long tail, as expected for internal waves (Figure 3.3c). Since the distribution is not Gaussian, the mean and the median differ, with the mean being skewed high. The median of the distribution is used for the analysis herein for any calculation of 'depth-average' or 'time-average', to characterize a 'typical' wave amplitude. As a result, most average values

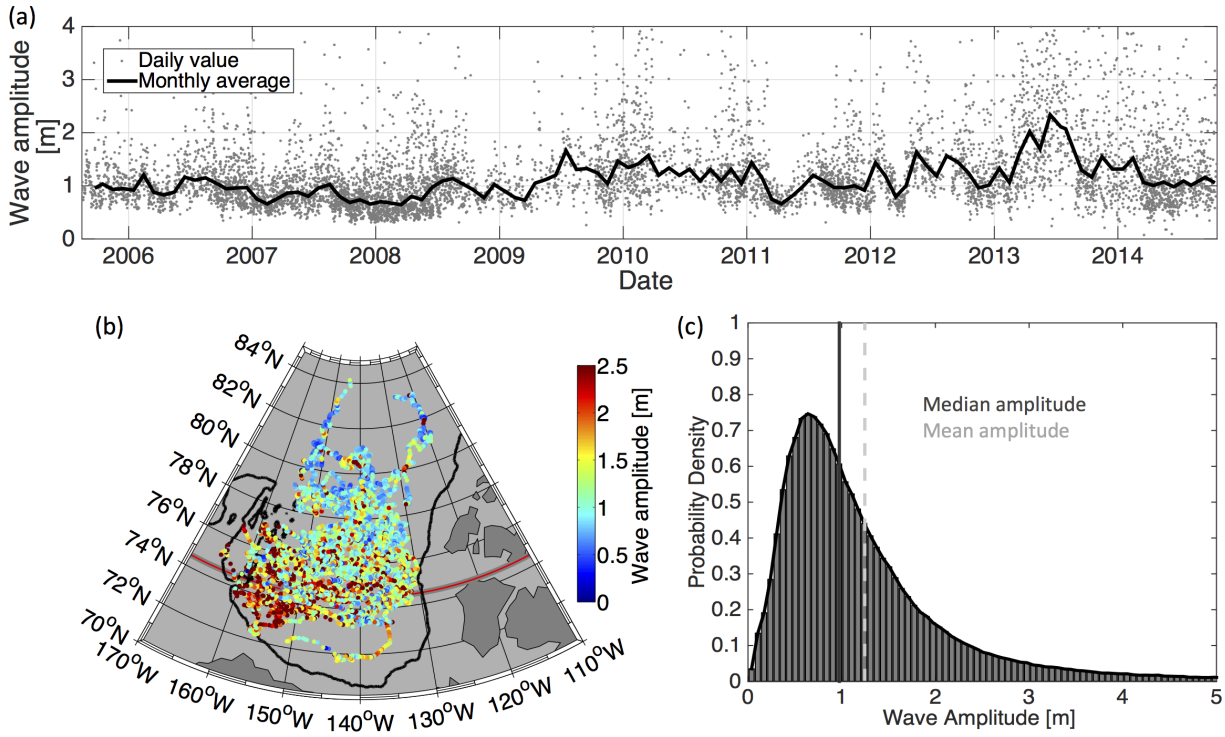

Figure 3.3: (a) Time series of individual measurements (grey dots) and monthly averages (black line) for the depth-averaged near-inertial wave vertical displacement amplitude from Fall 2005 to Fall 2014. Labels mark the 1st of Jan of each year. (b) Spatial map of depth-averaged wave amplitude following the ITP tracks from 2005 to 2014. Black line: 1000m isobath. Red line: critical latitude for the M2 semi-diurnal tide at 74.5^{o}N. (c) Probability density distribution of calculated near-inertial wave amplitude estimates from all ITP data considered herein. Dark and light grey lines indicate the median and mean amplitude for the distribution, respectively.

reported will be slightly lower than if the mean were used. The key findings of this paper hold regardless of whether the median or mean is used.

To provide an uncertainty estimate for a calculated median wave amplitude, bootstrapping is used (Efron and Tibshirani, 1993). This method provides an estimate of the standard error of the median for a non-normal distribution, and is typically very small ($\mathcal{O}(10^{-3}\text{m})$) for the near-inertial wave field due to the well-sampled wave amplitude distribution. When the standard deviation is reported below, it serves as a measure of the variability in the wave field about the median value, equal to the square root of the variance. The standard deviation is often large (0.7m in Figure 3.3c), owing to the high variability in wave amplitude on a range of temporal and spatial scales and to the long tail of the amplitude distribution.

3.5 Results

The complex demodulation technique applied to the ITP dataset allows for an assessment of the near-inertial wave field spanning nearly 10 years (Figure 3.3a) - the first record of such length for internal waves in the Arctic Ocean. As a result of the drift of the sea ice in which the ITPs are anchored, measurements of the near-inertial internal wave field capture variations in both time and space. During the time period analyzed, the ITPs transited a significant fraction of the Beaufort Gyre (Figure 3.1). If the entire data record is viewed as a spatial map (Figure 3.3b), bearing in mind that every measurement corresponds to a different time, possibly separated by years, then spatial patterns in the near-inertial wave field can be investigated across a large fraction of the Canada Basin. If the entire data record is treated as a time series, both seasonal and interannual variations in the wave field can be quantified and compared to changes in wind forcing and sea-ice characteristics, providing insight into internal wave evolution in the Arctic over the last decade. With over 10^6 individual estimates of near-inertial wave vertical displacement, the resulting distribution of wave amplitudes (Figure 3.3c) provides a robust statistical basis for analysis.

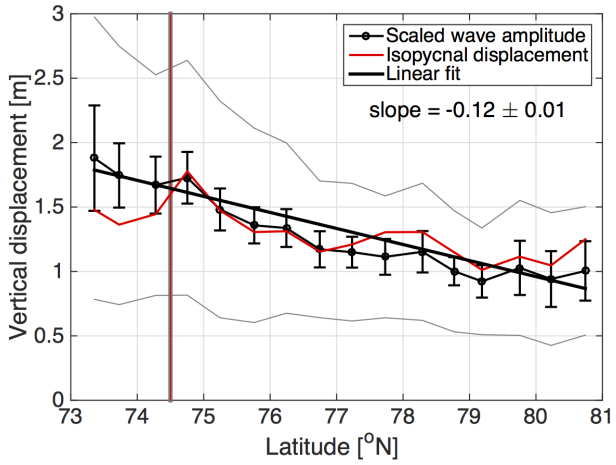

Figure 3.4: Average scaled near-inertial wave amplitude binned by half degree latitude (black line with markers), 2x rms (for comparison with amplitude) of high-frequency isopycnal displacements used for the wave fits binned by latitude (red line), linear fit to average wave amplitudes (black line). Grey lines show one standard deviation from the average wave amplitudes. Error bars are 95% confidence intervals based on standard error. The vertical red line indicates the critical latitude for the M2 semi-diurnal tide.

3.5.1 Spatial pattern

The dominant spatial pattern in the depth-averaged near-inertial wave field is a decrease in wave amplitude with increasing latitude (Figure 3.3b), with larger waves near the south of the Beaufort Gyre. To ensure that this pattern is not a result of the stratification in the region, which varies spatially, seasonally, and with depth, the amplitude estimates need to be normalized by a function of the stratification ([following the so-called Wentzel-Kramers-Brillouin approximation] Pedlosky (2003)). Stronger stratification suppresses isopycnal displacement and results in waves of smaller vertical displacement amplitude, A_η. To account for the effect of variations in stratification on the measured near-inertial wave field, a scaled wave amplitude, A_s, is calculated: $A_s = A_\eta\sqrt{(N(z)/N_o)}$, where $N(z)$ is the buoyancy frequency at each depth of each ITP profile and N_o is a constant reference buoyancy frequency, calculated as the dataset average. The scaled wave amplitude is used for all analysis hereafter.

The scaled wave amplitude displays a roughly linear decreasing trend with latitude (Fig-

ure 3.4), with only a slight increase below the critical latitude of the M2 semi-diurnal tide (74.5^oN). The standard deviation of the wave amplitude estimates also decreases with latitude. Assuming a linear trend, average wave amplitude decreases from 1.85 to 0.75m between 72^oN and 82^oN, a change of 12% per degree latitude (relative to the average wave amplitude). The rms sub-daily (high-frequency) vertical displacements of isopycnals in the water column also show a latitudinal trend (Figure 3.4), confirming that this spatial pattern is not an artifact of the complex demodulation technique described in Section 3.4.

Guthrie et al. (2013) hypothesized that the relatively weak internal wave signal in the Canada Basin was a result of the strength of the near-surface stratification. The scaled wave amplitude accounts for variations in the buoyancy frequency with depth, as well as the slight latitudinal variations across the Basin (Figure 3.5a). Note, however, that this scaling cannot account for the potential interactions between stratification features and the generation or propagation of individual internal waves. For example, inertial wind energy may result in mixed-layer deepening as opposed to near-inertial wave generation, or internal waves may reflect from double-diffusive layers in the Atlantic Water. While interesting, such impacts are outside the scope of the current work, as ITP data does not allow for a detailed analysis of either the generation of the propagation of individual internal waves.

The observed isopycnal displacements could also be associated with a semi-diurnal internal tide. Freely-propagating internal tides are possible south of the critical latitude for the M2 tide (74.5^oN), and across the whole basin for the weaker S2 tide. Some large wave amplitudes are observed south of 74.5^oN (Figure 3.3b). This area has a potential spatial / temporal bias caused by many ITP profiles taken near the shelf in the southwest corner of the Basin during the summer of 2013 (Figure 3.1, Appendix). Data very close to the shelf typically has more gaps and incomplete profiles due to the ITPs' rapid transit along the shelf, making it impossible to determine if the wave field has a spring-neap cycle. A trapped (evanescent) internal tide could cause elevated displacements near the Northwind Ridge and the Canadian Arctic Archipelago, where tidal current speeds are high. The central Canada Basin is smooth and far from rough topography, with small barotropic tidal currents (Figure

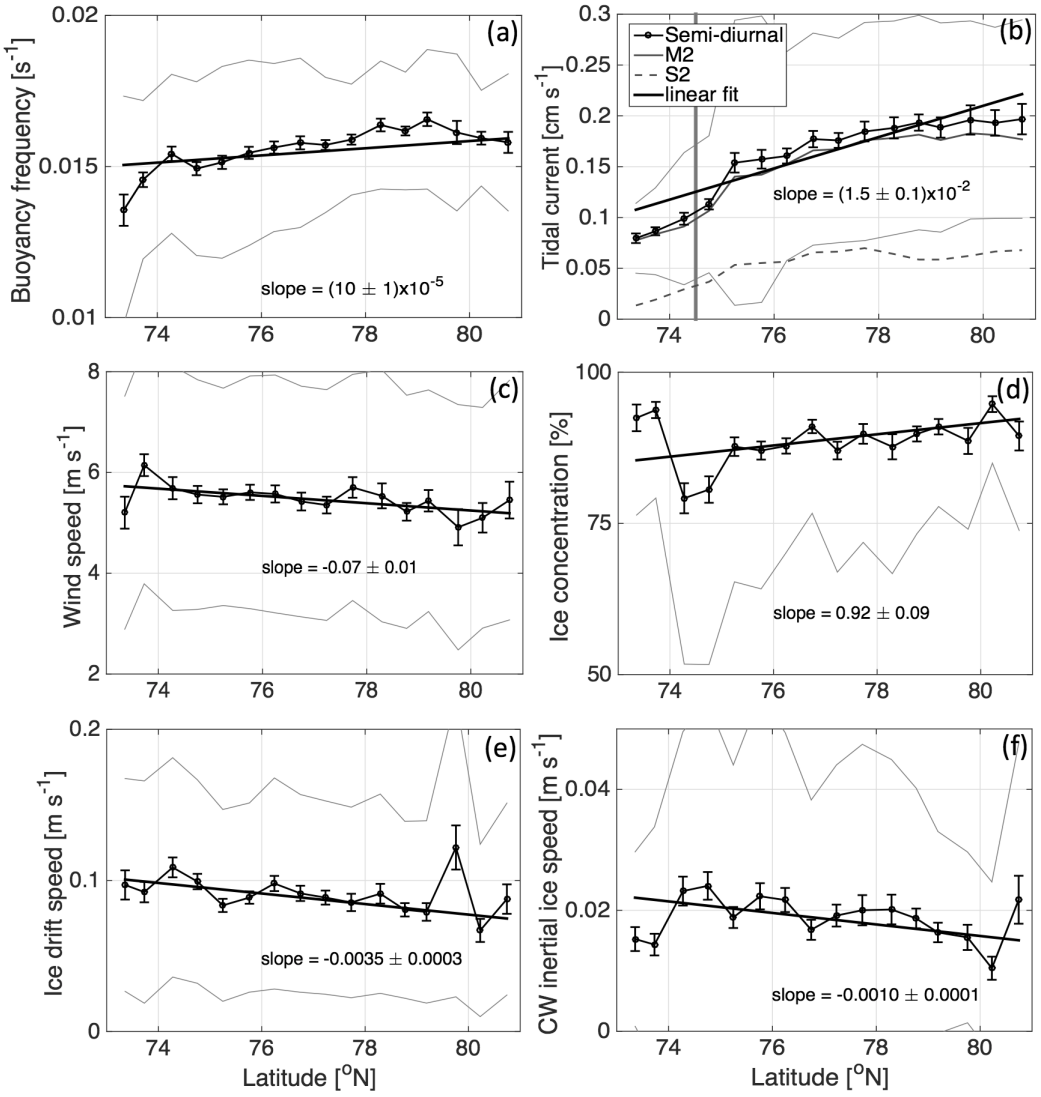

Figure 3.5: (a) Average buoyancy frequency, (b) tidal current speed for the semi-diurnal barotropic tide, (c) wind speed, (d) percent sea-ice concentration, (e) sub-inertial ice drift speed, and (f) clockwise inertial ice speed following the ITP tracks, binned by half degree latitude (black lines with markers), with linear fit (black lines). Grey lines: one standard deviation from the mean. Error bars: 95% confidence intervals based on standard error. In (b), the M2 (grey line) and S2 (dashed grey line) components are shown, as is the M2 critical latitude (vertical line).

3.5b). In fact, the semi-diurnal barotropic tidal current strength increases with latitude, which would result in larger internal tides to the north. Thus tidal forcing cannot explain the latitudinal trend in internal wave amplitude in the central Basin.

Internal waves generated at the inertial frequency are restricted to propagate equatorward, suggesting a possible accumulation of wave energy in the southern Basin. However the 'one-bounce' hypothesis of Pinkel (2005) predicts significant if not total wave dissipation in the under-ice boundary layer following a single reflection from the sea floor. If a significant fraction of near-inertial wave energy in the Canada Basin were to survive a single bounce, the wave field in the southern Basin would contain a combination of locally and remotely generated waves - with frequencies above the local inertial frequency. Further investigation would require determining if the peak in the internal wave spectrum around the local inertial frequency f is broader to the south in the Arctic, which is not possible using ITP data.

Comparison with the spatial distribution of wind speed, sea-ice concentration, and CW inertial and sub-inertial sea-ice drift speed shows no comparable latitudinal trend (Figure 3.5c-f) that can fully explain the trend in wave amplitude. [1] However, both wind and sea ice show variations with latitude that could potentially result in more energetic internal waves to the south. Slightly higher measured average wind forcing to the south, combined with increased open water, likely explains the more rapid ice drift and prevalence of inertial motions in the ice. These in turn could result in the generation of more energetic near-inertial waves, as could direct wind forcing on the open ocean. Changes in wind and ice concentration are only 1% per degree latitude toward the south, compared to the 18% increase per degree latitude for wave amplitude. Sea-ice CW inertial and sub-inertial drift speed increase by 7% and 5% per degree respectively, so may partially explain the variation with latitude in the near-inertial wave field. Other possible contributions to the spatial pattern in the wave field include the presence of older, thicker, more rigid sea ice to the north and east of the Canada Basin, and potential wave interactions with the eddy field. Further study is needed

[1] Spatial maps are in the Appendix for comparison with Figure 3.3(b).

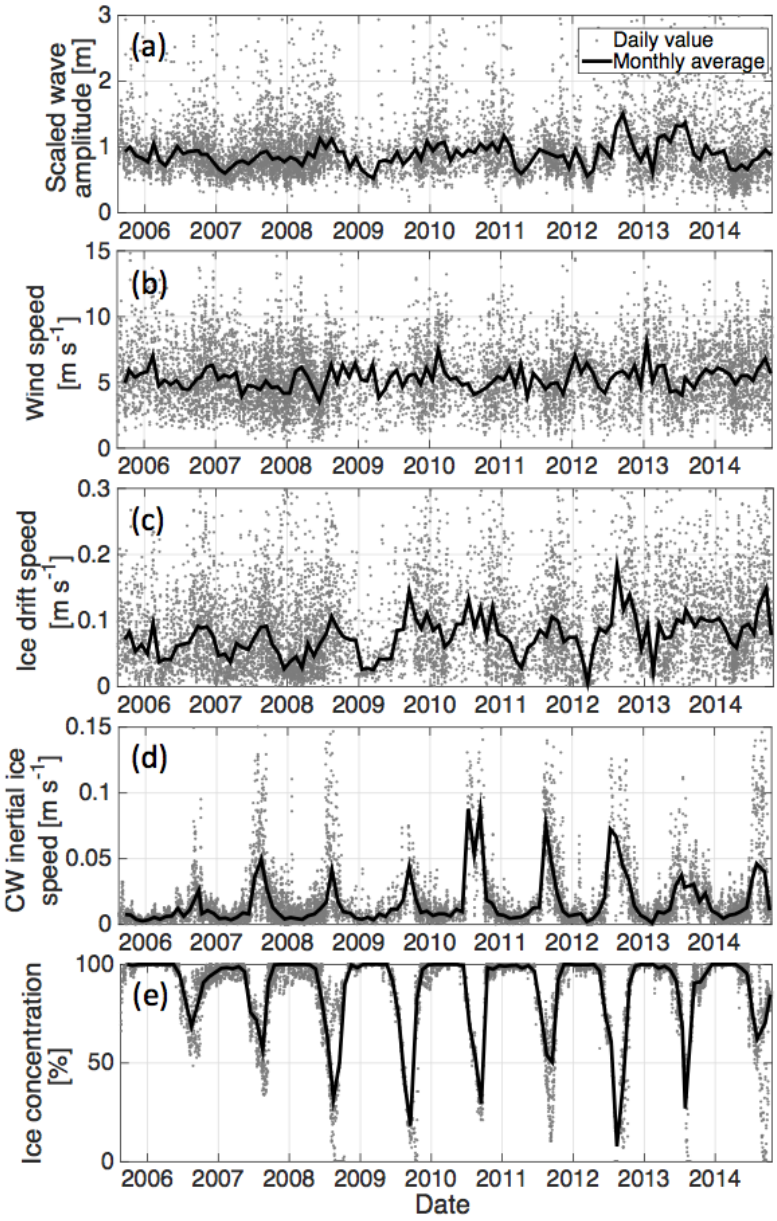

Figure 3.6: Individual measurements (grey dots) and monthly averages (black line) for (a) depth-averaged scaled near-inertial wave amplitude, (b) wind speed, (c) sub-inertial ice drift speed, (d) CW inertial ice speed, and (e) ice concentration, from Fall 2005 to Fall 2014. Labels mark the 1st of Jan of each year.

to determine the exact combination of causes.

The primary goal of this study is to examine the relationship between local sea-ice conditions and wind forcing and the near-inertial internal wave field. To better understand the relationship between the wind, the sea ice, and the internal waves, it is necessary to examine temporal as well as spatial variations. The presence of the large-scale spatial pattern acts to bias temporal measurements. To ensure that temporal variability is biased as minimally as possible by the decrease in wave amplitude with latitude, a linear fit to the latitudinal trend (Figure 3.4) is removed from the wave amplitude estimates. The results presented in the following Sections do not change significantly if this adjustment is not made. However temporal correlations are slightly higher when the large-scale north-south spatial pattern has been accounted for.

3.5.2 Temporal variations: Seasonal

The dynamics of the near-inertial wave field are influenced seasonally by both sea-ice properties and wind forcing. Unlike ice concentration and CW inertial ice speed, the near-inertial wave field does not immediately appear to be dominated by an obvious seasonal cycle (Figure 3.6), but is highly variable on both short (days to weeks) and long (seasonal to interannual) timescales, as are the wind and sea-ice drift speed.

Based on monthly average vertical displacement amplitude for all years from 2005 to 2014, the seasonal cycle in the near-inertial wave field (Figure 3.7a) has a maximum during the summer sea-ice melt period (August 1st - October 1st) when ice concentration (Figure 3.8b) and thickness are at their lowest, and a minimum in early spring when sea ice is at its thickest and most rigid (March 1st - May 1st). Wave amplitudes decrease through the fall during ice formation, then increase slightly in early winter (December 1st - February 1st), during a period of near-total sea-ice cover, when wind speeds are rising and strong winter storms occur frequently (Figure 3.8a). The magnitude of the seasonal cycle in the near-inertial wave field is small, on the order of 1/4 the average wave amplitude, but statistically significant. It is likely the ITPs may be underestimating the magnitude of the seasonal cycle,

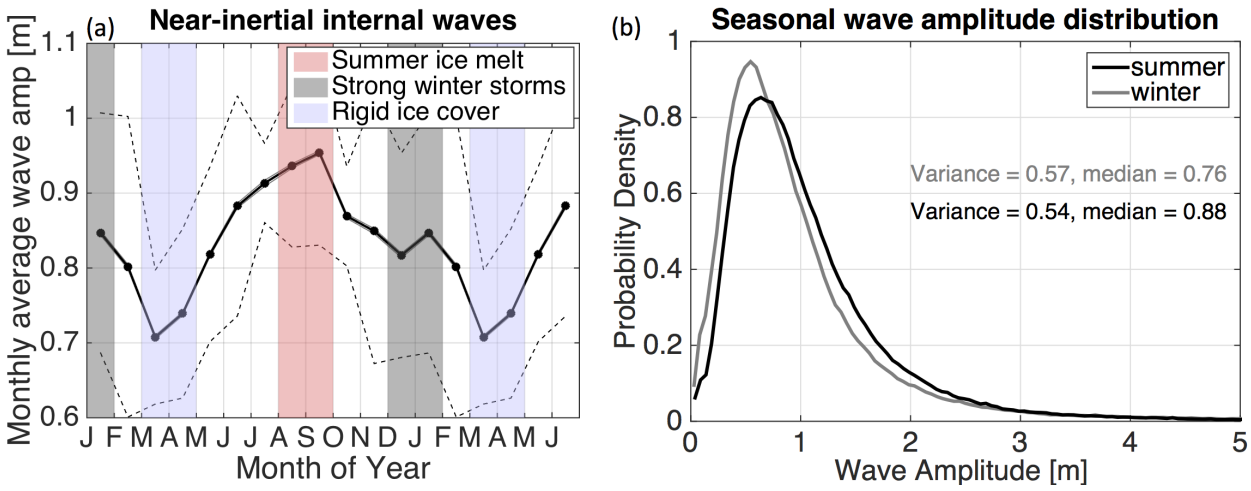

Figure 3.7: Seasonal variations in the near-inertial internal wave field. (a) Scaled vertical displacement wave amplitude estimates are binned by month (black dots). The annual mean has been removed for each year to avoid introducing an interannual bias, and the overall time series average has been added to the monthly anomalies to provide physical context. One standard deviation is shown by the dashed lines. The solid grey lines (nearly overlaying the black line) are uncertainty estimates from bootstrapping, which provides the standard error of the median for a non-normal distribution (95% level). Coloured bars show periods of interest. The months January through June have been repeated to show the complete, uninterrupted seasonal cycle. (b) Distribution of scaled near-inertial internal wave amplitudes for summer (June to November, black line) and winter (December to May, grey line). The variance and median for each distribution is given. The two distributions differ at the 95% confidence level based on a Kolmogorov-Smirnov significance test.

due to their infrequent sampling of open water and low-ice conditions.

While the uncertainty in the calculated monthly average wave amplitude is nearly negligible, the interannual variability in the seasonal cycle for near-inertial waves is high, as indicated by the standard deviation (Figure 3.7a). To determine the statistical significance of seasonal differences, the median amplitude of waves during summer (June to November) is compared to that during winter (December to May) and found to be significantly higher, indicating larger, more energetic waves overall during the summer (Figure 3.7b). While the summer and winter distributions of wave amplitude estimates are notably different, with the median wave amplitude 16% larger during June to November compared with December to May, their variances are similar.

Near-inertial waves and sea ice

The increase in near-inertial wave amplitude during summer is likely driven by two factors. First, summer sea ice is thin and patchy, providing maximum area for direct contact between the wind and the ocean's surface. Second, the sea ice is in free drift during summer, which may increase wave generation through resonant inertial responses in the sea ice to wind forcing. The resulting clockwise oscillations ice motion translate into inertial oscillations in the water column below. Note that the seasonal cycle for CW inertial ice speed (Figure 3.8d) has a sharp peak in summer matching the decrease in ice concentration during melt (Figure 3.8b).

Gimbert et al. (2012b) observed a small secondary peak in CW inertial oscillations in sea-ice drifter motion during the winter months, which is not seen in the ITP data. Overall, the seasonal variations in the near-inertial internal wave field do not follow those of the CW inertial ice speed. The ITPs may be underestimating CW inertial oscillations in the ice, as the instruments are typically deployed in large, thick ice floes that are less likely to regularly enter a state of rapid free drift. The impact of CW inertial ice motion on the near-inertial wave field may thus be an underestimate, particularly in summer.

Outside of the summer months, when the sea ice is a coherent pack with $\sim$100% con-

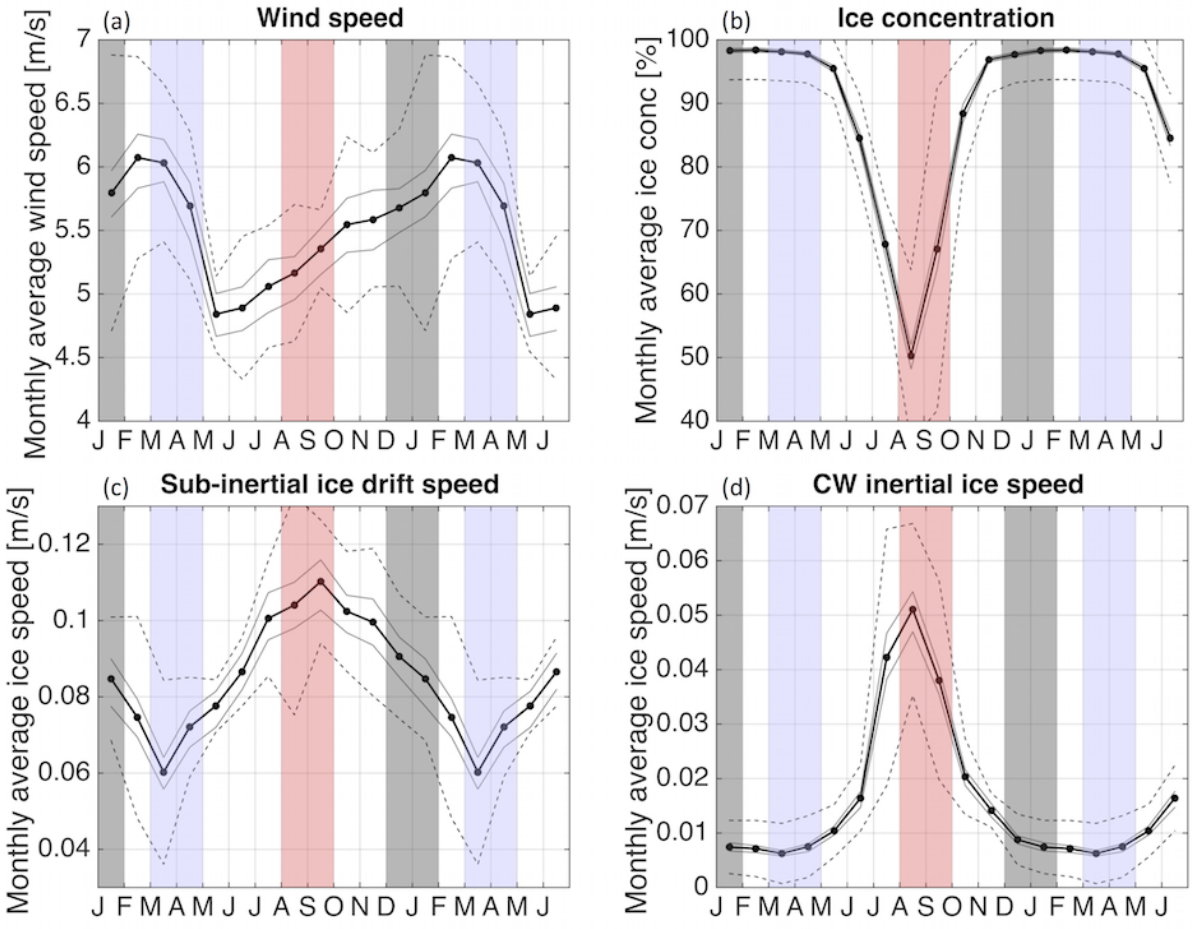

Figure 3.8: As in Figure 3.7a, but for the seasonal cycle in (a) wind speed, (b) sea-ice concentration, (c) sub-inertial ice drift speed, and (d) CW inertial ice speed.

centration and low CW inertial ice speeds, an alternate mechanism for wave generation is required to explain variations in the near-inertial wave field. The seasonal cycle for the sub-inertial ice drift speed (Figure 3.8c) agrees fairly well with that for the near-inertial waves. Sub-inertial ice motion can generate near-inertial waves when horizontal gradients in ice drift speed or bottom roughness induce a vertical velocity perturbation of the stratified water column at the resonant inertial frequency (McPhee and Kantha, 1989). The ice drift speed does not have a second peak in early winter, and increases more gradually than the near-inertial wave amplitude through the summer.

The wind speed, which drives sea-ice motion and is highly correlated with ice drift speed on short timescales (Hakkinen et al., 2008), is relatively small in summer when the wave field is most energetic and largest in winter when the wave field is at a minimum (Figure 3.8a). This is in contrast to the seasonal cycle for near-inertial waves at lower latitudes, which matches that of the wind forcing.

Near-inertial waves and wind factor

It seems likely that the amplitude of the near-inertial waves is strongly affected by the ease of momentum transfer from the wind through the sea ice to the stratified ocean below. The properties of the ice that impact momentum transfer are not available for this analysis, but their effect on ice motion is simplistically represented by the 'wind factor', the ratio of the ice drift speed to the wind speed. Martini et al. (2014) found that the wind factor had some agreement with the near-inertial internal wave field near the continental slope of the southern Canada Basin on weekly timescales.

The wind factor is calculated as:

$wind\ factor = |\vec{u}_{ice}|/|\vec{u}_{wind}|$,

assuming ocean current speeds are low relative to sea-ice drift speed (Wadhams, 2000). For consistency with the available 4x daily re-analysis data for wind speed, sub-inertial ice drift speed is used. This excludes the inertial component of wind forcing and sea-ice motion from the calculated wind factor values. If the ice is in free drift, the wind factor can be related

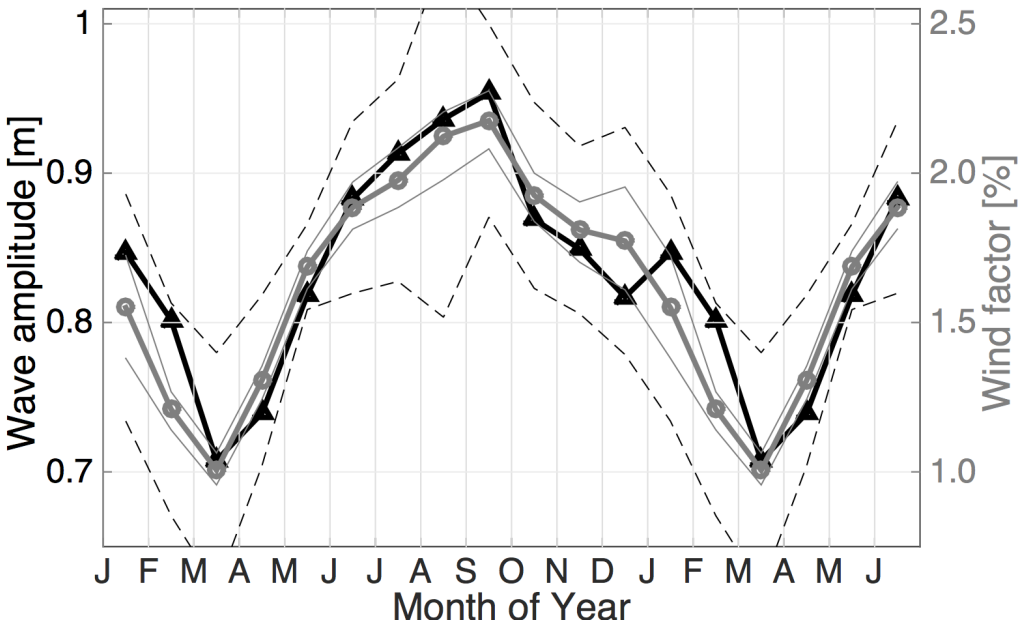

Figure 3.9: Near-inertial internal wave amplitude data binned by month is repeated from Figure 3.7a (thick black line), and compared with the wind factor (thick grey line). January through June are repeated to show the uninterrupted seasonal cycle. One standard deviation (dashed lines) and bootstrapped uncertainty estimates (thin grey lines) are shown for the wind factor.

to the ratio of the air-ice to ice-ocean drag coefficients (Wadhams, 2000). If the ice is not in free drift, internal ice stresses will affect the ice speed, which in turn modifies the wind factor.

If the wind factor is high, it indicates that the wind can move the ice easily. This may be because the ice-ocean drag is low, because the ice surface is rough, so that the air-ice drag is high, or because internal ice stresses are weak. If the ice cover is patchy and in free drift, the air-ice drag will increase due to the increase in form drag. If the wind factor is low, sea ice is resistant to wind-driven motion. This may be because the surface of the ice is smooth, so that the air-ice drag is low; because the bottom of the ice is rough, so that ice-ocean drag dominates; or because internal ice stresses are limiting the ice response to the wind forcing.

Comparing seasonal variations in the wind factor with those in the near-inertial internal wave field shows very good agreement (Figure 3.9). During summer, even relatively weak wind forcing can easily accelerate the ice, leading to a peak in ice speed and thus in wind factor. The strength of the ice response decreases to a minimum in March, matching the minimum in the near-inertial wave field.

The wind factor plateaus in early winter but does not show a second peak like that in the near-inertial wave field. During this time period, wind forcing is increasing but the sea-ice response decreases. This could be caused by variations in air-ice and ice-ocean drag, or by changes in the rigidity and internal stresses of the ice pack. The close agreement between the near-inertial wave field and the wind factor suggests that seasonal variations in the energy of the Arctic internal wave field are caused by sea-ice properties that determine how readily the ice responds to wind forcing.

3.5.3 Temporal variations: Interannual

Interannual variability in the vertical displacement amplitude of near-inertial internal waves (Figure 3.10) is significantly correlated with the wind factor ($r = 0.6$). Neither the wind speed nor sea-ice concentration alone can explain the variations in near-inertial wave amplitude on these timescales. Note that the peak in near-inertial wave amplitude during the summer of

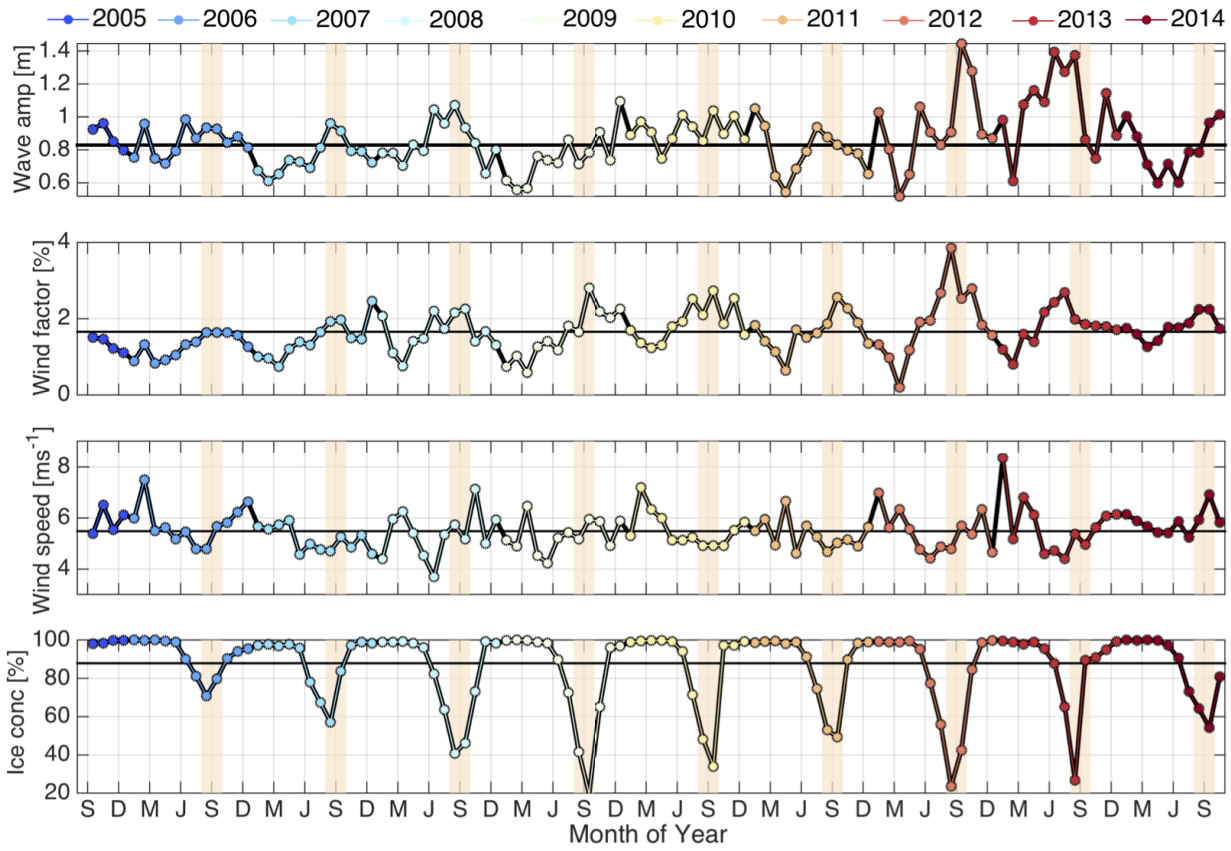

Figure 3.10: Interannual variations from Fall 2005 to Fall 2014. Data is binned by month and coloured by calendar year, matching Figure 3.1. From top to bottom, fields are: scaled near-inertial wave vertical displacement amplitude, wind factor, wind speed, and sea-ice concentration. Tan vertical bars indicate the summer sea-ice melt from Aug 1st to Oct 1st. Horizontal black lines give the overall time series average for each field.

2013 may be partially caused by a spatial bias due to an unusually high number of ITPs drifting near the continental slope in the south-west corner of the Basin, south of the critical latitude for the M2 tide. The high correlation with the wind factor should not be construed as an indication of a linear relationship between wind factor and wave amplitude, but rather as a suggestion that seasonally varying sea-ice properties impacting ice speed are important to the average energy of the wind-generated near-inertial wave field.

Compared to pre-2008 values, the median near-inertial wave amplitude (Figure 3.11) is slightly higher for the periods 2008-2011 and 2012-2014. The variance in the distribution of near-inertial wave amplitude estimates doubles between the early part of the record (pre-2007 sea-ice minimum) and the later part of the record (post-2012 sea-ice minimum). This increase in variance in later years indicates an overall broadening in the distribution of wave amplitudes, with a higher probability of large waves. Results are significant at the 95% confidence level based on a Kolmogorov-Smirnov significance test for the difference between distributions.

Interannual trends in the near-inertial internal wave vertical displacement amplitudes are small but significant during both the summer (Figure 3.12a) and the winter (Figure 3.12b) seasons, with 1.0% per year and 2.5% per year increases in wave amplitude respectively (Table 3.1). The trend in the winter months may be influenced by unusually large waves associated with the 2012 sea-ice minimum. In fact, the highest average wave amplitude for both summer and winter occurs during 2012.

The variance of the wave field (Table 3.1) increases dramatically by 11% per year (based on a linear trend) for wave amplitude estimates during summer (Figure 3.12c) and by 15% per year for the winter (Figure 3.12d). The winter trend is largely driven by changes occurring around the time of the second peak in the seasonal cycle, and may be related to the timing of the sea-ice freeze-up. The summer trend could be caused by an increase in the variance of inertial ice speed during the summer, or by the higher likelihood of open water in the vicinity of the ITPs.

Sea-ice concentration trends (Table 3.1) show a decline during the summer at a rate of

	Trend		Variance	
Field	**Summer**	**Winter**	**Summer**	**Winter**
Near-inertial wave amplitude	$(10 \pm 9) \times 10^{-3}$m/yr +1.0%/yr	$(22 \pm 9) \times 10^{-3}$m/yr +2.5%/yr	(0.04 ± 0.02)m^2/yr +11%/yr	(0.06 ± 0.01)m^2/yr +15%/yr
Wind factor	(0.071 ± 0.005)%/yr +5%/yr	(0.059 ± 0.005)%/yr +6%/yr	(0.06 ± 0.04)%^{2}/yr +9%/yr	(0.05 ± 0.03)%^{2}/yr +9%/yr
Wind speed	(0.04 ± 0.01)m s^{-1}/yr +0.7%/yr	(0.03 ± 0.01)m s^{-1}/yr +0.5%/yr	(0.0 ± 0.1)m^2 s^{-2}/yr +0.6%/yr	(0.0 ± 0.1)m^2 s^{-2}/yr +0.4%/yr
Sea-ice concentration	(-1.2 ± 0.1)%/yr −1.4%/yr	(0.09 ± 0.02)%/yr +0.1%/yr	(56 ± 30)%^{2}/yr +17%/yr	(0.3 ± 0.6)%^{2}/yr +5%/yr
CW inertial sea-ice speed	(1.7 ± 0.1)mm s^{-1}/yr +10%/yr	(0.44 ± 0.04)mm s^{-1}/yr +7%/yr	(40 ± 20)mm^2 s^{-2}/yr +18%/yr	(6 ± 2)mm^2 s^{-2}/yr +26%/yr
Sub-inertial sea-ice speed	(3.8 ± 0.3)mm s^{-1}/yr +5%/yr	(3.3 ± 0.3)mm s^{-1}/yr +5%/yr	(130 ± 40)mm^2 s^{-2}/yr +4%/yr	(170 ± 70)mm^2 s^{-2}/yr +6%/yr

Table 3.1: **Trend** column - Interannual trends for summer (June to November) and winter (December to May) calculated as the slope of a least-squares fit to the data. **Variance** column - Interannual trends in the variance of each field during summer and during winter. The relative %-change per year is reported below each absolute trend value.

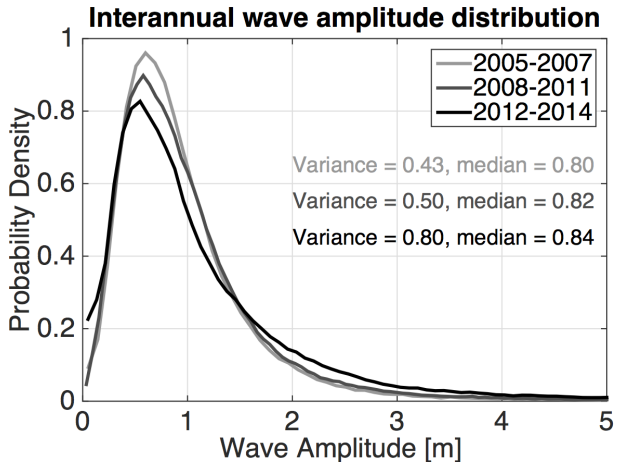

Figure 3.11: Distribution of scaled near-inertial wave amplitude from 2005 to 2007 (light grey line), from 2008 to 2011 (grey line), and from 2012 to 2014 (black line). The variance and median of each distribution is given. Differences are significant at the 95% confidence level based on a Kolmogorov-Smirnov significance test.

-1.4% per year, consistent with previous observations of total Arctic sea-ice extent (Comiso et al., 2008), with a +17% per year rise in variance associated with the increased frequency of low ice concentrations. Although wind speed only marginally increases over the course of the record and does not show any significant increase in variance along the ITP tracks, both CW inertial and sub-inertial ice speed have positive interannual trends in magnitude and variance (Table 3.1), with a +26% per year increase in the variance of CW inertial ice speed during the winter months. The percent increases per year in wind and ice drift speed are comparable to Arctic-wide trends from Spreen et al. (2011) for the period 2004-2009.

The wind factor has somewhat larger interannual trends than the near-inertial wave field (Table 3.1) during both summer and winter, but comparable increases in variance. This may reflect increased variance in the sea-ice speed, and/or increased variability in sea-ice properties, particularly as large amounts of multiyear ice melted out of the Canada Basin during this decade.

These results reflect the trajectories of the ITPs, and not overall Canada Basin aver-

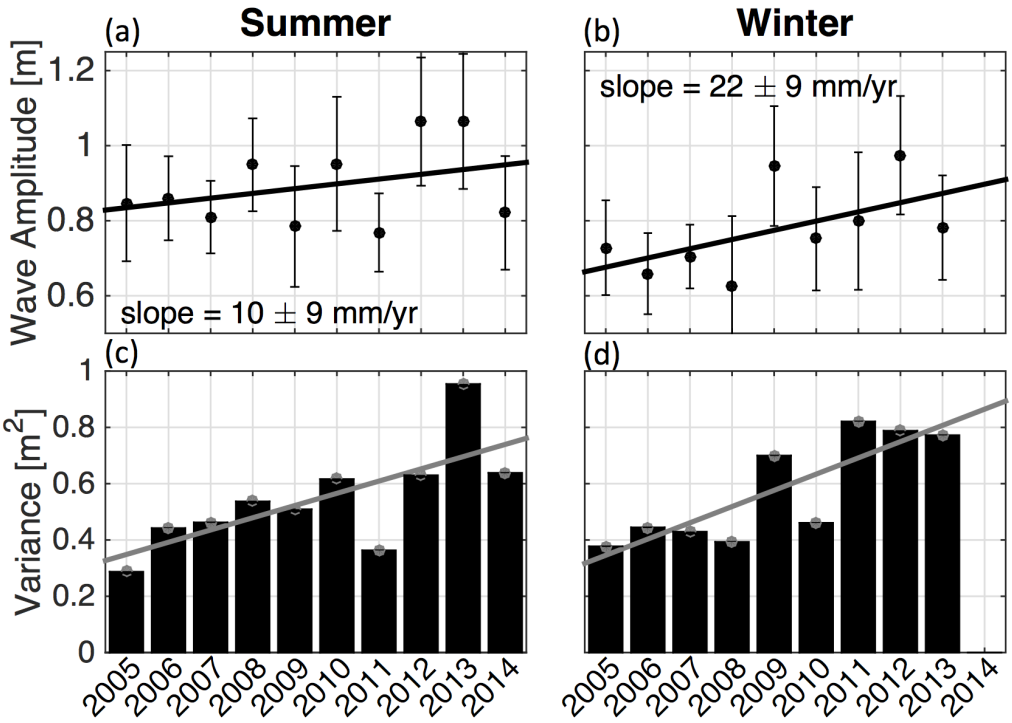

Figure 3.12: Interannual trend in scaled near-inertial wave amplitude for (a) summer (June to November) and (b) winter (December to May). Dots correspond to the average value for each year e.g. Winter 2005 is the December 2005 to May 2006 average. The black line is a linear fit with the given slope. Errorbars give 95% confidence intervals based on standard error. Variance in the wave field by year is shown for (c) summer and (d) winter. Grey lines are linear fits.

ages. Despite the purposeful deployment of ITPs in large ice floes, the overall change in observed sea-ice characteristics during the last decade is still apparent, as the Canada Basin transitioned from a thicker, multiyear ice pack to relatively younger, thinner ice cover. Accompanying the slight increase in the overall energy of the near-inertial wave field, evidence suggests that the declining sea ice is driving an increase in the frequency of unusually large near-inertial waves. The episodic generation of these large amplitude waves would cause intermittent spikes in the energy of the wave field.

3.6 Discussion: Dynamics of the near-inertial wave field

Key results for the near-inertial internal wave field include: 1) The presence of a latitudinal trend in wave amplitude, with larger waves in the south of the Canada Basin, 2) A seasonal cycle in wave amplitude, with monthly variations closely matching those in wind factor, and summer sea-ice conditions associated with more ice motion and a more energetic wave field, and 3) A slight interannual trend in wave amplitude linked to decreased sea-ice concentration and increased ice speeds, and a large interannual trend in variance suggesting that the generation of highly energetic near-inertial internal waves is on the rise.

3.6.1 Near-inertial wave generation

Interpretation of the agreement between near-inertial wave amplitude and the wind factor on seasonal to interannual timescales must necessarily consider how wind forced sea ice results in wave generation. The seasonal agreement between the two (Figure 3.9) is closely tied to the seasonal cycle in sub-inertial ice drift speed (Figure 3.8c). The wind factor should not be viewed as a predictor or driver of near-inertial wave generation, but rather as a 'rule of thumb' for the typical Arctic sea-ice response to wind forcing (Wadhams, 2000), which is itself the primary driver of Arctic internal wave generation.

Internal wave generation is not directly captured by the ITPs, and the uncertainty in individual wave amplitude estimates from ITP data can be up to $\pm$1m, as discussed in Section 3.4. Despite this, short timescale correlations (days to weeks) between wind forcing,

sea-ice properties, and wave amplitude suggest how wave generation is affected by changing conditions. Individual estimates of wave amplitude were correlated to daily averaged wind speed, ice speed, ice concentration and wind factor. [2] The wave amplitude time series has a low but significant correlation with wind speed ($r = 0.2$ at the 95% level), wind factor ($r = 0.2$), and ice drift speed ($r = 0.3$). Wind speed correlates strongly with sea-ice drift speed ($r = 0.6$), indicating that sea-ice motion is closely tied to changes in the wind on short timescales, despite the lack of agreement on seasonal and interannual timescales. This matches findings from Thorndike and Colony (1982), who found that geostrophic winds accounted for over 70% of the variance in daily sea-ice motion, a result that was corroborated by Rigor et al. (2002). When lagged by 1-3 days, correlations rise slightly, but remain below $r = 0.5$, suggesting a finite amount of time for momentum transfer from the wind, through the sea ice and mixed layer, into internal wave generation.

Neither sea-ice concentration nor CW inertial ice speed are significantly correlated with the near-inertial wave field for the full record on a daily timescale. Over shorter time periods - months to seasons as opposed to the entire record - correlations between different fields and the near-inertial waves are often higher, suggesting seasonal variations in the mechanisms behind internal wave generation. In particular, correlations between the near-inertial waves and the CW inertial ice speed are generally significant during the summer (though still typically low), when the ice is in free drift. Low correlation values are likely partially due to the limitations of the ITPs (which cause large uncertainties in individual wave amplitude estimates as discussed in Section 3.4) and also to an internal wave field that is no doubt composed of both locally and remotely generated waves.

Wind factor does not well explain variations in the near-inertial internal wave field on daily timescales, and what agreement there is is likely attributable to the (slightly higher) correlation with ice drift speed. There is no reason to expect a direct linear relationship between wind factor and the amplitude of any given wave. In fact, rather than a proportional

[2] Associated scatterplots are in the Appendix.

increase in wave amplitude for a given increase in either wind or ice speed, it is the timing of wave generation that seems to be driven by an increase in wind forcing accelerating the sea ice, as demonstrated qualitatively in the case study below.

In turn, the ice motion forces a near-inertial wave, either through variations in horizontal sub-inertial drift speed or through inertial ice motion. The wind factor acts as a simple proxy for sea-ice properties that affect the ice response, which could include ice thickness, strength, age, roughness, internal stresses, and amount of open water or ice in free drift. Wind factor thereby provides information about how such properties affect the average energy of waves generated on longer timescales.

For example, the near-inertial wave field (Figure 3.7a) is more energetic during May to August than during October to January, despite similar values of the average monthly sub-inertial ice drift speed (Figure 3.8c) for the two periods. Wind speeds are lower (Figure 3.8a) and the wind factor is higher (Figure 3.9) in May-August than October-January, indicating that sea-ice properties during summer allow the ice to respond more readily to wind forcing.

Exactly how various sea-ice properties affect near-inertial wave generation remains an open question that cannot be addressed by the ITP dataset at present. A complete understanding would likely require detailed information on not only local sea-ice characteristics, but also inertial current speeds in the mixed layer, on both daily to weekly and seasonal timescales.

3.6.2 Case study - ITP 41

To better understand the connections between short timescale variations in the wave field, wave generation, and the seasonal and interannual patterns previously identified, ITP 41 is used as a case study (Figure 3.13). This record begins in October 2010 and runs through July 2012.

During the summer melt, near-inertial wave amplitude is elevated on daily and monthly timescales. The is associated with a rapid decrease in ice concentration and increase in CW inertial ice speed (Figure 3.13a). The ice is likely patchy, thin, and weak, in free drift,

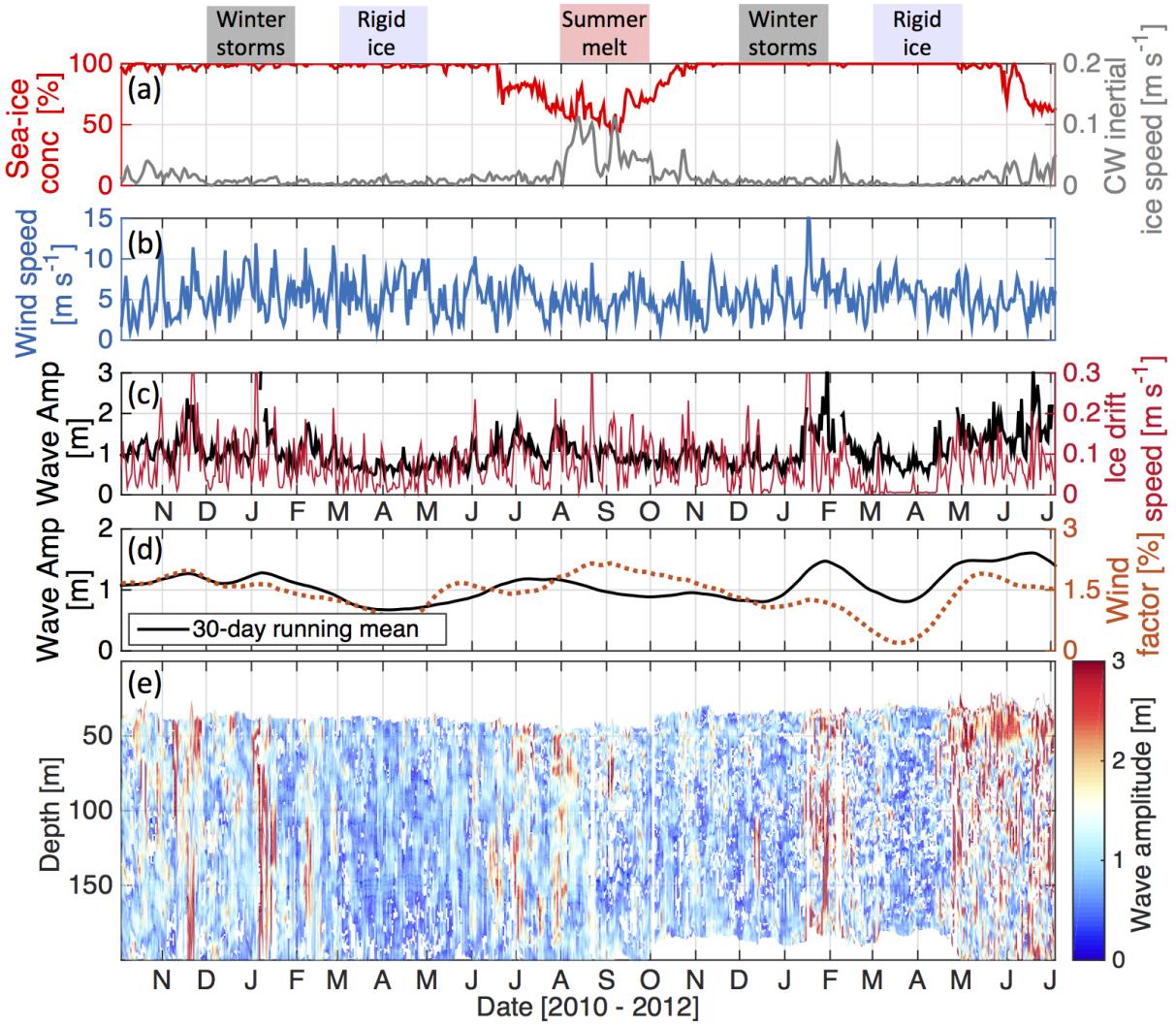

Figure 3.13: Data from October 2010 to July 2012. Near-inertial internal wave amplitude estimates and ice speed are from ITP 41. (a) Daily average sea-ice concentration and CW inertial ice speed. (b) Daily average wind speed. (c) Daily average sub-inertial ice drift speed (thin red line) and depth-average near-inertial wave amplitude (thick black line). (d) 30-day running means of wind factor (dashed orange line) and depth-average near-inertial wave amplitude (solid black line). (e) Near-inertial internal wave vertical displacement amplitude with depth and time. Coloured bars show seasonal periods of interest as in Figure 3.7a.

increasing momentum transfer from the wind to the ocean. Wave generation is expected to be predominantly due to wind forcing driving an inertial response in the ice cover, which then translates into the mixed layer and the water column below.

In fall and early winter, near-inertial wave amplitude increases sharply during several significant storm events, in which wind speeds exceed 10m s^{-1} (Figure 3.13b). Ice concentration is close to 100%, though it sometimes drops slightly during a storm as wind forcing perturbs the newly formed ice. Storms cause an increase in sub-inertial ice speed, and sometimes in inertial ice speed (Figure 3.13a-c), presumably depending on ice characteristics. The timing of individual wave generation events is therefore tied to storms driving horizontal variations in ice drift, which causes vertical inertial pumping at the base of the mixed layer. Particularly energetic periods are also accompanied by an increase in inertial ice oscillations driving an inertial response in the mixed layer.

During late winter (March and April), the near-inertial internal wave field is at a minimum (Figure 3.13c), though waves continue to be generated (Figure 3.13c,e). Wind speeds are high, but sea ice is at 100% concentration and is likely thick and rigid, with high internal strength that limits ice deformation. Both inertial and sub-inertial ice speeds are small and less variable, suggesting that the wind is unable to transfer momentum effectively to the ice, even during storms. This record is from recent years, when less multiyear ice was present in the Canada Basin. Momentum transfer from wind forcing to sea-ice motion in winter may have been further reduced by the lower drag coefficient for first-year ice compared to multiyear ice (Wadhams, 2000).

During all seasons, variations in the wind factor are similar to those in the near-inertial wave field on longer (weekly to monthly) timescales (Figure 3.13d). The timing of individual wave generation events is linked to rapid variations in wind and thus sea-ice speed, while the overall momentum available for wave generation on seasonal and interannual timescales appears to be determined by ice characteristics that affect air-ice and ice-ocean drag and internal ice stresses, and are here simplistically reflected by the wind factor.

3.7 Summary

The near-inertial internal wave field is quantified using nearly a decade (2005-2014) of observations from drifting Ice-Tethered Profilers in the Beaufort Gyre region of the Canada Basin. Vertical displacement amplitude for near-inertial waves is compared to wind speed, sea-ice concentration and ice drift speed to determine how wind-ice-ocean dynamics have affected Arctic internal waves over the last decade, both spatially and on seasonal and interannual timescales.

The near-inertial wave field displays a spatial pattern consistent with a linear decrease in vertical displacement wave amplitude of 12% per degree latitude to the north, decreasing by over 1m on average between 72^oN and 82^oN. This pattern may be partially explained by slightly elevated wind and ice speeds, and lower sea-ice concentration in the south of the Canada Basin. The latitudinal trend in wave amplitude could also be caused by the strictly southward propagation of internal waves generated at the inertial frequency. This is inconsistent with the idea that internal waves are dissipated in the under-ice boundary layer following a single reflection from the sea floor (Pinkel, 2005), although it is possible that the under-ice boundary layer (Morison et al., 1985) is becoming less dissipative. Further investigation is necessary to determine the exact causes of this spatial pattern.

On a seasonal timescale, near-inertial internal waves are largest during the summer months, with a second peak in late fall as wind forcing increases, and a minimum in late winter. Median wave amplitude is 16% larger during summer and fall (June to November) than during winter and spring (December to May). Both seasonal and interannual variations in the near-inertial internal wave field are found to match changes in the wind factor, the ratio of sub-inertial ice drift speed to wind speed. Momentum transfer varies based on the characteristics of the sea ice, such as ice concentration, thickness, roughness, form drag, and internal ice stresses. Many of these properties are reflected in how readily the wind is able to accelerate the sea ice, which is simplistically captured by the wind factor.

There is a small but significant interannual trend during both the summer and winter

months, with a 5% increase in the median amplitude of the near-inertial waves over the course of the record, paralleling the decline in sea-ice cover during the summer and the increase in sea-ice speed during both summer and winter. More importantly, the variance in the distribution of near-inertial wave amplitudes doubles between the years 2005-2007 and 2012-2014, with an 11% increase in variance per year during summer and a 15% increase in variance per year during winter. Therefore, while the average amplitude of near-inertial waves is only slightly larger in recent years, unusually large waves are generated much more frequently.

Near-inertial internal wave generation in is known to occur due to horizontal variations in sea-ice velocity (or wind velocity over open water) driving vertical inertial pumping at the base of the mixed layer. During summer free drift or a strong winter storm, the wind can excite a clockwise inertial response in the sea ice. Large inertial ice speeds are highly intermittent and cannot fully explain the seasonal cycle in the near-inertial waves. Some agreement is found between near-inertial wave amplitude estimates and sub-inertial ice drift speed. While the timing of near-inertial wave generation matches rapid variations in wind and sea-ice speed, the average energy in the wave field on seasonal timescales is more closely tied to how readily the ice responds to wind forcing, suggesting that changing ice characteristics - such as the continued dramatic reduction in multiyear sea ice in the Canada Basin - are impacting the energetics of the Arctic internal wave field.

The ITPs do not directly measure internal wave generation, and cannot be used to distinguish between locally generated downward propagating waves, and remotely generated upward propagating waves. They lack sufficient time resolution to measure the internal wave frequency spectrum, so do not provide accurate estimates of internal wave energy. Despite these limitations, the ITP dataset has provided unique information about the spatial, seasonal, and longterm evolution of the near-inertial wave field in the Arctic, and brought to light potential connections between wind forcing, local sea-ice properties, and the resulting internal waves.

The near-inertial internal wave field in the Canada Basin has become increasingly ener-

getic and variable over the last decade, reflecting a fundamental shift in year-round sea-ice characteristics in the Arctic Ocean. As the properties of the sea ice continue to change, the internal wave field will likely continue to evolve as well. This may have important implications for mixing in the upper ocean due to wave overturning and dissipation, as the most energetic waves are those most likely to become unstable and break. Any resulting increase in mixing would influence the vertical flux of heat and nutrients, and possibly weaken the stratification of the upper halocline.

3.8 Appendix: Details and biases of ITP sampling

The analysis herein uses data from 27 ITPs which completed density profiles and recorded hourly GPS position between August 2005 and October 2014 (Figure 3.14) in the Beaufort Gyre region of the Canada Basin (72^oN to 82^oN and 130^oW to 160^oW). Measurements were made during all months of the year for all years within that timespan. ITPs which profiled for only a month or two before failing were excluded from the analysis, as were those ITPs whose drift tracks were outside the study region. The 30364 profiles used in the analysis represent 85% of the total number of ITP profiles recorded in the Canada Basin. As such, the information in Figure 3.14 is for those ITPs and time periods used in this analysis, and does not represent all profiles currently available for all ITPs.

As ITPs are typically deployed during late summer to early fall, in the thickest ice floes available, there is a slight spatial bias in the month of year profiles were taken (Figure 3.15a), with the average latitude for profiles slightly further south in the Canada Basin from April to August. However, the variability in this average latitude of measurement is very high, and the associated spatial pattern in month of year of measurement (Figure 3.15b) does not match that for the near-inertial wave amplitude estimates (Figure 3.3b). This slight temporal measurement bias in ITP sampling may partially explain the latitudinal trend in wave amplitude, though largely by its connection to sea-ice concentration and speed, which are considered separately. Note that numerous measurements were made during the summer of 2013 in the southeast corner of the Basin, in a region south of the M2 critical latitude and

ITP	Years Sampled	Months of Year Sampled														
		Aug	Sep	Oct	Nov	Dec	Jan	Feb	Mar	Apr	May	Jun	Jul	Aug	Sep	Oct
1	2005-2006	■	■	■	■	■	■	■	■	■	■	■	■	▒	▒	▒
	2006-2007	▒	▒	▒	■	■	■									
3	2005-2006	■	■	■	■	■	■	■	■	■	■	■	■	■	■	
4	2006-2007		■	■	■	■	■	■	■	■	■	■	■	■		
5	2006-2007		■	■	■	■	■	■	■	■	■	■	■	■	■	
6	2006-2007		■	■	■	■	■	■	■	■	■	■	■	▒	▒	▒
	2007-2008	▒	▒	▒	■	■	■	■	■	■	■	■	■			
8	2007-2008	■	■	■	■	■	■	■	■	■	■	■	■	■	■	■
11	2007-2008		■	■	■	■	■	■	■	■	■	■	■	▒	▒	▒
	2008-2009	▒	▒	▒	■	■	■	■	■	■	■	■	■	■	■	■
13	2007-2008	■	■	■	■	■	■	■	■	■	■	■	■	■		
18	2007-2008	■	■	■	■	■	■	■	■	■	■	■	■	■	■	■
33	2009-2010			■	■	■	■	■	■	■	■	■	■	▒	▒	▒
	2010-2011	▒	▒	▒	■	■	■									
34	2009-2010			■	■	■	■	■	■							
35	2009-2010			■	■	■	■	■	■							
41	2010-2011			■	■	■	■	■	■	■	■	■	■	▒	▒	▒
	2011-2012	▒	▒	▒	■	■	■	■	■	■	■	■	■			
42	2010-2011			■	■	■	■	■	■	■						
52	2011-2012	■	■	■	■											
53	2011-2012	■	■	■	■	■	■	■	■	■	■	■	■	■		
55	2011-2012	■	■	■	■	■										
62	2012-2013			■	■	■	■	■	■	■	■	■	■	■		
64	2012-2013	■	■	■	■	■	■	■	■	■	■	■	■	■		
65	2012-2013	■	■	■	■	■	■	■	■	■	■	■				
68	2013-2014	■	■	■	■	■	■	■	■	■	■					
69	2013-2014	■	■	■	■	■	■	■	■							
70	2013-2014	■	■	■	■	■	■	■	■	■	■	■	■			
77	2013-2014								■	■	■	■	■	■	■	■
78	2013-2014								■	■	■	■	■			
79	2013-2014								■	■	■	■	■	■	■	
80	2014-2015	■	■	■												

Figure 3.14: Ice-Tethered Profilers used for the analysis herein, listed by ITP number, years sampled, and months for which data was available for the analysis (shaded grey). As ITPs are typically deployed in late summer or early fall, the months of August through October are repeated. For ITPs which profiled for longer than 15 months, an additional row lists the second year, with repeated months shaded a darker grey. Eg: For ITP1, data from Aug 2005 to Jan 2007 was used. For ITP 8, data from Aug 2007 to Oct 2008 was used. For ITP 79, data from Mar 2014 to Sep 2014 was used.

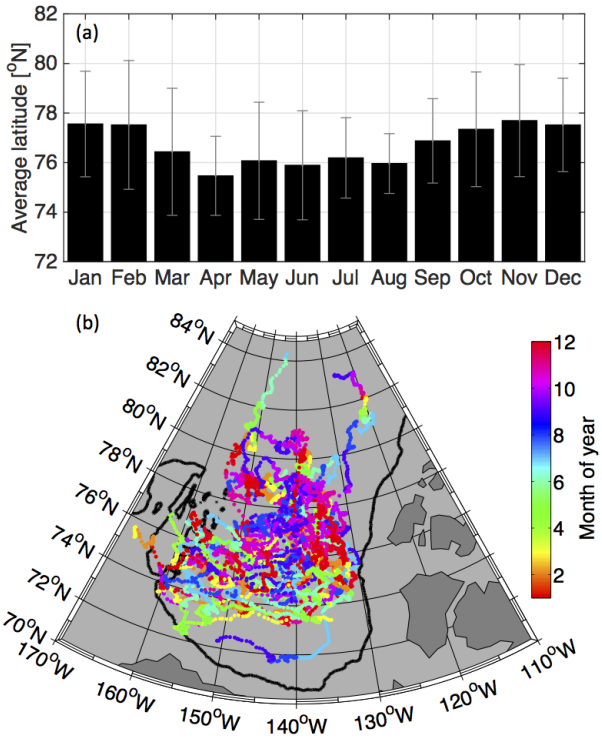

Figure 3.15: (a) Average latitude of ITP profiles by month of year. Grey error bars show one standard deviation around the mean. (b) Spatial map for month-of-year ITP profiles were measured, plotted along the ITP tracks from 2005 to 2014.

therefore permitting generation of a semi-diurnal internal tide. A temporal/spatial bias for that time period is discussed further in the text.

3.9 Acknowledgments

We acknowledge the support of the Office of Naval Research (grant N00014-11-1-0454) for this study. We gratefully acknowledge the Ice-Tethered Profiler Program and the Beaufort Gyre Exploration Program based at the Woods Hole Oceanographic Institution (in collaboration with researchers from Fisheries and Oceans Canada at the Institute of Ocean Sciences) for deploying and maintaining the ITPs (*http://www.whoi.edu/itp*) and (*http://www.whoi.edu/beaufortgyre*). We thank J. Toole and K. Martini for useful discussions.

3.10 Appendix: Unpublished material

3.10.1 Spatial pattern in wind and sea ice

Spatial patterns in wind and sea-ice speed and ice concentration following the ITP tracks (Figure 3.16) show little agreement with the spatial distribution of depth-averaged near-inertial internal wave amplitudes (Figure 3.3b). Neither wind nor sub-inertial sea-ice drift speed show any clear spatial pattern in either the latitudinal or longitudinal directions. The patterns in clockwise inertial ice speed are roughly opposite to those in percent ice concentration, with larger inertial oscillations when ice cover is low and ice floes are mobile, as discussed above. Neither has the linear increase to the south across all longitudes visible in the near-inertial wave amplitude data.

3.10.2 Scatterplots

Individual estimates of wave amplitude are compared to wind speed, sub-inertial ice drift speed, and wind factor (Figure 3.17). These fields are smoothed with a 4-day running mean to match the 4-day timescale associated with the waves. The high variance in wave amplitude is immediately evident from the scatter. Note that the average uncertainty associated with

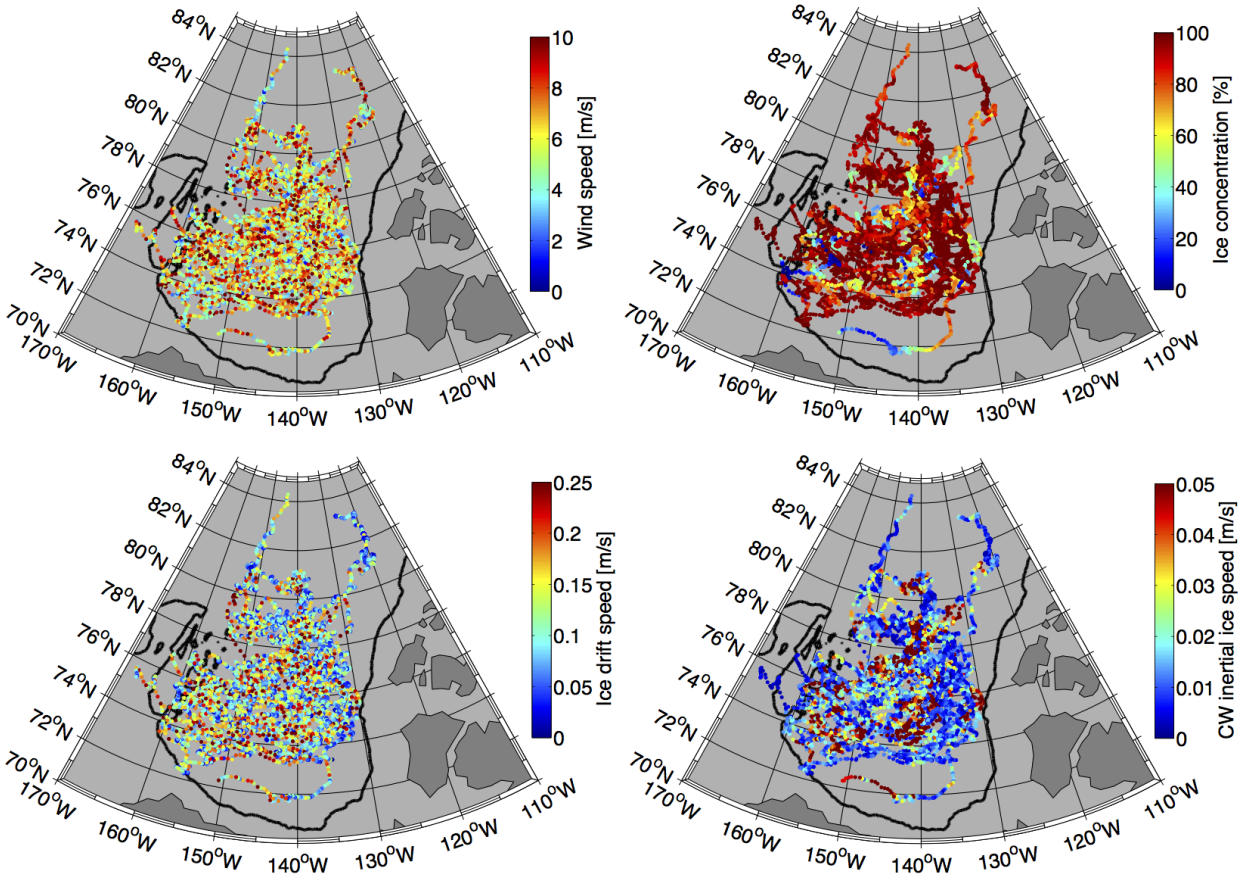

Figure 3.16: Spatial patterns following the ITP tracks for (a) wind speed, (b) percent sea-ice concentration, (c) sub-inertial sea-ice drift speed, and (d) clockwise inertial sea-ice speed.

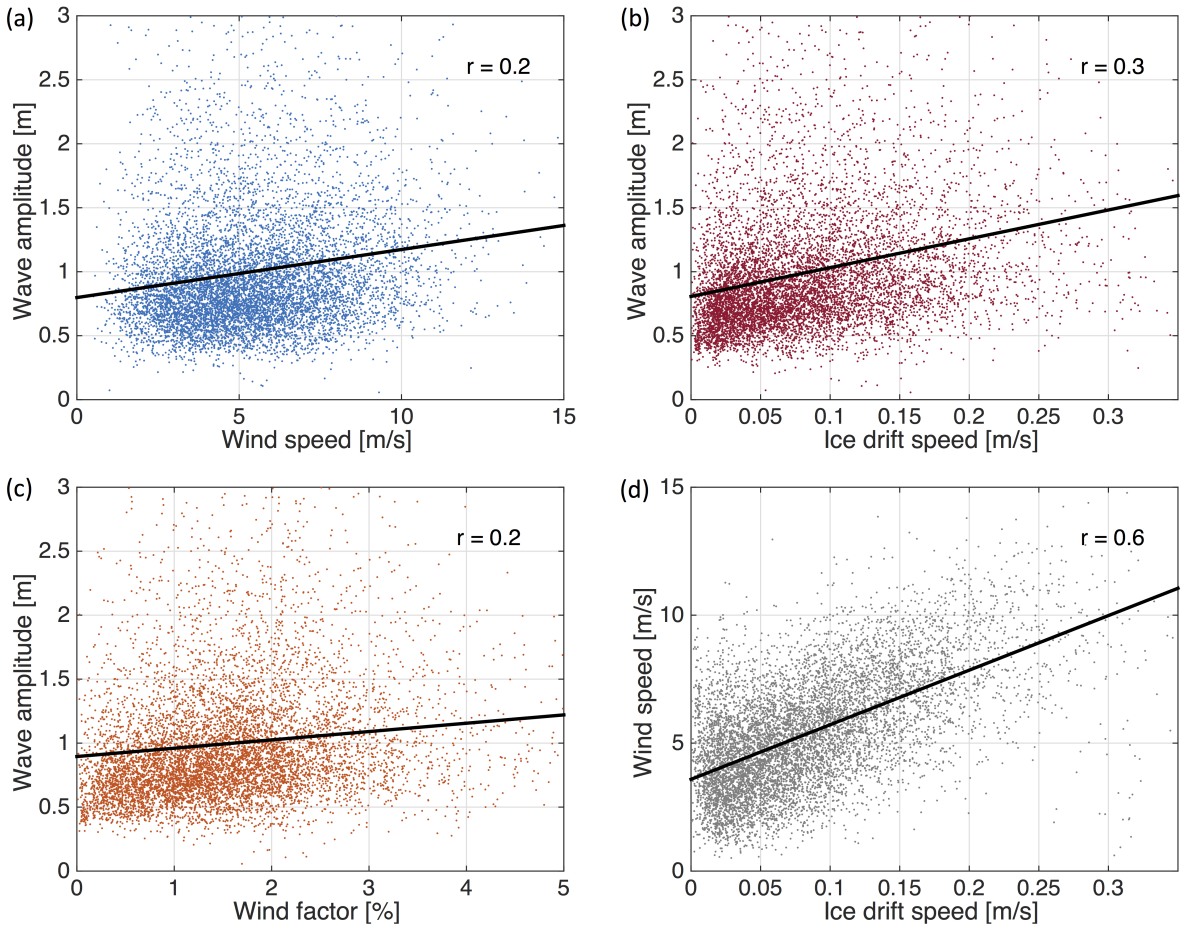

Figure 3.17: Scatterplots of all data from 2005 to 2014 for (a) wave amplitude estimates vs. 4-day running mean of wind speed, (b) wave amplitude vs. 4-day running mean of sub-inertial ice drift speed, (c) wave amplitude vs. 4-day running mean of wind factor, and (d) wind speed vs. ice drift speed. Correlation coefficients and linear fits to the data are shown. 4-day running mean is used to match degrees of freedom with wave amplitude estimates. Colours correspond to those in Figure 3.13.

individual amplitude estimates for the wave field can be up to ±1m. The wave amplitude time series has a low but significant correlation with both wind speed ($r = 0.2$, Figure 3.17a), wind factor ($r = 0.2$, Figure 3.17c), and ice drift speed ($r = 0.3$, Figure 3.17b). Wind factor does not well explain variations in the near-inertial internal wave field on short timescales.

Neither sea-ice concentration nor CW inertial ice speed are significantly correlated with the near-inertial wave field. Wind speed and sea-ice drift speed are correlated at $r = 0.6$ (Figure 3.17d). The motion of the sea ice is closely tied to changes in the wind forcing on short timescales, despite the lack of agreement on seasonal and interannual timescales.

Chapter 4

INTERNAL WAVE PROPAGATION AND STABILITY IN THE WESTERN ARCTIC

Note: Sections of this chapter were part of collaborative work with Sasan Ghaemsaidi and Thomas Peacock at the Environmental Dynamics Lab at MIT. I am second author on a manuscript based on this collaboration that is currently in revision in the Cambridge Journal of Fluid Mechanics as of August 2015. Subject to Cambridge Journals Copyright as of date of publication.
Citation: Sasan J. Ghaemsaidi, Hayley V. Dosser, Luc Rainville, Thomas Peacock: The impact of multiple layering on internal wave transmission, J. Fluid Mech.

4.1 Introduction

Internal wave energy levels in the Arctic Ocean were determined observationally as early as the 1980s and 1990s. Observations from ice camps supported the idea of a quiescent Arctic Ocean with limited vertical mixing, and an energy level an order of magnitude below that at lower latitudes (e.g.: the Arctic Internal Waves Experiment, AIWEX Spring 1985 - Levine et al. (1985), 1987; D'Asaro and Morehead (1991); Merrifield and Pinkel (1996), and the Surface Heat Budget of the Arctic experiment, SHEBA 1997-1998 - Pinkel (2005)).

Recent observations indicate that Arctic internal waves are more energetic during ice-free or ice-forming conditions (Rainville and Woodgate, 2009; Cole et al., 2014; Martini et al., 2014). No trend in average diffusivity over the last 30 years was found in the Western Arctic (Guthrie et al., 2013), suggesting that the internal wave field remains relatively low energy on average. However, the generation of unusually large wind forced near-inertial waves is becoming more common as sea ice declines and multiyear ice is replaced by first-year ice in

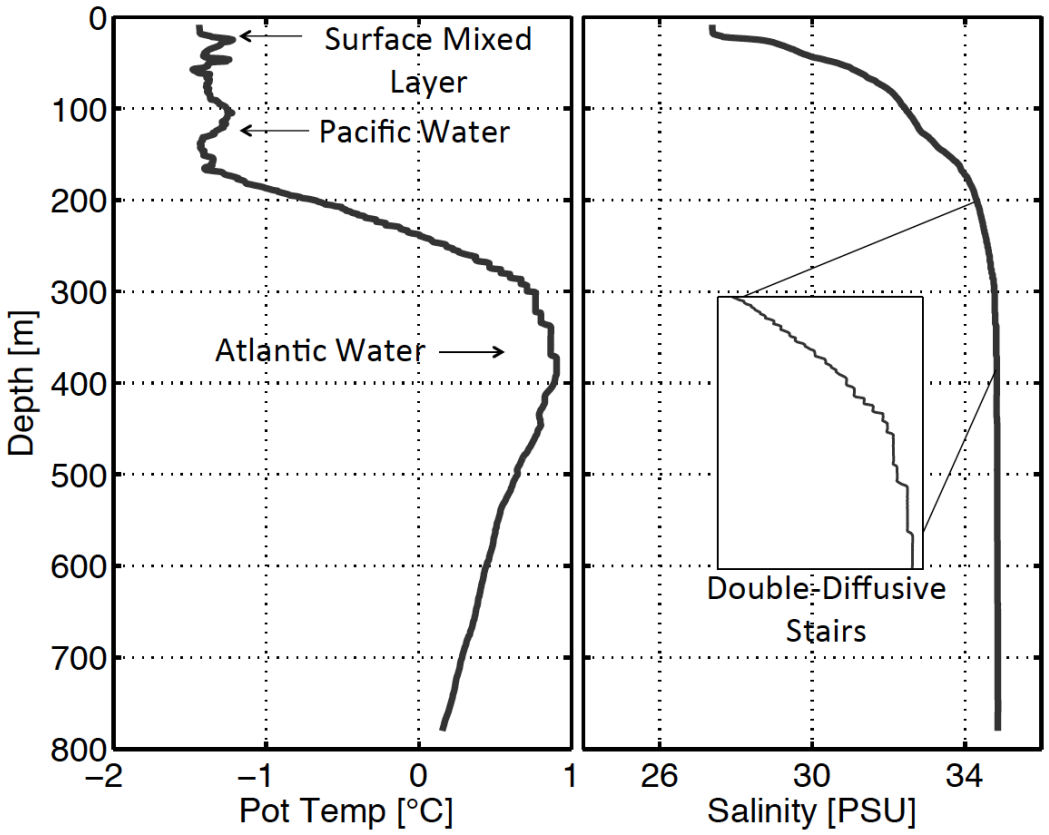

Figure 4.1: Potential temperature and salinity profiles from an Ice-Tethered Profiler in the Canada Basin, showing details of the typical stratification in the region from the surface mixed layer to ∼800m depth. Water masses are indicated. The inset shows details of the double-diffusive staircase found above the Atlantic Water temperature maximum.

the Canada Basin (Chapter 3: Dosser and Rainville (2015)). Depending on the details of the propagation of high energy internal waves through the stratification in the western Arctic Ocean, internal wave instability and breaking may become more common.

The internal wave field in the Arctic Ocean is a combination of downward propagating wind generated near-inertial waves and upward propagating waves from either a topographically generated internal tide (Halle and Pinkel, 2003) or surface generated internal waves that have reflected off the ocean floor (Pinkel, 2005). Most of the energy in the internal wave spectrum is found in the near-inertial band (Chapter 2: Dosser et al. (2014) - Appendix),

$\omega \approx f$, where the Coriolis period $2\pi/f$ varies from just over 12 hours in the northern Canada Basin at 85^oN to about 12.7 hours in the far south of the Basin at 70^oN.

A typical stratification profile in the Canada Basin (Figure 4.1) is dominated by salinity variations. A seasonally varying mixed layer roughly 15-25m deep on average (Toole et al., 2010) overlays the often-present near-surface temperature maximum (Jackson et al., 2010; Steele et al., 2011), and a local temperature maximum associated with Pacific Summer Water. A strong halocline and thermocline are associated with the Atlantic Water layer, which is both warmer and saltier than the overlying Pacific Water. Below the Atlantic Water temperature maximum, potential density is nearly constant with depth. Heat within the Atlantic Water layer is sufficient to completely melt the sea ice, but is trapped at depth due to the strength of the halocline, isolating it from the ice in the absence of vertical mixing (Turner, 2010). The monotonically increasing temperature and salinity within the Atlantic Water layer and low levels of turbulent mixing have led to the formation of a 'double-diffusive staircase' stratification feature above the temperature maximum.

The double-diffusive staircase in the Arctic Ocean (Figure 4.2) is formed by diffusive convective instability, rather than by salt fingers as is common at lower latitudes. The salinity, and therefore density, stratification is stable; the energy for convection is contained in the unstable thermal stratification. A parcel of warm, salty water displaced into cooler, fresher water will cool due to the rapid diffusion of heat relative to salt. The parcel will then be denser than the surrounding fluid, sink and overshoot its original depth, resulting in an oscillation. These instabilities create overturning convective cells, resulting eventually in a series of well-mixed layers or 'steps' of constant density with thickness from $\mathcal{O}$(1m) or less to $\mathcal{O}$(10m) or more, separated by thin interfaces, $\mathcal{O}$(10cm), with strong salinity and temperature gradients (Turner, 1968).

Such staircases have been widely observed in the Western Arctic (Padman and Dillon, 1987, 1988, 1989; Timmermans et al., 2008a). Vertical heat flux through a double-diffusive staircase is estimated using the laboratory derived '4/3 flux laws', based on the gradient of potential temperature across the stratified interfaces (Marmorino and Caldwell, 1976; Kelley,

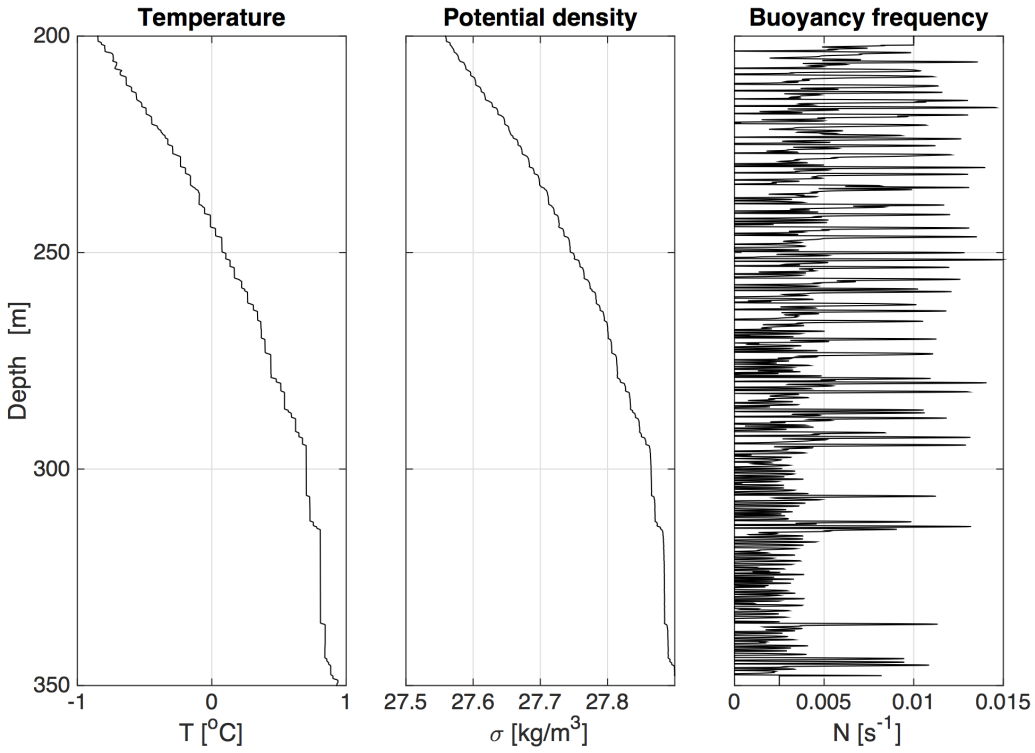

Figure 4.2: Potential temperature, potential density, and buoyancy frequency for the double-diffusive staircase, from a high-resolution CTD profile in the Canada Basin.

1984). Heat fluxes from the staircase in the Canada Basin are quite low, originally found to be $0.05 - 0.2\mathrm{W/m^2}$ (Padman and Dillon, 1987), based on the 4/3 flux law of Marmorino and Caldwell (1976), and more recently $0.22 \pm 0.10\mathrm{W/m^2}$ (Timmermans et al., 2008a), based on the 4/3 flux laws determined by both Marmorino and Caldwell (1976) and Kelley (1984). These heat fluxes are an order of magnitude smaller than the estimated heat flux from the mixed layer to the sea ice, and two orders of magnitude below the Basin-average heat loss from the Atlantic Water, making them relatively unimportant to sea-ice melt (Turner, 2010).

The double-diffusive staircase in the Canada Basin is coherent over hundreds of kilometres across the Basin (Rudels et al., 2009; Timmermans et al., 2008a), with individual layers persisting over several years. A double-diffusive staircase can only persist if up-gradient double-diffusion of heat is larger than down-gradient turbulent diffusion due to mixing. The coherence of the staircase in recent years suggests a lack of persistent turbulent mixing, with the exception of the Basin peripheries, in which the staircase structure is eroded (Timmermans et al., 2008a). The impact of the double-diffusive staircase on internal wave propagation and stability is an open question, as is the effect of an increasingly but intermittently energetic internal wave field on the staircase stratification.

Most longterm observational platforms in the Arctic Ocean, including Ice-Tethered Profilers, lack the resolution to determine how individual internal waves evolve as they propagate vertically. Internal waves have vertical scales which may be smaller, larger, or comparable to vertical variations in the double-diffusive staircase stratification. Pinkel (2008) observed near-inertial waves in the Western Arctic that were energetic over a broad band of vertical wavelengths, between 10m (the smallest resolvable scale) and several hundred meters. Cole et al. (2014) found that the shear spectrum for internal waves in the Canada Basin had a peak between 10-50m vertical wavelength. A typical mixed layer in the double-diffusive staircase can be on the order of 1m thick in the upper staircase, to tens of meters thick in the lower staircase, with stratified interfaces on the order of 10cm thick (Timmermans et al., 2008a). Few existing datasets capture the details of internal wave propagation through the staircase, or possible causes of wave instability associated with wave-stratification interac-

tions. In order to progress further, a combination of theory and numerical simulations is necessary.

Eckart (1961) considered internal waves in stratified fluid in which two strongly stratified layers were separated by a weakly stratified layer, an example being the seasonal and main ocean thermoclines. Ray theory (also called WKB-theory, e.g. Lighthill (1978)) treats waves as particles and incorrectly predicts total reflection for waves whose wavelength is short compared to vertical variations in the stratification. Likewise, total transmission of wave energy may be incorrectly assumed for waves whose vertical wavelength is long compared to variations in the stratification.

Treating the situation as an eigenvalue problem, Eckart (1961) found resonant energy transmission back and forth across the weakly stratified layer for vertical wave modes in the strongly stratified layers whose frequencies and vertical wavenumbers matched. 'Eckart resonance' in the atmosphere was investigated by Fritts and Yuan (1989) for internal waves propagating between the stratosphere and the ionosphere.

In the ocean, Mysak (1978) provides an overview of internal and near-inertial wave propagation through variable stratification with realistic vertical variations, including work by Mysak and Howe (1976), who derived a formula for reflected and transmitted energy of an upward propagating internal wave of specified frequency and vertical wavenumber, scattering from a layer of random small-scale fluctuations in the stratification. They found significant wave reflection if the layer was very thick compared to the scale of the waves, or if the variance in the vertical wavenumber spectrum for the stratification was high. D'Asaro (1982) demonstrated observationally and using a slab model that near-inertial waves encountering the turbulent benthic boundary layer are partially absorbed and significantly reflected from the layer, despite the vertical width of the layer potentially being thin compared to the vertical scale of the incident waves.

Sutherland and Yewchuk (2004) derived analytic solutions and performed laboratory experiments for internal waves encountering a single mixed layer in a constant stratification profile. They found that, contrary to the predictions of ray theory for complete wave reflec-

tion, internal waves whose vertical scale is comparable to or smaller than the mixed layer are still able to partially or completely 'tunnel' through, transmitting some wave energy, depending on their vertical wavenumber and frequency.

This work was extended to numerical solutions for internal waves in vertically varying background stratification and shear by Nault and Sutherland (2007), and to internal wave beams by Mathur and Peacock (2009), who found significant modification of the waves due to variations in the stratification. The evolution of surface forced internal waves in realistic ocean stratifications with complex vertical structure was modelled numerically by Ghaemsaidi et al. (2015a), and extended to layered stratifications similar to an Arctic double-diffusive staircase by Ghaemsaidi, Dosser, Rainville, and Peacock (2015).

The current work builds on these earlier studies, with a focus on exploring the parameter regime most pertinent to internal waves in the Western Arctic Ocean. In this research, an analytic solution is derived for two mixed layers separated by a stratified interface, and used to further validate the numerical solution technique for use with layered stratifications. Numerical solutions for successively more realistic idealized layered stratifications are determined, and the physics underlying their effect on the internal wave field is discussed.

Finally, the impact of the unusual double-diffusive staircase stratification ubiquitous to the Arctic Ocean on internal wave propagation, vertical energy flux, and wave stability is determined using observed stratification profiles. The vertical displacement amplitude distribution for near-inertial waves determined from the Ice-Tethered Profiler dataset is used to provide realistic values for internal waves in the current Arctic climate.

The key questions are:
I. Does the double-diffusive staircase affect Arctic internal wave propagation and stability?
II. Can unstable internal waves affect the stratification through overturning and mixing?
III. Do internal waves contribute significantly to mixing in the Arctic Ocean?

4.2 Theory

For the case of a rotating Boussinesq fluid with no background flow, small amplitude internal waves are described by the following governing equations:

$$\frac{\partial u}{\partial t} = fv - \frac{1}{\rho_0}p_x \tag{4.1}$$

$$\frac{\partial v}{\partial t} = -fu \tag{4.2}$$

$$\frac{\partial w}{\partial t} = -\frac{g}{\rho_0}\rho - \frac{1}{\rho_0}p_z \tag{4.3}$$

$$\frac{\partial \rho}{\partial t} = -w\frac{d\bar{\rho}}{dz} \tag{4.4}$$

$$\frac{\partial u}{\partial x} + \frac{\partial w}{\partial z} = 0 \tag{4.5}$$

where $\vec{u} = (u, v, w)$ is the velocity associated with the waves, p and ρ are the perturbation pressure and density respectively, ρ_0 is a reference density, $\bar{\rho}(z)$ is the background density profile, f is the Coriolis parameter, and the simplifying assumption that the waves have no structure in the y-direction has been made, so that y-derivatives are zero.

The Taylor-Goldstein equation describes the vertical structure of an internal wave propagating through an arbitrary density stratification. It was independently derived by G. I. Taylor and S. Goldstein in 1931, replicated here with the inclusion of rotation. Eliminating pressure by taking the curl of the momentum equations gives:

$$\frac{\partial^2 u}{\partial t \partial z} - \frac{\partial^2 w}{\partial t \partial x} = f\frac{\partial v}{\partial z} + \frac{g}{\rho_0}\frac{\partial \rho}{\partial x}. \tag{4.6}$$

Equations (2), (4), and (5) are used to eliminate v, ρ, and u respectively, leaving an equation solely in terms of the vertical velocity w:

$$\frac{\partial^2}{\partial t^2}\nabla^2 w + N^2\frac{\partial^2 w}{\partial x^2} + f^2\frac{\partial^2 w}{\partial z^2} = 0. \tag{4.7}$$

Here $N^2(z) = -(g/\rho_0)d\bar{\rho}/dz$ is the vertically varying background buoyancy frequency profile.

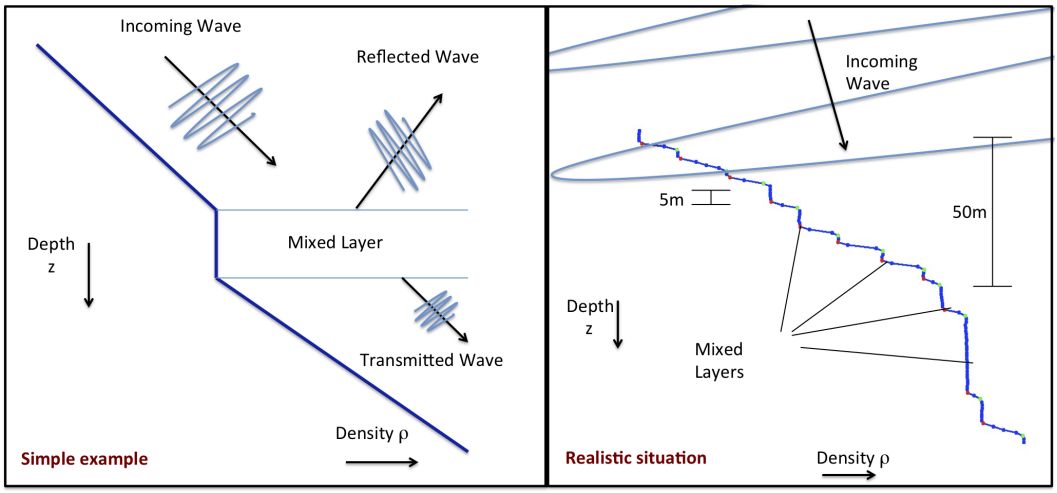

Figure 4.3: Left: Cartoon illustrating an incoming 'incident' internal wave encountering a single mixed layer, partially reflecting and partially transmitted. The internal wave decays exponentially in amplitude within the mixed layer. Right: Cartoon illustrating an internal encountering a series of mixed layers in a double-diffusive staircase stratification. This wave will also partially reflect and partially transmit, depending on the vertical scale of the wave relative to the thickness of the mixed layers and stratified interfaces within the staircase.

In a depth-dependent stratification, the z-direction structure of the wave solution may not be oscillatory for all depths, so that any basic state field $a(x, z, t)$ is given by:

$$a(x, z, t) = \tilde{a}(z) \exp \imath(kx - \omega t), \tag{4.8}$$

in which $\tilde{a}(z)$ is the unknown depth-dependent term, k is the horizontal wavenumber, ω is the wave frequency, and the actual measured field is taken to be the real part of (8).

Combining this with equation (4.7), and replacing the vertical velocity by the vertical displacement η associated with the wave ($w = \partial\eta/\partial t$) leads to the form of the Taylor-Goldstein equation used for this analysis:

$$\frac{d^2\tilde{\eta}}{dz^2} = -k^2 \frac{N^2 - \omega^2}{\omega^2 - f^2}\tilde{\eta}. \tag{4.9}$$

Solutions to this 1-D ordinary differential equation describe how the vertical displacement of an internal wave in an arbitrary stratification varies with depth.

For internal waves under the influence of rotation, the frequency for freely propagating waves is constrained to $f < \omega < N$. In regions where the stratification is approximately constant ($N(z) \approx N_0$), the z-structure of the wave is given by $\tilde{\eta}(z) = A_\eta \exp \imath mz$, in which A_η is the vertical displacement wave amplitude and m is the vertical wavenumber, giving the standard dispersion relation:

$$\omega^2 = \frac{k^2 N_0^2 + m^2 f^2}{k^2 + m^2}. \tag{4.10}$$

Other fields of interest can be calculated from the governing equations:

$$\tilde{w} = -\imath\omega\tilde{\eta} \tag{4.11}$$

$$\tilde{u} = (\omega/k)\partial\tilde{\eta}/\partial z \tag{4.12}$$

$$\tilde{v} = -\imath(f/k)\partial\tilde{\eta}/\partial z \tag{4.13}$$

$$\tilde{\rho} = (\rho_0/g)N^2\tilde{\eta} \tag{4.14}$$

$$\tilde{p} = \rho_0(N^2 - \omega^2)\int \tilde{\eta} dz. \tag{4.15}$$

Here $\vec{u} = (u, v, w)$ are the horizontal and vertical velocities, ρ is the density, and p is the pressure associated with the internal wave.

Vertical energy flux is used to characterize wave transmission through the double-diffusive staircase, and is calculated from $F_z = \langle wp \rangle$, where $\langle\rangle$ denotes a horizontal average over one wavelength and a temporal average over one wave period. Using (11) and (15), and assuming $N \simeq N_0$, the vertical energy flux above and below the staircase is:

$$F_z = \rho_0(\omega/m)(N_0^2 - \omega^2)A_\eta^2 \exp 2\imath mz. \tag{4.16}$$

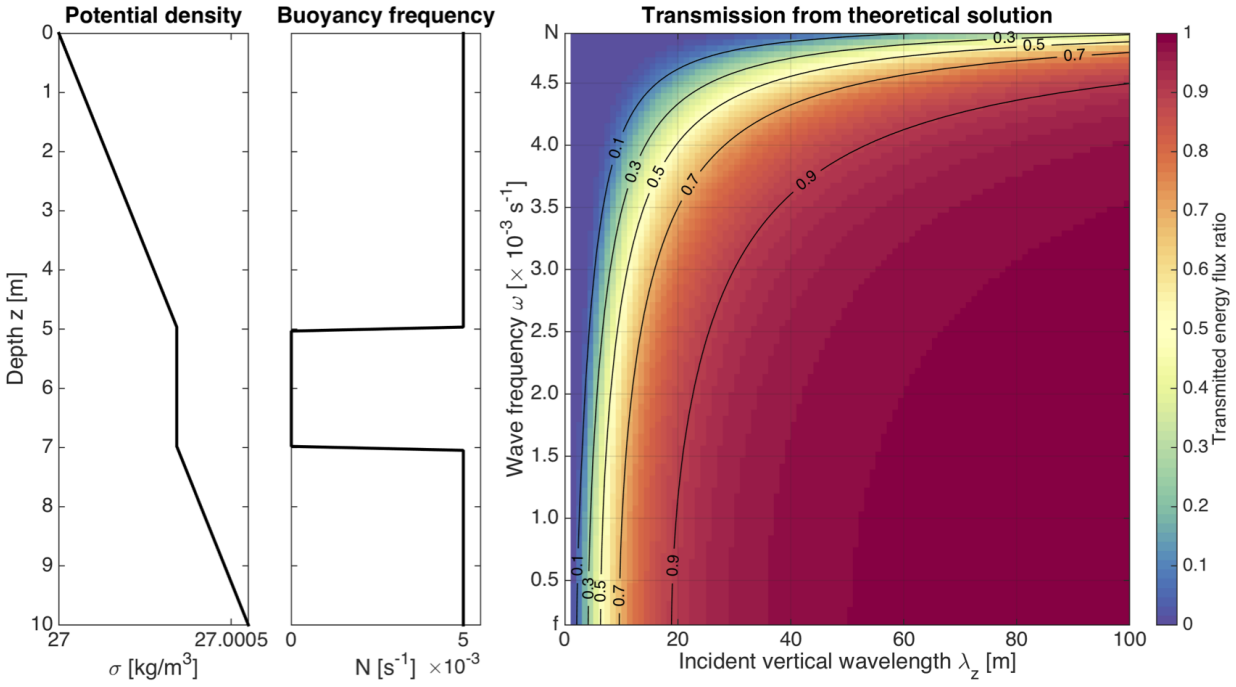

Figure 4.4: Transmitted vertical energy flux ratio calculated for the density profile in the left panel, with the associated buoyancy frequency profile for a single mixed layer or 'step' with thickness $L = 2$m. Here f is the Coriolis frequency (calculated at 75^{o}N) and $N \equiv N_0 = 0.005$rad s^{-1} is the constant background buoyancy frequency.

4.3 Analytic solutions

Analytic solutions of the Taylor-Goldstein equation can be determined for internal waves propagating through simple layered stratifications, such as the constant stratification profile with a single mixed layer examined by Sutherland and Yewchuk (2004). In this scenario, an incident, oscillatory internal wave encounters the mixed layer, and is partially reflected. Within the mixed layer, the wave is evanescent - that is, its amplitude decays exponentially with depth. On the other side of the mixed layer, the transmitted wave is once again oscillatory (Figure 4.3).

Boundary conditions above and below the mixed layer require that the vertical velocity and pressure be continuous, which is equivalent to requiring that the streamfunction be continuous and differentiable in a fluid with zero mean flow. For a mixed layer of thickness L, they found the transmission coefficient for a 2-D, Boussinesq internal wave in a non-rotating fluid (their equation 2.3, rearranged):

$$T = \left[1 + \frac{N_0^2/\omega^2}{4(N_0^2/\omega^2 - 1)} \sinh^2(Lm_0)\right]^{-1}, \tag{4.17}$$

in which $m_0 \equiv k$ is the vertical 'wavenumber' in the mixed layer. The transmission coefficient is defined as the fraction of transmitted to incident vertical energy flux F_z for the waves.

This equation predicts complete transmission for waves whose vertical wavelength λ_z is large relative to L (Figure 4.4). However, partial transmission also occurs for waves with $\lambda_z \leq L$. Internal waves are evanescent within the mixed layer, so that this transmission indicates wave 'tunnelling' between the two stratified regions, which Sutherland and Yewchuk (2004) describe as analogous to quantum mechanical tunnelling across a potential barrier.

Tunnelling can occur whenever an internal wave encounters a layer within the stratification for which $N < \omega$. In the double-diffusive staircase, the constant density 'steps' are such layers, for which $N = 0$. Ray theory predicts wave reflection, however, the actual wave solution within the weakly stratified or mixed layer gives an exponential decrease in wave

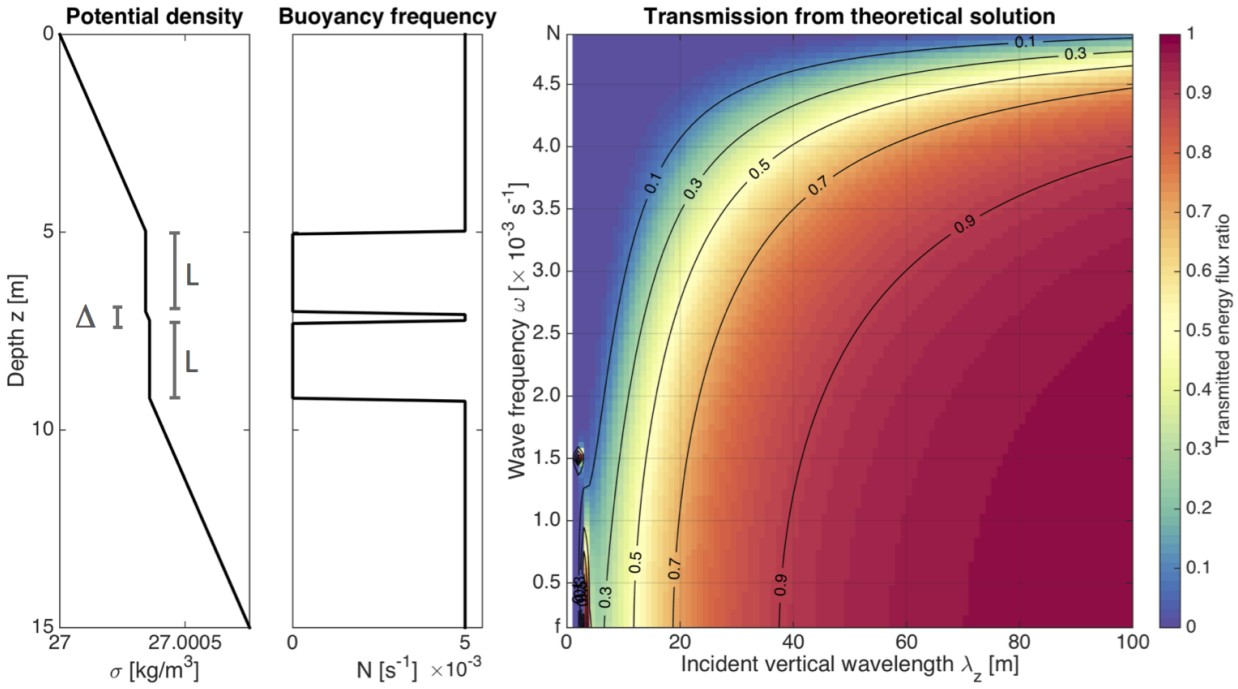

Figure 4.5: Transmitted energy flux ratio calculated for the density profile in the left panel, with the associated buoyancy frequency profile for two mixed layers or 'steps' with $L = 2$m separated by a stratified interface with $\Delta = 20$cm. The first mixed layer begins at $h = 5$m.

amplitude with depth - the wave is evanescent. If the layer is sufficiently thin relative to the exponential decay scale of the wave, energy is transferred through, producing a propagating internal wave on the other side.

For the single layer case considered by Sutherland and Yewchuk (2004), transmission is predicted to be small for internal waves whose frequency ω is nearly equal to N_0. The cause of this is not well documented in the literature, but the likely explanation is as follows: The angle of incidence of such a wave with the mixed layer will be nearly zero, the wave will approach and reflect almost vertically. The phase of the reflected wave will be nearly opposite that of the incident wave (Ghaemsaidi et al., 2015a), which is not the case for $\omega << N_0$. Thus the reflected wave will be almost totally out of phase with the incident wave, leading to destructive interference and reduced transmission of wave energy.

As a step toward understanding propagation through the double-diffusive staircase stratification (Figure 4.3), the equation for transmission through a two layer stratification in a rotating fluid, with a stratified interface separating two mixed layers, is derived as part of the current analysis. The stratification profile (e.g. Figure 4.5) is:

$$N(z) = \begin{cases} 0, & \text{for } h < z < (h + L) \\ 0, & \text{for } (h + L + \Delta) < z < (h + 2L + \Delta) \\ N_0, & \text{otherwise} \end{cases} \tag{4.18}$$

where h is the depth of the top of the first mixed layer and $N(z)$ is shown in Figure 4.5.

The Taylor-Goldstein equation (4.9) specifies the vertical structure of the waves in each region:

$$\tilde{\eta}(z) = \begin{cases} A_I e^{-\imath m z} + A_R e^{\imath m z}, & \text{for } z < h \\ B_1 e^{-m_0 z} + B_2 e^{m_0 z}, & \text{for } h < z < (h + L) \\ A_{I\Delta} e^{-\imath m z} + A_{R\Delta} e^{\imath m z}, & \text{for } (h + L) < z < (h + L + \Delta) \\ B_3 e^{-m_0 z} + B_4 e^{m_0 z}, & \text{for } (h + L + \Delta) < z < (h + 2L + \Delta) \\ A_T e^{-\imath m z}, & \text{for } z > (h + 2L + \Delta). \end{cases} \tag{4.19}$$

Here A_I, A_R, and A_T are the incident, reflected, and transmitted vertical displacement wave amplitudes respectively, $A_{I\Delta}$ and $A_{R\Delta}$ are the reflected and transmitted wave amplitudes within the stratified interface of thickness Δ, and B_1 through B_4 are the evanescent wave amplitudes within the mixed layers of thickness L. The vertical wavenumber is denoted by m where the wave is oscillatory and by m_0 where it is evanescent. It is defined as positive, so that an incident wave propagates downwards.

These 5 equations are solved for A_T by assuming a continuous background density profile, which imposes the requirement for continuity of the vertical displacement $\tilde{\eta}$ and of its

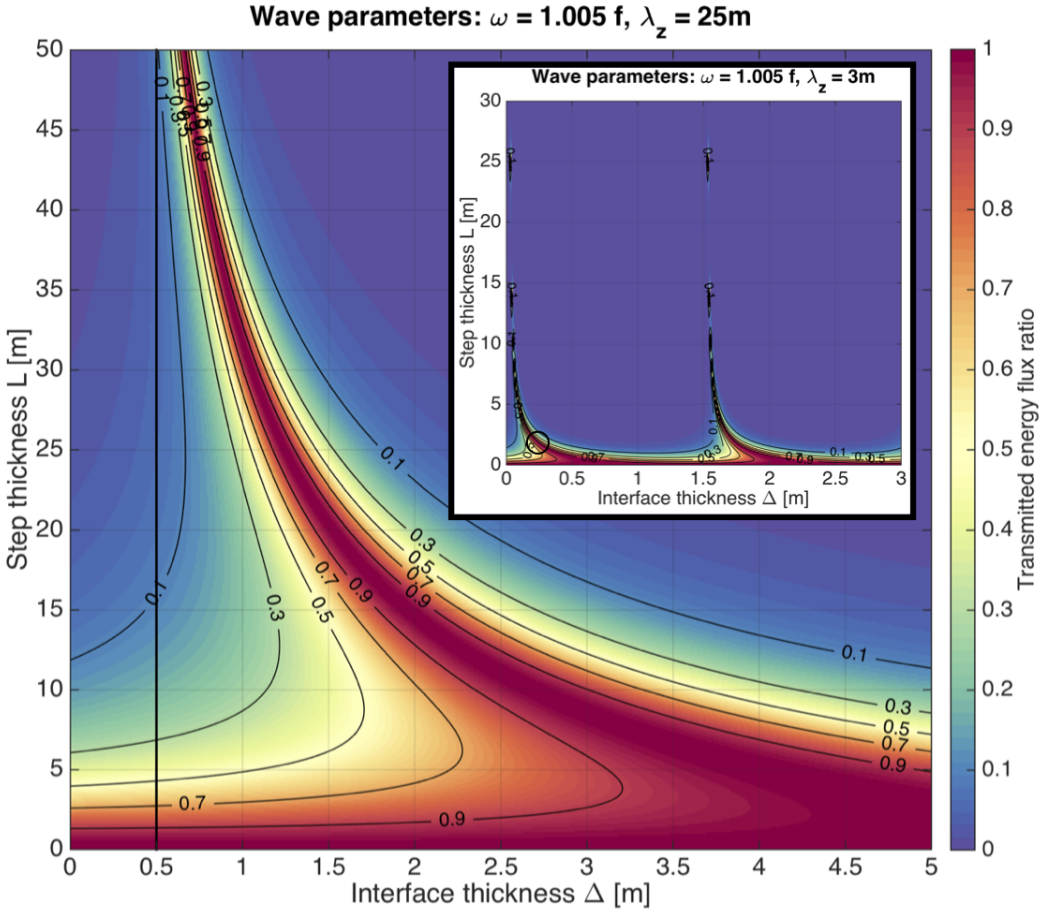

Figure 4.6: Transmission for different step and interface thicknesses for a wave of given λ_z and ω crossing the two step stratification shown in Figure 4.5. The vertical black line provides a rough upper limit for typical values of Δ for Arctic double-diffusive staircases. Inset shows transmission for smaller λ_z. Black circle shows resonant transmission for L, Δ matching the stratification in Figure 4.5.

derivative at the top and bottom of each mixed region. After some algebra, the solution is:

$$T = \frac{|A_T|^2}{|A_I|^2} = \left| (1 - e^{-2\imath m\Delta}) \left(\frac{1}{4} + \frac{1}{8} \left(\frac{m_0^2}{m^2} + \frac{m^2}{m_0^2} \right) (1 - \cosh 2m_0 L) \right) + \frac{1}{4}(3 + e^{-2\imath m\Delta}) \cosh(2m_0 L) - \frac{1}{2}\imath \left(\frac{m_0}{m} - \frac{m}{m_0} \right) \sinh 2m_0 L \right|^{-2}. \tag{4.20}$$

This collapses to the solution of Sutherland and Yewchuk (2004) in the limit $\Delta = 0$, with mixed layer thickness $2L$, and noting $m^2/m_0^2 = N_0^2/\omega^2 - 1$ and $m_0 \equiv k$ in non-rotating fluid.

Equation (4.20) indicates that internal wave transmission through a layered stratification is sensitive to the incident vertical wavenumber m, the wave frequency ω and background buoyancy frequency N_0 which determine the wavenumber in the mixed layers m_0, and the thickness of both mixed layers L and stratified interface Δ. Rotation enters the equation only by limiting the allowed values of ω for the incident wave. The specific parameters of interest are $m\Delta$, which relates the incident wavelength $\lambda_z = 2\pi/m$ to the stratified interface thickness, $m_0 L$, which relates the evanescent decay scale to the mixed layer thickness, and m/m_0, the ratio of the incident wavenumber to the 'wavenumber' in the mixed layer.

The result (Figure 4.5) is similar to the single mixed layer case (Figure 4.4), with slightly reduced transmission overall, and a sharp peak in transmission at low frequencies, which occurs for $\lambda_z \simeq 3$m in the example shown $\Delta = 20$cm and $L = 2$m (corresponding to $m \simeq 2$rad m^{-1} and $m_0 \simeq 0.06$rad m^{-1} for $\omega \simeq f$).

4.4 Resonant transmission

This is an example of what will be referred to as 'resonant transmission' - near complete transmission of incident wave energy occurring at certain combinations of incident vertical wavenumber and frequency (Figure 4.7). Resonant transmission is due to one of two mechanisms, depending on the details of the stratification:

- Resonance between the incident and reflected wave in the strongly stratified interface between mixed layers Ghaemsaidi et al. (2015a). Within the stratified layer, the in-

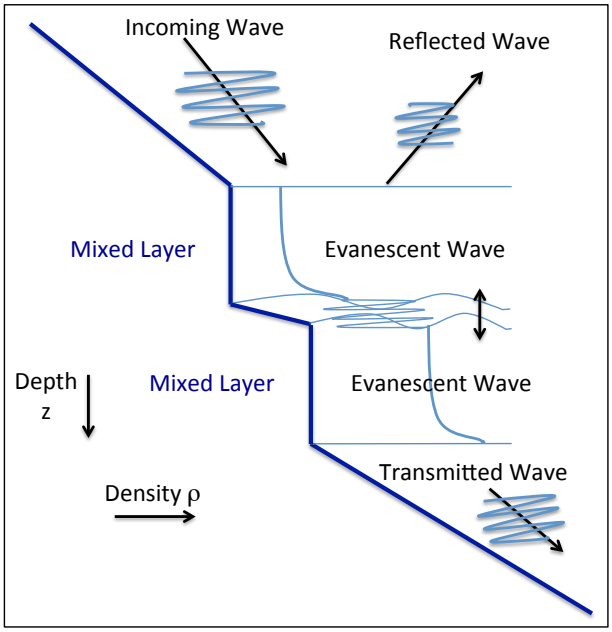

Figure 4.7: Cartoon showing an internal wave incident on a series of mixed layers separated by thin, stratified interfaces. The waves are oscillatory above and below the mixed layers and within the interfaces, and evanescent within the mixed layers. Resonance occurs for oscillations due to internal waves or interfacial waves in or on the stratified interfaces that are in phase and constructively interfere.

ternal wave will be oscillatory in the vertical. If the incident vertical wavenumber is such (relative to the thickness of the layer) that the reflected wave is mostly in phase with the incident wave, constructive interference occurs and resonantly enhances wave transmission through the mixed layer by amplifying the internal wave energy exiting the stratified layer.

Ghaemsaidi et al. (2015a) determined the transmitted wave amplitude: $A_T = A_I(1+r)$, where $r = (m - m_0)/(m + m_0)$ is the reflection coefficient, which is negative if the reflected wave switches phase. The condition for resonance is $m\Delta = (n-\frac{1}{2})\pi$ or $m\Delta = (n-1)\pi$, where n is an integer. This condition is satisfied when the stratified layer is exactly filled by (integer multiples of) quarter wavelength increments for the incident wave, $\Delta = n(\frac{1}{4}\lambda_z)$, allowing constructive interference upon reflection. Sutherland and Yewchuk (2004) also considered a case with wave transmission across a strongly stratified interface ('N^2-barrier') between two weakly stratified layers and found a series of transmission peaks which associated with resonance between the incident wave and wave modes trapped within the stratified interface.

- Resonance between the incident internal wave and interfacial waves along thin, strong stratified interfaces. An analytic solution is presented in Sutherland and Yewchuk (2004) for a discontinuous density profile in which a single mixed layer is bounded by two infinitely thin interfaces with infinitely large N. Resonance occurs if the vertical wavenumber and frequency of the incident wave are such that the incident internal wave linearly couples with the interfacial waves.

  Physically, the propagating internal wave impacts the stratified interface, forcing it to oscillate and generating an interfacial wave. The internal wave is evanescent within the mixed layer, but will generate a similar interfacial wave on the other side. If the interfacial waves are resonant with the incident wave, energy is efficiently transmitted through the mixed layer. In the simple case studied by Sutherland and Yewchuk (2004), this occurs when the frequency of the interfacial wave is equal to $\omega(m_0 L/2)^{1/2}$.

Varying the mixed layer thickness L and interface thickness Δ (Figure 4.6) when solving equation (4.20) strongly affects wave transmission. Thinner mixed layers or 'steps' (lower L) lead to more transmission, as does a thicker stratified interface (higher Δ). The resonant transmission peak, which occurs for certain combinations of L and Δ, is found to repeat (Figure 4.6 inset). For $L \gg \lambda_z$, the peaks occur at $\Delta = (n-1)\pi/m$, and for $L \ll \lambda_z$, the peaks occur at $\Delta = (n-\frac{1}{2})\pi/m$, with n an integer, in agreement with the conditions from Ghaemsaidi et al. (2015a) for resonant transmission between incident and reflected internal waves in a stratified layer.

The resonant peak shifts depending on the reflection within the interface. For $L \ll \lambda_z$, resonance occurs when a quarter wavelength of the incident wave fits approximately within the stratified interface (or three-quarters wavelength etc), so that the phase of the reflected wave causes constructive interference both within the interface and in the stratification above the relatively thin mixed layer. Significant transmission is possible for a fairly broad range of interfaces thicknesses, in this case.

For $L \gg \lambda_z$, the wave will experience significant exponential decay within the thick mixed layers. Resonance occurs only for a small range of Δ, the values of which approach $\Delta = (n-1)\pi/m$ as L increases. In this case, an integer number of half wavelengths must fit within the interface, and resonance occurs due to constructive interference in the interface alone, since the reflected wave will also experience significant exponential decay.

In Figure 4.5, resonant transmission occurs at $\lambda_z \simeq 3$m with $L = 2$, which is an intermediate case between these two regimes, in which constructive interference occurs primarily within the interface, but also to some degree within the stratification above the mixed layer (black circle in Figure 4.6). In the Arctic Ocean, most stratified interfaces are quite thin, with Δ on the order of 10cm, while the thickness of the double-diffusive steps varies dramatically, from $L \sim \mathcal{O}(1\text{m})$ or less to $\mathcal{O}(10\text{m})$ or more. Vertical wavelengths range from $\mathcal{O}$(10-100m) or more. This suggests that resonance and wave transmission within the double-diffusive staircase will depend more heavily on the incident vertical wavenumber than on the exact thickness of the stratified interfaces.

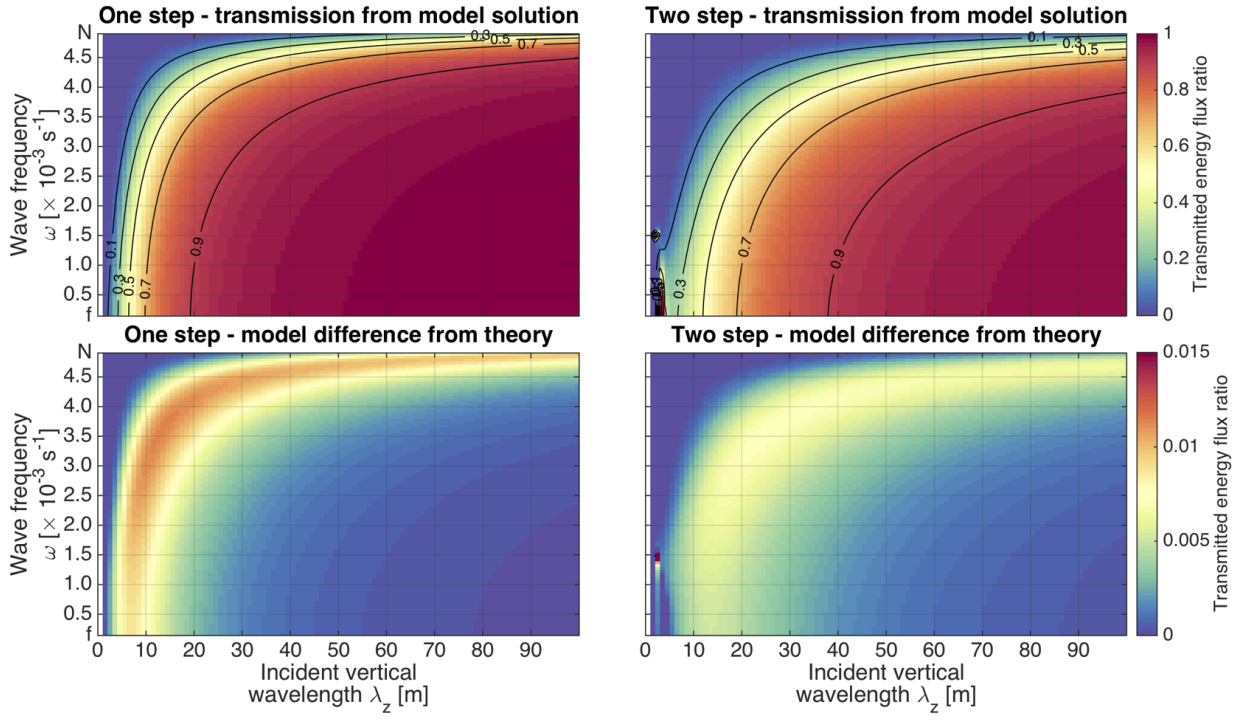

Figure 4.8: As in Figure 4.4 and 4.5, but showing wave transmission calculated by the model. Bottom panels show the difference between the model and the analytic solutions. Note the contour scale difference between the upper and lower panels.

As the goal of this work is to examine the impact of a double-diffusive staircase on internal wave propagation, it is necessary to examine stratifications with many different mixed layers or 'steps', and with different values of N above, below, and between these steps. Equation (4.9) is solved numerically for a series of idealized and measured stratification profiles.

4.5 Numeric solutions

A numerical solution to equation (4.9) is found for waves propagating through a background buoyancy profile $N(z)$ with arbitrary nonuniform stratification, to determine the structure of the internal wave vertical displacement $\tilde{\eta}(z)$, and its derivative $d\tilde{\eta}/dz$ with depth. Equation (4.9) is solved numerically as an ordinary differential equation boundary value problem

(MATLAB *bvp4c* function is used), for a wave of prescribed incident amplitude A_I. The transmitted wave amplitude A_T is determined, with the transmission coefficient physically interpreted as the ratio of the transmitted to incident vertical energy flux.

Two boundary conditions are applied at the boundaries above and below the nonuniform stratification region. Both $\tilde{\eta}(z)$ and $d\tilde{\eta}/dz$ are expressed in terms of the incident, reflected, and transmitted wave amplitudes, and it is required that:

$$\tilde{\eta}(z_1) = A_I e^{-\imath m_1 z_1} + A_R e^{\imath m_1 z_1} \tag{4.21}$$

$$\frac{d\tilde{\eta}}{dz}(z_1) = -\imath m A_I e^{-\imath m_1 z_1} + \imath m A_R e^{\imath m_1 z_1} \tag{4.22}$$

$$\tilde{\eta}(z_2) = A_T e^{-\imath m_2 z_2} \tag{4.23}$$

$$\frac{d\tilde{\eta}}{dz}(z_2) = -\imath m_2 A_T e^{-\imath m_2 z_2} \tag{4.24}$$

in which z_1 and z_2 are the depths of the upper and lower boundaries and m_1 and m_2 are the vertical wavenumbers at those depths, where the buoyancy frequency is $N = N_1$ and $N = N_2$ respectively. This provides two conditions at each boundary, and it is noted that the solution is highly sensitive to the values of the background buoyancy frequency at the boundaries (Appendix).

This numerical approach was developed in collaboration with Tom Peacock's research group at MIT, which resulted in a manuscript (Ghaemsaidi, Dosser, Rainville, and Peacock, 2015) that examines internal wave transmission through single and double mixed layers, and through a segment of a measured double-diffusive staircase profile from the Arctic Ocean. The current work represents an extension of that earlier study.

Comparisons between the numeric and analytic solutions for the one and two mixed layer (or 'step') stratifications (Figure 4.8) show that the numeric solutions are very accurate for the parameter range considered, to within 1% for the two step case. Note that the numerical model reproduces the resonant peak in transmission.

Ghaemsaidi et al. (2015b) examined transmission for these cases as a function of the inci-

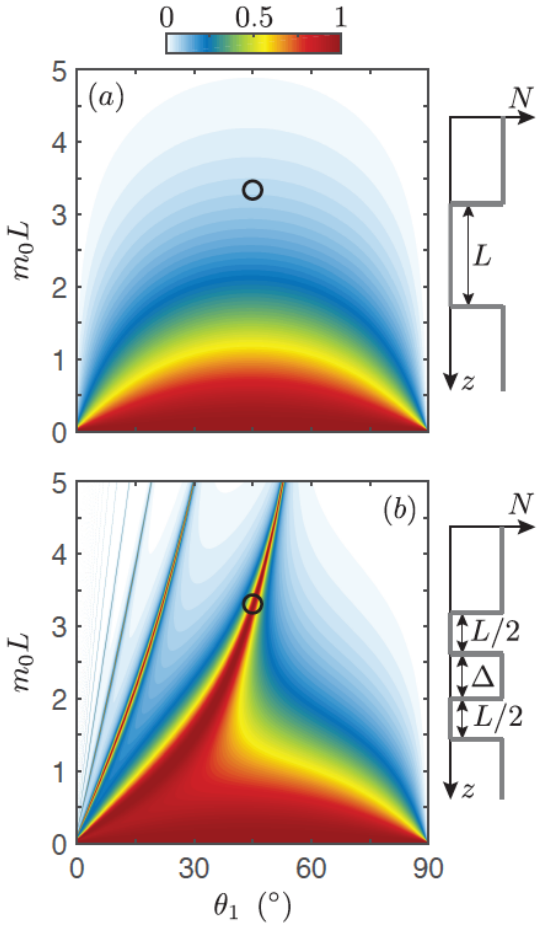

Figure 4.9: From Ghaemsaidi et al. (2015b) (their Figure 3): "Wave transmission for (a) a single mixed layer of thickness L and (b) two mixed layers of thickness $L/2$ separated by a stratification layer of thickness $\Delta = L/2$." Here θ_1 is the angle of incidence of the wave to the horizontal, $\theta = \tan^{-1} k/|m_1|$.

dent wave angle to the horizontal $\theta = \tan^{-1} k/|m_1|$ and $m_0 L \equiv kL$ (Figure 4.9). This allows for a more direct comparison with Sutherland and Yewchuk (2004), (although Sutherland and Yewchuk defined Θ such that $\Theta = \cos^{-1}(\omega/N_0) \simeq 90^o$ corresponds to near-inertial waves, as opposed to $\theta = 0^o$, used herein and by Ghaemsaidi et al. (2015)) and excellent agreement is found for the single mixed layer case (Figure 4.9a). For the case with a stratified interface, a series of transmission peaks is observed. These are attributed to resonance caused by the reflection of internal waves in the uniform stratification regions as discussed above and in (Ghaemsaidi et al., 2015a).

Ghaemsaidi et al. (2015b) also performed a series of laboratory experiments, which were compared with numerical solutions to a version of the Taylor-Goldstein equation that included viscosity. The experiments were performed in a salt-stratified tank, filled via the double-bucket method, with waves generated by an oscillating cylinder within the tank. Wave propagation was measured using particle image velocimetry (PIV). Very good agreement was found with the numerical solutions in both the single and double mixed layer cases (Figure 4.10), with clear wave propagation below the mixed layers, and wave reflection visible off of each mixed layer, including reflection off the lower step in the two step case.

These results provide validation of the numerical model solutions to the Taylor-Goldstein equation for use with layered stratifications, and identify some likely transmission features for internal waves encountering successively more complex stratification profiles.

4.6 Propagation through idealized stratifications

To gain insight into the how different aspects of a double-diffusive staircase stratification affect internal wave transmission, the numerical model is used in this analysis to determine wave solutions for a series of increasingly complex ideal stratification profiles, designed to represent aspects of a realistic double-diffusive stratification. Idealized stratifications considered: *4.6.1*) increased stratification in the interfaces between mixed layers, *4.6.2*) increased number of mixed layers, and *4.6.3*) changing value of N at the boundaries.

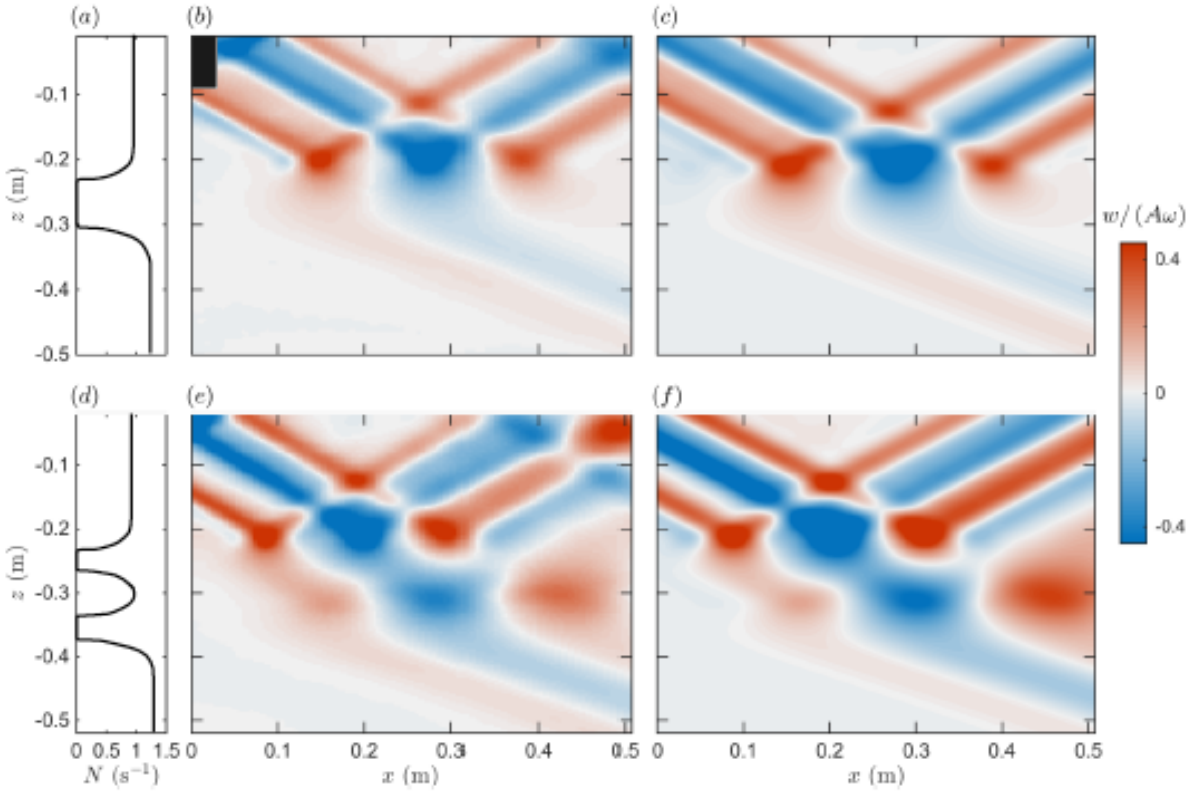

Figure 4.10: From Ghaemsaidi et al. (2015b)(their Figure 5): Internal wave propagation through the stratification shown in the left panels in a laboratory experiment and from the numerical model. "Results for (a) - (c) single and (d) - (f) double mixed layers; snapshots of the experimental (middle column) and theoretical (right column) vertical velocity wavefields are presented at an arbitrary phase. The wavefields have been normalized by the characteristic vertical velocity amplitude."

4.6.1 Interface stratification

Mixed layers within a double-diffusive staircase form when convection locally mixes a continuous density profile. The integrated density with depth remains the same, so that the strength of the stratification in the interfaces between mixed layers must increase to compensate. This is analogous to locally mixing a linear density profile, and requiring that the total change in density with depth $\Delta\bar{\rho}/\Delta z = N_0$ remain constant.

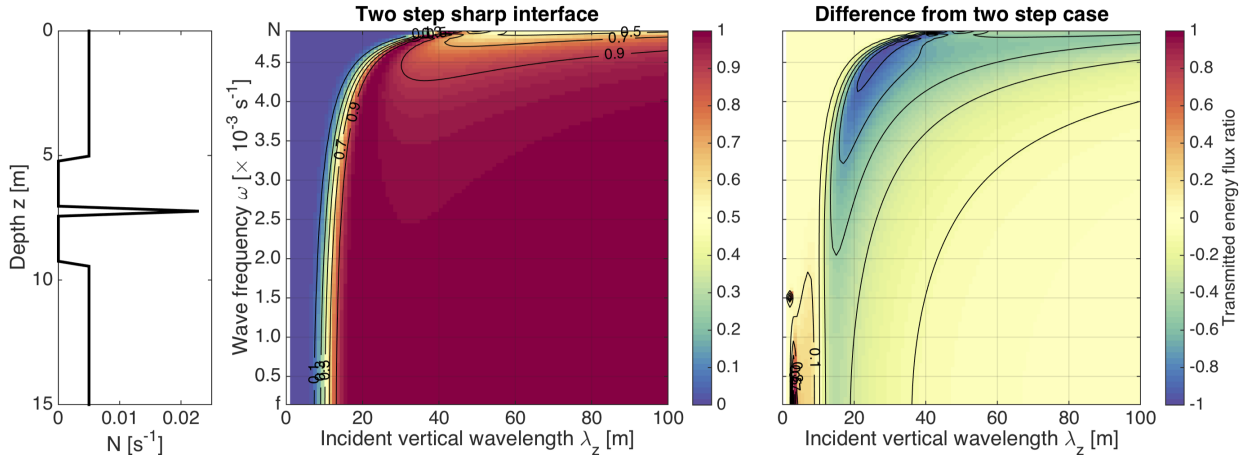

Figure 4.11: Two step stratification with a sharply stratified interface (left panel), and associated wave transmission (middle panel). The right panel shows the difference between the sharply stratified interface case and the two layer stratification in Figure 4.5.

A stratification with two mixed layers and a sharply stratified interface (Figure 4.11) can be compared to the original two step stratification (Figure 4.5), and has similar wave transmission for large vertical wavelengths and $\omega \ll N_0$. However, the small transmission peak at $\lambda_z \approx 3$m caused by resonant transmission within the interface has shifted to a broad transmission peak at about $\lambda_z \simeq 20$m (for $\omega \simeq f$).

This peak is still caused by resonance due to wave reflection within the strongly stratified interface. The stratification within the interface is roughly 5 times stronger than N_0 above the mixed layer, and so the vertical wavelength within the interface is roughly 5 times smaller than the incident vertical wavelength. Therefore, resonant transmission occurs for $\lambda_z \approx 20/5 = 4$m in the interface, consistent with the transmission peak at ∼3m in the original two step stratification.

4.6.2 Number of steps

A double-diffusive staircase is composed of a series of mixed layers separated by thin, strongly stratified interfaces. The number of these steps can be in the decades up to a hundred or

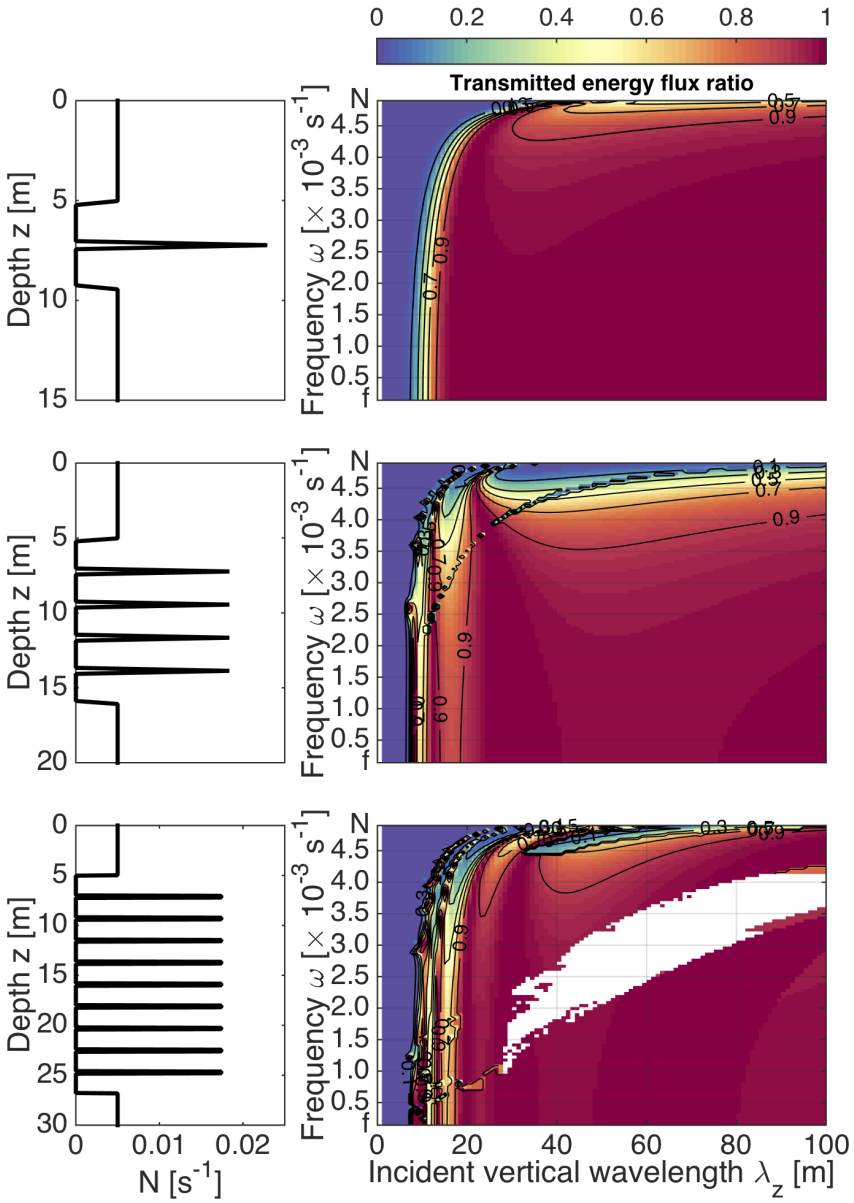

Figure 4.12: Impact on wave transmission of increasing the number of steps in the stratification profile (left column) from 2 (top row, as in Figure 4.11), to 5 (middle row), to 10 (bottom row). (White patches indicate the numerical model was unable to converge on a solution.)

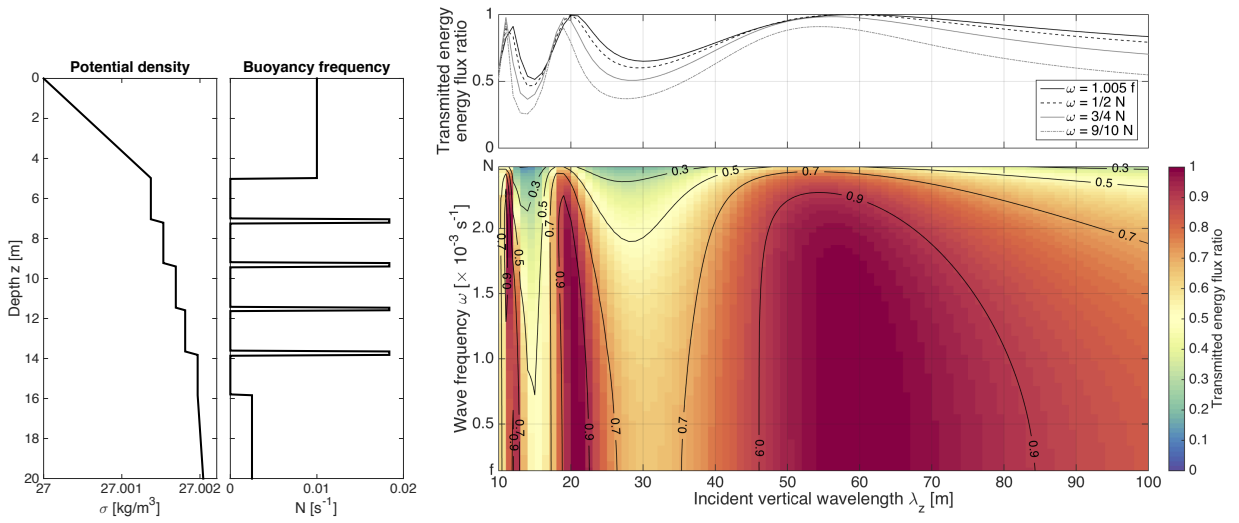

Figure 4.13: Transmission through the 5 step stratification shown at left with $L = 2$m and sharply stratified interfaces with $\Delta = 0.2$m, for which $N_{Top} = 0.01$rad s^{-1} and $N_{Bot} = 0.0025$rad s^{-1}. The top panel shows transmission for select frequencies ω as a function of vertical wavelength λ_z. The maximum wave frequency shown is $N = N_{Bot}$.

more. Increasing the number of steps in an idealized stratification profile with sharp interfaces creates complex transmission patterns (Figure 4.12), with an increasing number of resonant transmission peaks. Note that the numerical model has difficulty converging to a solution for some λ_z and ω in the 10 step case, due to the presence of multiple sudden jumps in N at the 'corners' of each interface. In a measured double-diffusive staircase, the stratification across the interfaces increases smoothly to a maximum, eliminating this issue.

For each additional step, another resonant transmission peak appears (although some are too thin to be visible in Figure 4.12). This is because internal wave reflection occurs in each additional stratified interface, and constructive or destructive interference occurs between the waves incident from above and the waves reflected from every interface below. Resonant transmission still occurs according to the criteria discussed above for the two layer cases, but the peaks are broadened by the successive reflections, as the oscillations need only be approximately in phase between successive layers. The overall effect is to selectively transmit

certain vertical wavenumber bands, while largely reflecting others.

In the limit that λ_z is much larger than the non-uniform stratification region, even the case with 10 steps shows almost complete transmission, as expected. However, for λ_z less than or comparable to the thickness of the non-uniform stratification region, significant wave reflection is often present, when resonant tunnelling does not occur.

4.6.3 Value of N for the boundary conditions

Model sensitivity to the boundary conditions is explored in detail in the Appendix. For a real ocean stratification profile, a constant value of N is imposed above and below the double-diffusive staircase. This ensures that the incident and transmitted waves have well-defined vertical wavenumbers and are not evanescent. The values used are representative of the measured stratification immediately above and immediately below the staircase.

These boundary values for N are determined by smoothing the measured density profile on a 30m scale, and using a spline-fit to ensure that the total integrated density matches that of the original profile. In other words, the smoothed density profile approximates the density profile that existed prior to double-diffusive mixed layer formation. The constant values of N at the boundaries are chosen to match N_{Top} and N_{Bot} from the corresponding smoothed $N(z)$ profile, where 'Top' denotes the upper boundary and 'Bot' the lower.

For a double-diffusive staircase, $N_{Top} \gg N_{Bot}$. Density increases rapidly over the upper staircase and slowly in the lower staircase, below the Atlantic Water temperature maximum. The impact of such a change in stratification between the boundaries is significant (Figure 4.13, for which $N_{Top} = 0.01\text{rad s}^{-1}$ and $N_{Bot} = 0.0025\text{rad s}^{-1}$). When making comparisons with previous results, note that doubling N_{Top} approximately halves the value of the incident vertical wavelength (Appendix), so that $\lambda_z = 30\text{m}$ in Figure 4.13 is equivalent to $\lambda_z \simeq 60\text{m}$ in previous sections for which $N_{Top} \equiv N_0 = 0.005\text{rad s}^{-1}$. Thus, a comparison with the five step profile in Figure 4.12 should consider $\lambda_z \leq 50\text{m}$ in Figure 4.13.

The transmission peaks in the case with realistic boundary conditions (Figure 4.13) have become more distinct, with wave reflection occurring for a wider range of wavelengths be-

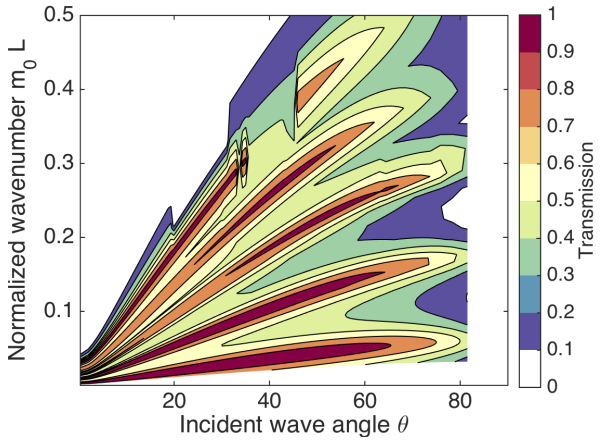

Figure 4.14: Transmission through a 5 step stratification with step thickness $L = 2$m and sharply stratified interfaces of thickness $\Delta = 0.2$m, for which $N_{Top} = 0.01$rad s^{-1} and $N_{Bot} = 0.0025$rad s^{-1}. Wave transmission is plotted as a function of the evanescent vertical wavenumber m_0 within the mixed layers and the incident wave angle to the horizontal $\theta = \tan^{-1} k/|m_1|$.

tween them. No analytic prediction exists for the location of the transmission peaks, however it would involve additional parameters for the ratios of the vertical wavenumbers above and below the varying stratification region, within the stratified interfaces and the mixed layers.

Resonant transmission still occurs for integer multiples of some constant times the vertical wavenumber. Visualized similarly to the transmission peaks observed by Sutherland and Yewchuk (2004) for internal waves encountering an 'N^2-barrier', peaks occur for increments of $m_0 L$ (Figure 4.14), where $m_0 = k$ for non-rotating waves. Increased transmission is still due to resonance between the incident and reflected waves within each stratified interface. Focusing on near-inertial waves, transmission is reduced by as much as to $\sim$50% for incident vertical wavelengths of $\lambda_z \leq 50$m and by up to $\sim$30% even for long incident vertical wavelengths, $\lambda_z > 50$m. This idealized stratification is the best approximation to a real double-diffusive staircase stratification examined herein.

In summary

1) Internal waves can tunnel through one or more mixed layers, even when their vertical wavelength is less than or comparable to the mixed layer thickness.
2) For multiple mixed layers separated by stratified interfaces, resonant transmission peaks cause the stratification to act as a filter on the propagation of waves in certain vertical wavenumber bands.
3) For a staircase-like profile, even waves whose vertical wavelength is much larger than the non-uniformly stratified region can experience significant reflection, at all frequencies.

4.7 Propagation through observed double-diffusive staircase stratifications

The idealized stratifications investigated above outline effects of layered stratifications on internal wave propagation, and provide physical explanations for different transmission features. Observed Arctic double-diffusive staircase stratifications are investigated using the same numerical model to determine their impact on internal wave propagation and stability.

4.7.1 Data

Detailed measurements of the double-diffusive staircase in the Western Arctic were made during the "Beringia" cruise from August 19th to September 25th, 2005, aboard the ice-breaker Oden (Rainville and Winsor, 2008). The cruise crossed the Canada Basin from south to north, then proceeded past the North Pole across the Amundsen Basin. Measurements included regular CTD and microstructure profiles, and rapid sampling CTD profiles taken with a Rockland Scientific Vertical Microstructure Profiler (VMP).

The regular CTD profiles are from the ship's rosette CTD, and have a typical vertical resolution of about 1m. The vertical resolution is due mostly to the response of the temperature and conductivity sensors (which are matched in processing), and the fast profiling speed ($\sim$1m/s) of the large rosette, which also entrains some water as it profiles. During "Beringia", Rainville and Winsor made several profiles using a smaller VMP, on which SeaBird 3 and 4

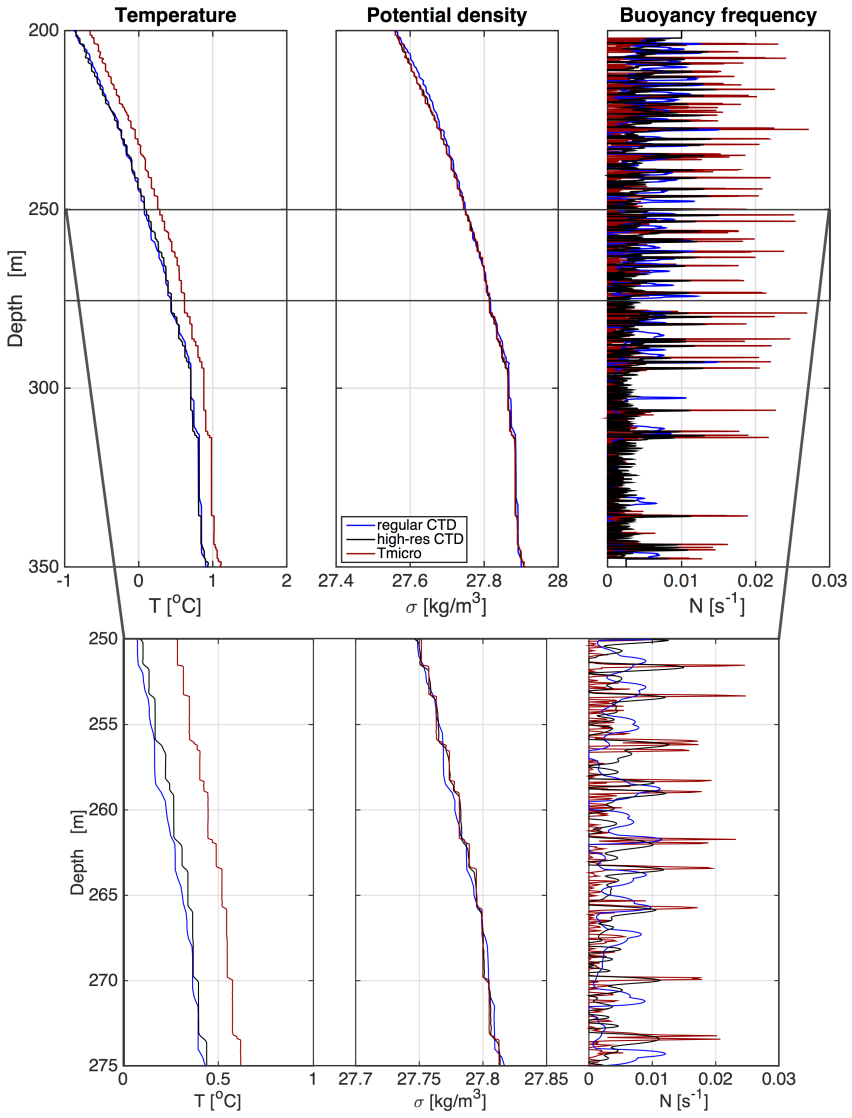

Figure 4.15: Temperature, potential density, and buoyancy frequency from a regular CTD (blue), a fast sampling CTD (black) and a temperature microstructure profiler (red, with density from the regular CTD). Bottom row shows a larger version of the depth range 250-275m, chosen to show details of the smaller steps in the staircase.

temperature and conductivity sensors were mounted and sampled at a faster rate (64 Hz). The resulting density profile from this 'high-resolution CTD' is estimated from the coherence spectrum of temperature and conductivity and has a vertical resolution better than 0.5 m.

Given that it is very difficult to accurately measure both conductivity and temperature (and match them) at higher resolution, an even higher resolution estimate of the stratification profile is obtained by use of a fast response temperature sensor (FPO7, micro temperature sensor) to resolve variations on a centimetre scale. Scaled temperature in a limited range is used to estimate potential density by using temperature as a tracer. Since salinity dominates density, this 'micro-temperature' estimate of density is only approximately valid over a small depth range. Filtering the micro-temperature signal to eliminate turbulence, potential density is likely resolved to about 5cm in the vertical. Data from all three instruments are linearly interpolated to a 5cm grid before buoyancy frequency is calculated.

4.7.2 Staircase description

Profiles from the "Beringia" cruise in the Canada Basin show a distinct double-diffusive staircase above the Atlantic Water temperature maximum. Data from the station at 73^{o}N and 151^{o}W (Figure 4.15) is used with the numerical model discussed above to assess typical internal wave transmission through the staircase. Timmermans et al. (2008a) noted that, due to the lateral coherence of the double-diffusive staircase in the Canada Basin, individual mixed layers could be traced across the entire Basin (roughly 800km). For this reason, a detailed exploration of internal wave transmission through the staircase as measured at a single location may be relevant to much of the central Canada Basin in the Western Arctic.

The staircase observed during "Beringia" extends from $\sim$ 200 to 350m depth, with a series of many of small ($\mathcal{O}$(1m) thick) steps above 300m, and a few very thick steps ($\mathcal{O}$(10m)+) below (Figure 4.15). The stratified interfaces between mixed layers are thin, $\mathcal{O}$(10cm), as measured by the microstructure profiler, and sharply stratified ($N \sim 0.015$rad s^{-1}).

The value of N at the top and bottom boundaries of the staircase is chosen based on smoothing the density profile as described in Section 4.6.3. In this way, $N_{Top} = 0.01$rad

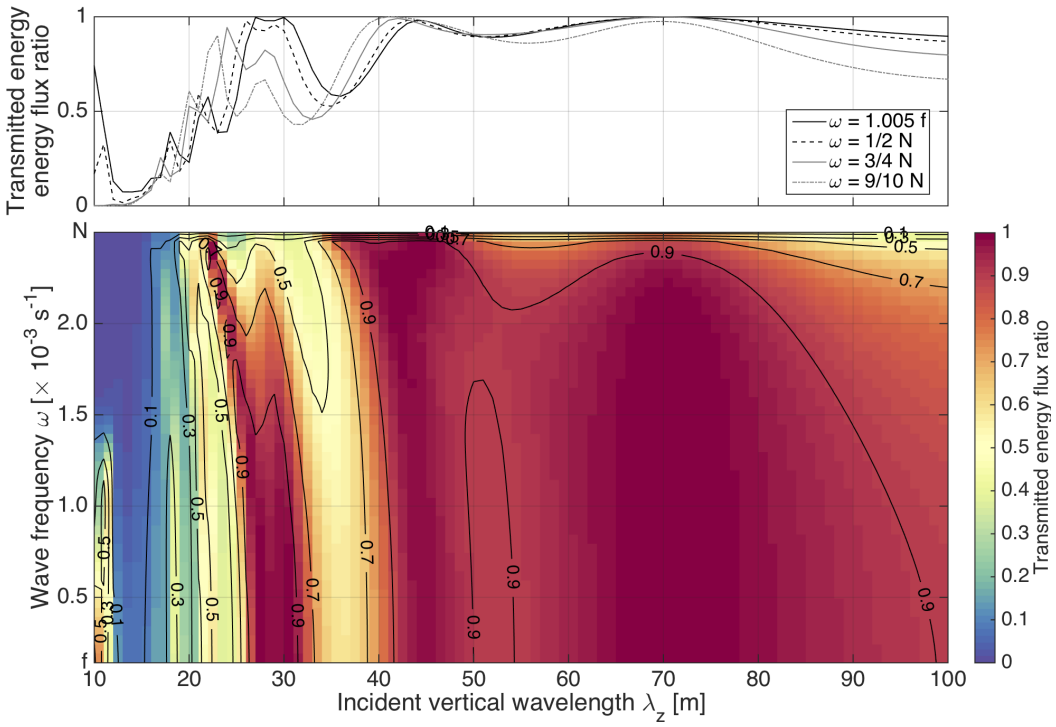

Figure 4.16: Transmitted vertical energy flux for internal waves of given frequency ω and incident vertical wavelength λ_z through a high-resolution CTD profile of the double-diffusive staircase (black line - Figure 4.15), with $N_{Top} = 0.01$rad s^{-1} and $N_{Bot} = 0.0025$rad s^{-1}. The top panels shows transmission for select frequencies. The incident wave amplitude is $A_\eta = 1$m.

s^{-1} and $N_{Bot} = 0.0025$rad s^{-1} are consistent with the observed buoyancy frequencies just outside of the staircase depths, preventing any jump in average N at the upper or lower boundary (Appendix). Within the staircase steps, $N \simeq 0$, but cannot be distinguished from zero within the instrument noise (roughly $\pm 5 \times 10^{-6}$rad s^{-1} for the fast sampling CTD).

4.7.3 Transmission through the staircase

The double-diffusive staircase stratification profile calculated from the fast sampling CTD data (Figure 4.15) is used to numerically determine internal wave transmission (Figure 4.16)

since the fast sampling CTD provides high vertical resolution and measures conductivity, allowing for a direct calculation of density and thus $N(z)$. This stratification profile is used as a 'reference run' representing the best estimate of internal wave transmission through a typical staircase in this region, for comparison transmission through with other profiles.

The ratio of transmitted to incident internal wave vertical energy flux is calculated for a wave whose vertical displacement amplitude is $A_\eta = 1$m, a typical amplitude for the upper Arctic Ocean (Chapter 3: Dosser and Rainville (2015)). Wave frequencies between f and N_{Bot} are considered. The maximum wave frequency possible, $N_{Bot} = 0.0025\text{rad s}^{-1}$, is the background buoyancy frequency at the base of the staircase, and the minimum is $f = 1.4 \times 10^{-4}\text{rad s}^{-1}$, the Coriolis frequency, which varies from $1.35 - 1.45 \times 10^{-4}\text{rad s}^{-1}$ across the Canada Basin.

The incident vertical wavelength λ_z of the waves ranges from 10-100m. Waves with $\lambda_z <$ 10m experience zero transmission through the staircase. Characteristic vertical wavelengths observed for Arctic near-inertial internal waves in the Canada Basin above the staircase depths are in the range 10-50m (Cole et al., 2014). Pinkel (2008) observed near-inertial waves in the Western Arctic on vertical scales between 10 and several hundred meters, and found that waves were energetic over a broader band of vertical wavelengths than is typical for the global ocean, with a fairly flat spectral slope for $\lambda_z > 50$m.

Similarities between the wave transmission through the staircase in Figure 4.16 and wave transmission through the idealized 5 step stratification in Figure 4.13 are immediately apparent. A series of resonant transmission peaks result in near-complete transmission for certain wavelengths, and significant reflection of others. These peaks are quite narrow, so that a near-inertial wave with $\lambda_z = 30$m is completely transmitted through the staircase, while a wave with $\lambda_z = 35$m experiences 40% reflection into the upper ocean, and a shorter wavelength, $\lambda_z = 15$m, wave is almost completely reflected.

Significant internal wave tunnelling is evident at short wavelengths, for example a $\lambda_z =$ 10m wave experiences 75% transmission for $\omega \simeq f$, despite the fact that several steps in the staircase are significantly thicker than 10m. At long wavelengths, transmission increases

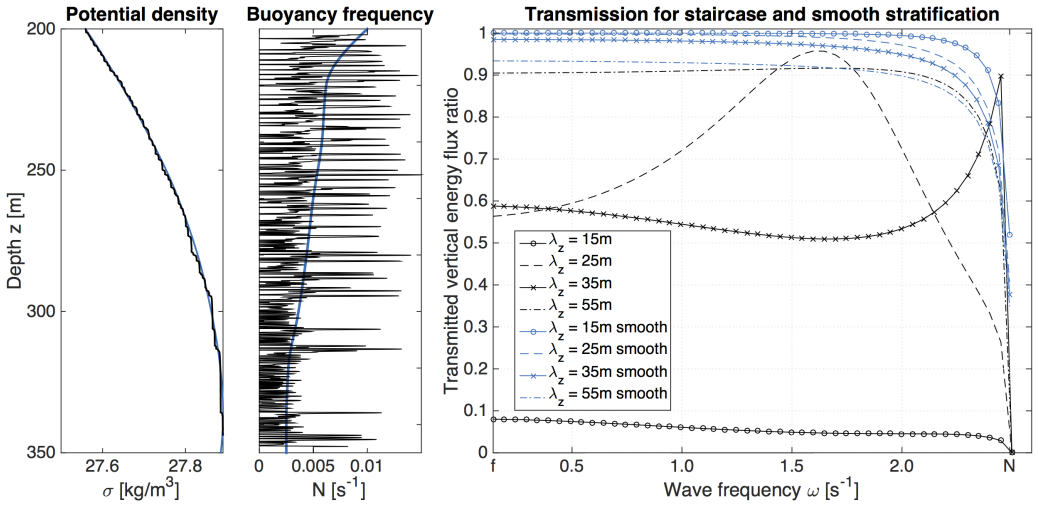

Figure 4.17: Density and buoyancy frequency profiles for the reference run staircase (black) and the corresponding smoothed stratification (light blue). Transmission vs wave frequency is shown for the double-diffusive staircase (black) and the smooth stratification (light blue), for a range of incident vertical wavelengths.

toward 100%, but a wave with $\lambda_z = 100$m still has 10% reflection off the staircase. As the wave frequency increases towards N_{Bot}, transmission decreases. Resonant transmission occurs due to resonance of internal waves within the stratified interfaces, and may also occur for resonance with interfacial waves along the interfaces.

If the double-diffusive staircase stratification is replaced with a smooth density profile in which the overall change in density with depth is conserved, but no mixed layers are present, internal waves experience almost complete transmission (Figure 4.17). Thus the presence of the double-diffusive staircase acts to:

1) Filter wavenumber bands out of the internal wave field reaching the deep ocean, while still allowing certain short initial vertical wavelength waves to transmit by resonant tunnelling.

2) Reflect significant amounts of internal wave energy back into the upper ocean, even for waves whose vertical wavelength is comparable to the total thickness of the staircase.

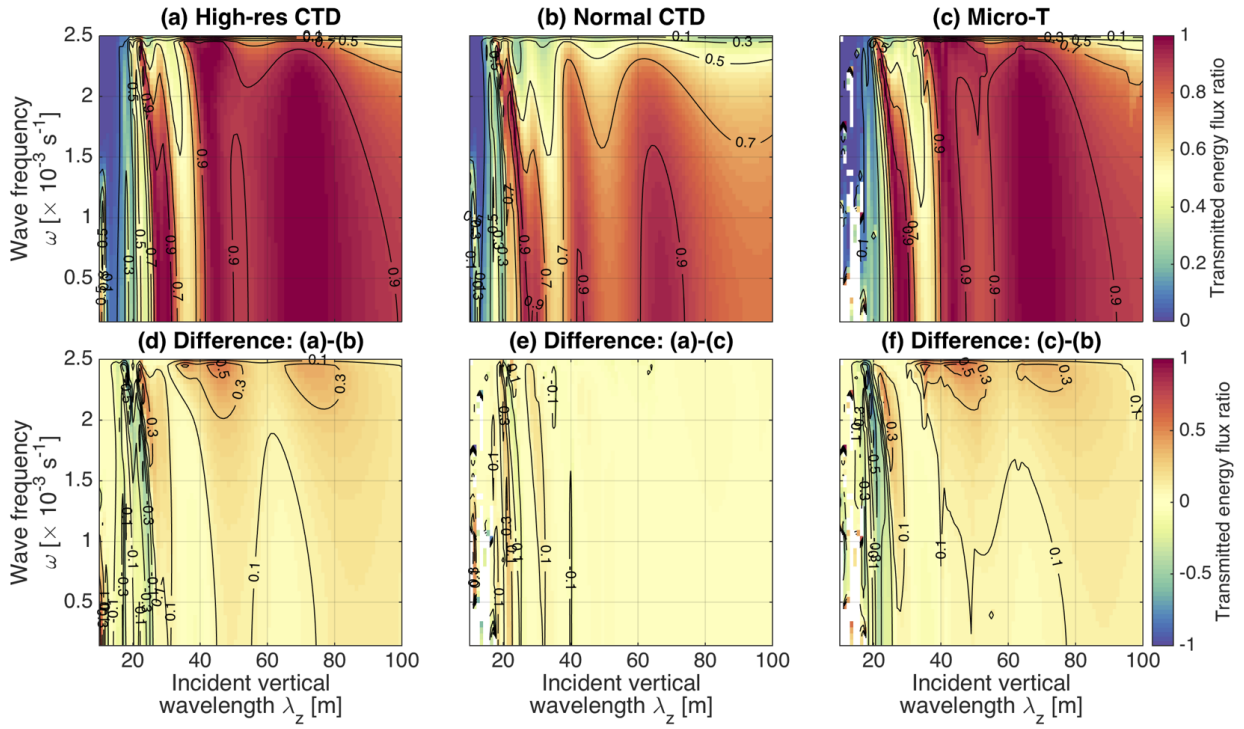

Figure 4.18: Impact of instrument resolution on wave transmission. (a) As in Figure 4.16 for the high-resolution CTD, (b) transmission for $N(z)$ from a regular CTD, and from (c) a temperature microstructure profiler (white patches indicate the numerical model was unable to converge on a solution). Bottom row shows the difference between: (d) the high-res CTD and the regular CTD, (e) the high-res CTD and the microstructure profiler, (f) the regular CTD and the microstructure profiler. Note the different contour scale for the bottom row.

4.8 Observational considerations

Accurate estimates of the impact of measured Arctic Ocean stratification on the internal wave field for different datasets would be of benefit to observational oceanographers (for example, the double-diffusive staircase varies spatially across the Arctic). The numerical model used here could be implemented for stratification profiles anywhere in the Arctic Ocean, though that is beyond the scope of the current investigation.

4.8.1 Instrument resolution

As mentioned previously, the "Beringia" dataset comprises measurements from 3 separate instruments: a regular CTD with nominal 1m vertical resolution ('normal CTD'), a fast sampling high-resolution CTD with better than 0.5m resolution ('high-res CTD'), and a microstructure profiler with ∼5cm resolution ('micro-T'). Such high resolution measurements are rare in the Arctic, but CTD profiles are common. The $N(z)$ profile calculated from each instrument (Figure 4.15) results in slightly different values of wave transmission (Figure 4.18). Note that boundary conditions N_{Top} and N_{Bot} for all three runs are identical.

The difference in internal wave transmission calculated from the microstructure data relative to the high-res CTD is minimal (Figure 4.18e), with less than 5% difference for most wavelengths. This suggests that the vertical resolution from the high-res CTD is sufficient to resolve the details of the staircase that affect internal wave propagation. Differences with the regular CTD (Figures 4.18d,f) are more significant, though still below 15% for $\lambda_z \geq 25$m. Differences for shorter wavelengths are largely due to slight offsets in the location of the transmission peaks relative to λ_z.

The stratification from the regular CTD decreases internal wave transmission (Figures 4.18d,f), consistent with CTD measurements of significantly reduced N within the interfaces. A more strongly stratified interface increases transmission (Figure 4.11), particularly for small λ_z and for $\omega >> f$. The effect of weakened stratification in the stratified interfaces dominates over their artificial thickening relative to the mixed layers (caused by the inability

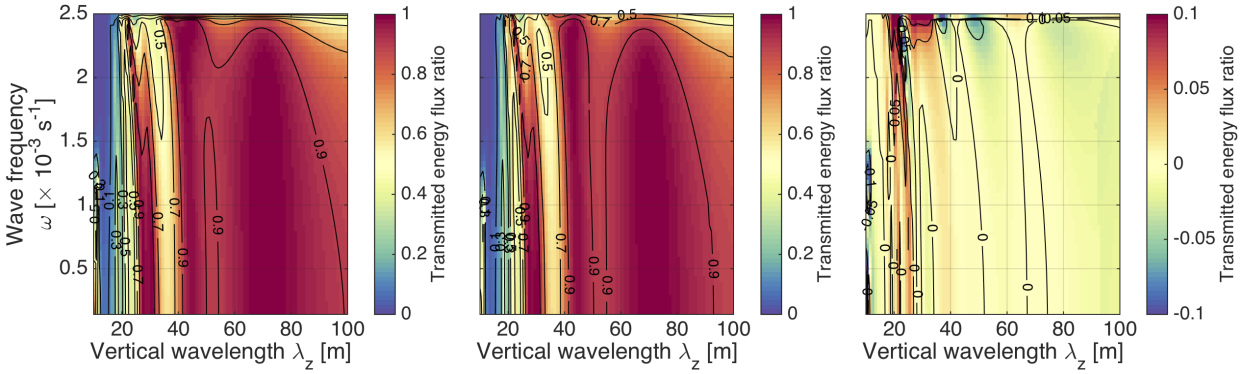

Figure 4.19: Impact of instrument noise removal (by averaging N within the mixed layers of the staircase) on transmitted energy flux. Left panel is the reference run from Figure 4.16. Middle panel shows transmission for the same stratification, but with all values below $N = 5 \times 10^{-6}$rad s^{-1} set to their average value of 4×10^{-7}rad s^{-1}. Right panel shows the difference between the two (note the different contour scale).

of the regular CTD to fully resolve the interfaces, Figure 4.15), which increases transmission (Figure 4.6).

Transmission of internal wave energy determined from a regular CTD profile will underestimate transmission by about 10-15% for most wavelengths for a near-inertial wave, but accurately capture the resonantly transmitted wavelength bands. This suggests that future research can take advantage of datasets such as the Ice-Tethered Profiler data to investigate spatial and temporal variations in internal wave transmission, reflection, and staircase characteristics.

4.8.2 Instrument noise

Due to instrument noise in the measured profiles of temperature and conductivity, values of $N(z)^2 = (g/\rho_0)d\rho/dz$ within fully mixed layers oscillate around $N = 0$ to within roughly $\pm 5 \times 10^{-6}$rad s^{-1}. Instrument noise is removed by averaging all $N(z)$ values below $N = 5 \times 10^{-6}$rad s^{-1}, since the average taken over the noise measured in a mixed layer should be $N \approx 0$. (The actual average value within the mixed layers is $N \sim 10^{-7}$rad s^{-1}.)

Internal wave transmission with instrument noise removed (Figure 4.19) is nearly identical to the reference run, with a difference of less than 5% for most combinations of ω and λ_z. The largest differences of 90%+ occur for waves with $\omega \sim N$. Internal wave transmission is therefore relatively insensitive to instrument noise for $\omega << N$, so a measured stratification profile from CTD data does not introduce significant uncertainty into the result for internal wave energy flux transmission through a layered stratification.

4.9 Stratification considerations

To understand how different aspects of the staircase stratification affect internal wave transmission, the numerical model is used to examine: 1) transmission through the many small, $\mathcal{O}$(1m) thick steps in the upper staircase relative to the several large, $\mathcal{O}$(10m) thick steps in the lower staircase, and 2) transmission through a staircase on the slope in the southern Canada Basin, for which mixing processes have partially eroded the steps, leading to weak stratification or eroded layers rather than the sharply defined steps in the central Basin.

4.9.1 Upper vs lower staircase

The upper portion of the double-diffusive staircase is characterized by a series of many thin $\mathcal{O}$(1m) mixed layers and a rapidly decreasing background density gradient. The lower staircase has comparatively few mixed layers, but they are much thicker, $\mathcal{O}$(10m) or more. The background density changes slowly as both temperature and salinity continue to increase towards the Atlantic Water temperature maximum at the base of the staircase. Double-diffusive staircases exist in regions of the Arctic outside the Canada Basin, but are often quite different from the laterally coherent staircase in the central Canada Basin, with fewer steps of widely varying thickness.

For shorter vertical wavelengths $\lambda_z \leq 50$m, internal waves propagating through the upper staircase (Figure 4.20) have higher transmission than waves propagating through the full staircase, with the exception of those that resonantly tunnel through the staircase in both cases. A near-inertial wave experiences between 10-30% reflection for typical incident vertical

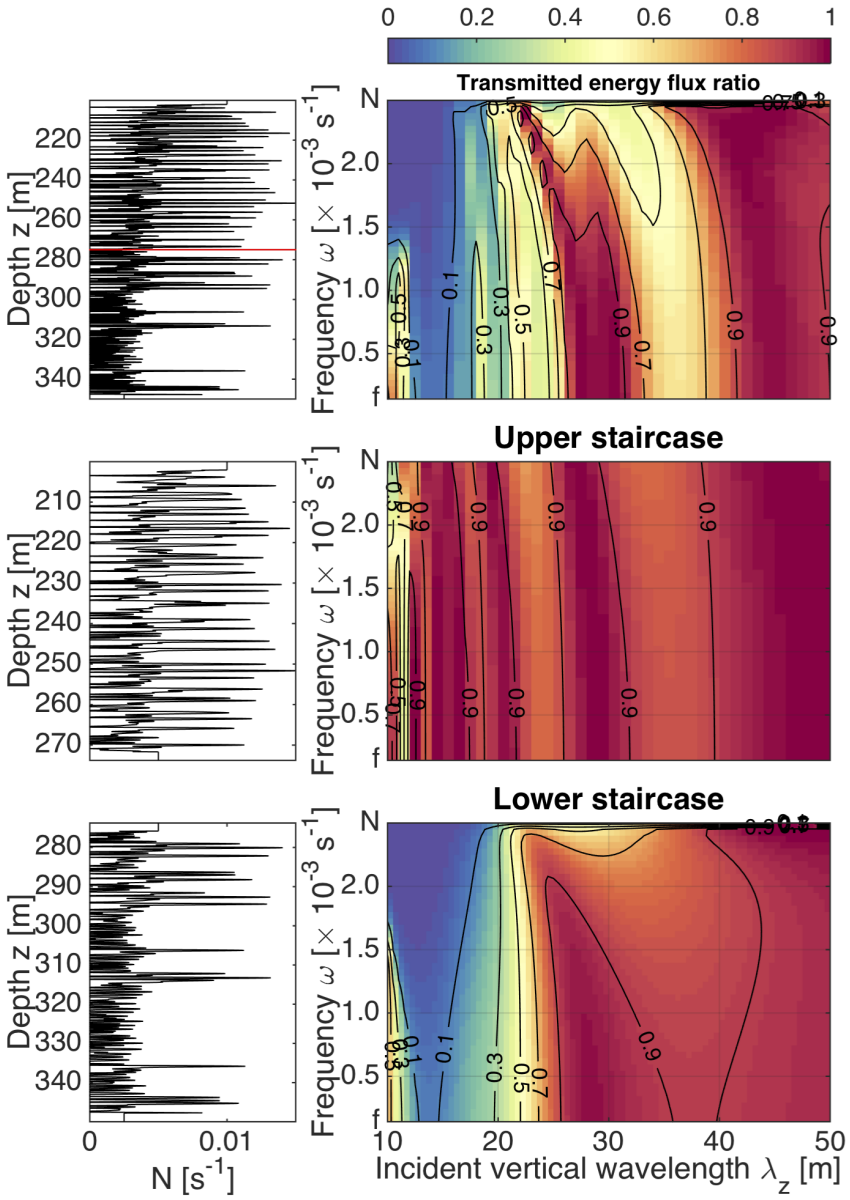

Figure 4.20: Buoyancy frequency profile $N(z)$ and associated transmitted vertical energy flux for: top row - reference run (as in Figure 4.16), middle row - upper staircase (above 275m - red line in 1st panel), and bottom row - lower staircase. The x-axes are scaled to allow direct comparison between runs, despite differing values of N_{Top} (e.g. wave with incident wavelength $\lambda_z = 20$m and $N_{Top} = 0.01$rad s^{-1} in the upper staircase has a wavelength of $\lambda_z \approx 40$m when it encounters the lower staircase with $N_{Top} = 0.005$rad s^{-1}, see Appendix). Thus, the x-axis for all runs shows values of λ_z incident at the top of the staircase at $z = 200$m.

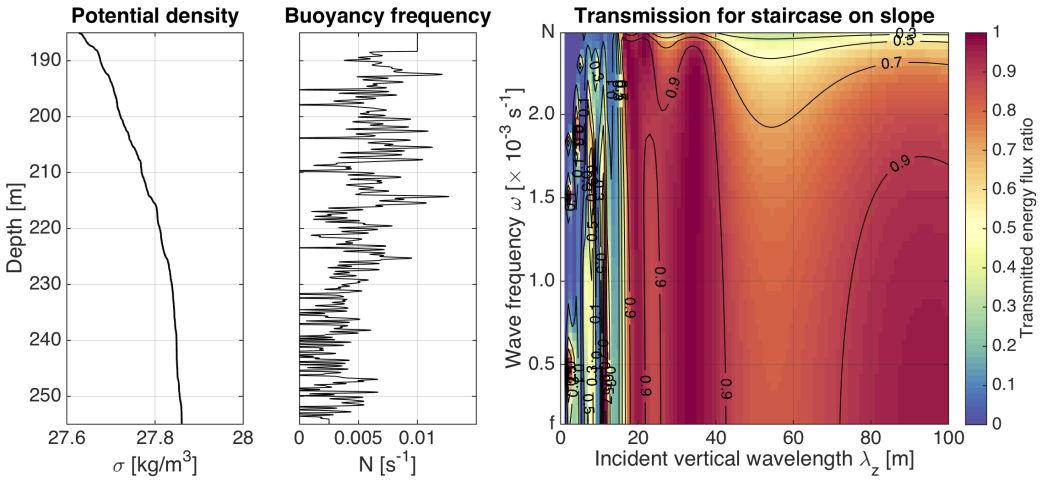

Figure 4.21: Density and buoyancy frequency profiles for an eroded staircase on the slope in the southern Canada Basin and associated transmitted vertical energy flux. $N_{Top} = 0.01$rad s^{-1} and $N_{Bot} = 0.0025$rad s^{-1} as in the reference run (Figure 4.16).

wavelengths, $\lambda_z = 10 - 50$m. Mixed layers within the upper staircase are typically only a few meters thick, smaller than the vertical scale of internal waves in this wavelength range, so that evanescent decay within the mixed layers is small.

Internal waves propagating through the lower staircase (Figure 4.20) experience significant reflection for $\lambda_z < 25$m, with a transmission peak at $\lambda_z \approx 10$m. These waves have vertical scales that are similar to, or smaller than, the thickness of the largest mixed layers. They experience significant evanescent decay across thick mixed layers, causing reflection. For propagation through the full staircase, the upper staircase causes multiple resonant transmission peaks and the lower staircase primarily increases reflection for short $\lambda_z < 25$m waves, and introduces selective reflection of longer λ_z waves.

4.9.2 Eroded staircase on the slope

In the presence of enhanced turbulent mixing due to internal tidal dissipation, frontal instabilities associated with coastal currents, or enhanced shear at the peripheries of eddies, the

sharply defined steps in the double-diffusive staircase can become eroded (Figure 4.21). The result is a staircase in which the interfaces are less strongly stratified and mixed layers may merge or become weakly stratified. Eroded staircases are common at the peripheries of the Canada Basin (Timmermans et al., 2008a). One such staircase was sampled at 72^oN and 152^oW during the 2005 "Beringia" cruise.

The eroded staircase (Figure 4.21) permits enhanced wave transmission, often 50% increase or more, for shorter vertical wavelengths ($\lambda \sim$ 40m or less) relative to the sharply defined staircase used for the reference run (Figure 4.16), including significant transmission for $\lambda_z <$ 10m. Resonant transmission peaks are visible despite the reduced number of fully mixed layers. The eroded staircase allows less wave transmission overall (10-30% reduction) for large vertical wavelength waves, $\lambda_z >$ 50m. It was determined that the presence of thin, sharply stratified interfaces enhanced resonant wave transmission (Figure 4.11) relative to more weakly stratified interfaces. This explains the reduced transmission of large vertical wavelength waves through the eroded staircase.

Internal waves near the slope and shelf are therefore less likely to reflect off the staircase back into the upper ocean if they are of small vertical scale, but are more strongly reflected at longer $\lambda_z >$ 50m. If the staircase in the central Basin becomes eroded in an increasingly energetic Arctic Ocean, this suggests that internal wave reflection from the stratification may decrease for certain wavenumber bands, but increase for the most energetic waves, increasing internal wave energy in the upper ocean.

In summary

1) Profiles of the double-diffusive staircase stratification calculated from CTD measurements provide sufficient resolution to accurately predict internal wave transmission and reflection.
2) The presence of the double-diffusive staircase causes significant reflection of internal wave energy back into the upper ocean.
3) The staircase acts to filter certain vertical wavenumber bands, preventing their transmission into the deep ocean.

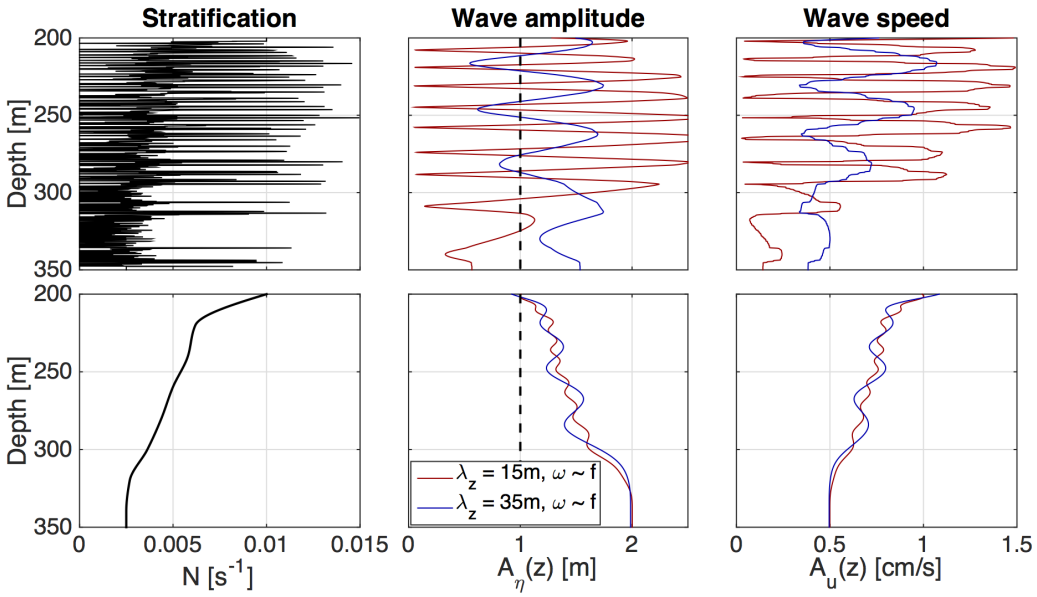

Figure 4.22: Double-diffusive staircase (top) and smoothed (bottom) buoyancy frequency profiles as in Figure 4.17 and the corresponding vertical displacement wave amplitude $A_\eta(z)$ and horizontal wave speed magnitude $A_u(z)$ with depth for a near-inertial wave with $\lambda_z =$ 15m (red) and $\lambda_z = 35$m (dark blue). Dashed black line shows the initial wave amplitude.

4) The characteristics of the staircase, including the number and thickness of the mixed layer steps and the sharpness and thickness of the stratified interfaces, strongly influence internal wave transmission. The impact of the staircase on the internal wave field can be expected to vary both spatially and in time.

4.10 Discussion and implications

Numerical solutions for internal wave propagation through measured stratification profiles have shown that the presence of a double-diffusive staircase in the Arctic significantly affects internal wave propagation and vertical energy flux. The corresponding wave amplitude with depth and thus wave stability are discussed below, with a particular focus on the most energetic internal wave frequency band - near-inertial waves - for:

I) the reflection of internal waves off the staircase relative to a smooth stratification profile,

II) the amplification of internal wave energy within the staircase due to constructive interference with the reflected waves, and
III) gravitational and shear instability for a range of incident wave amplitudes.

4.10.1 I) Wave reflection

If the double-diffusive staircase stratification was not present, internal waves would experience almost no reflection during their downward propagation (Figure 4.17). Waves would propagated unhindered from the surface into the deep ocean; the classical view of internal wave propagation in the Western Arctic. For near-inertial internal waves in particular, which have a small vertical group velocity on the order of 100m/week above the staircase, reflection from the staircase significantly reduces the distance travelled prior to reflection and the time before the waves return to the surface. Note that near-inertial internal wave transmission through a given staircase stratification does not vary significantly across the range of frequencies within the near-inertial band in the Canada Basin.

Two examples of near-inertial wave reflection from the staircase are shown in Figure 4.22 and compared to transmission through a smooth density profile. Vertical displacement and wave speed are lower below the stratified region when compared to values at the same depth for the smooth profile, indicating significant reflection. Wave reflection reduces vertical energy flux to the deep ocean and increases the total energy in the internal wave field in the upper ocean. The presence of such shallow wave reflection may also increase wave-wave interaction in the upper ocean. Wave-wave interactions cannot be investigated with the 1-D numerical model, but constructive interference clearly occurs (Figure 4.22).

As mentioned previously, the staircase acts to filter the vertical wavenumber internal wave spectrum by resonantly transmitting only certain wavenumber bands. This occurs for both downward and upward wave propagation (Figure 4.23). For near-inertial waves, transmission through the staircase occurs for the same wavenumber bands regardless of propagation direction, however for high frequency waves the situation is more complex.

Merrifield and Pinkel (1996) observed that energetic downward propagating near-inertial

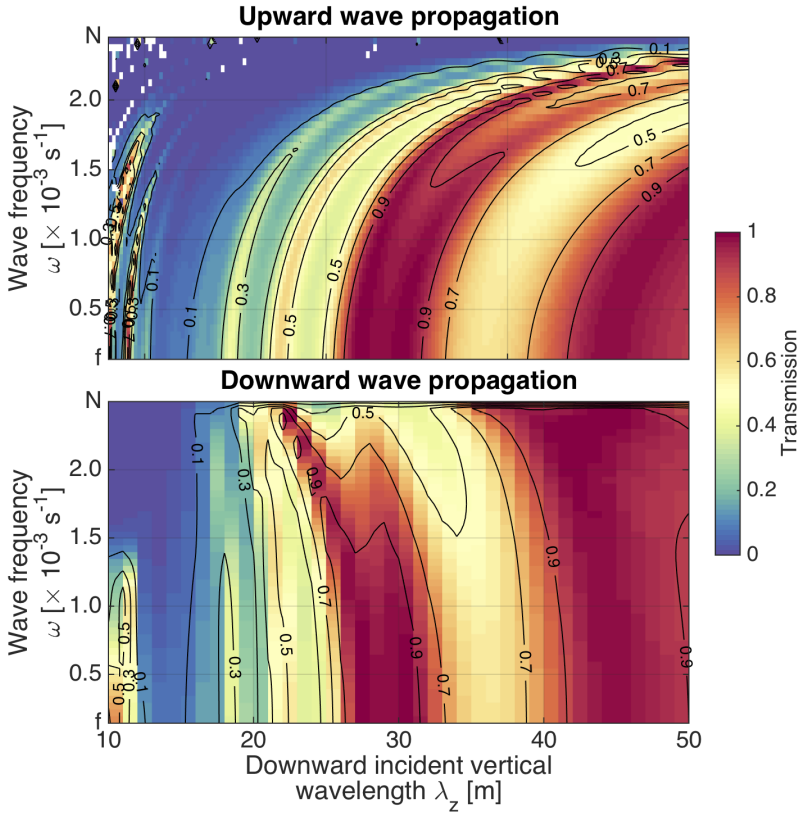

Figure 4.23: Transmitted vertical energy flux ratio for downward internal wave propagation through the reference run double-diffusive staircase stratification (bottom panel) and for upward internal wave propagation through the same stratification (top panel). The x-axis has been scaled for direct comparison between runs, despite the differing values of N_{Top} for the incident waves (Appendix).

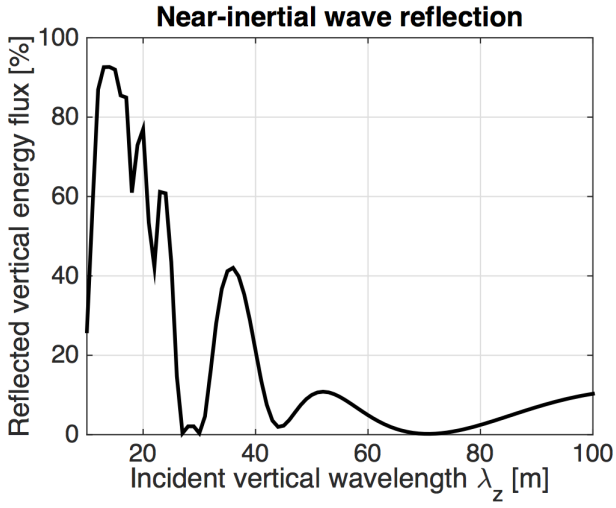

Figure 4.24: Percent reflected vertical energy flux for near-inertial internal waves vs incident vertical wavelength for the reference run double-diffusive staircase stratification.

waves were dominant above 100m in the Beaufort Sea, and energetic upward propagating waves were dominant below that depth. They attributed this separation in part to refraction caused by shear, but the results of this analysis suggest it could also be explained by partial transmission of locally generated, downward propagating waves and partial reflection of remotely generated, upward propagating waves (with different dominant vertical wavenumbers) from a shallow double-diffusive staircase.

The degree of reflection from the staircase is quantified for near-inertial waves specifically in Figure 4.24. Waves with $\lambda_z < 25$m experience between 25-90% energy flux reflection. Long vertical wavelength waves are less affected, but up 10% energy flux reflection is not uncommon for $\lambda_z > 50$m. This has significant implications for the fate of wind energy carried vertically by near-inertial waves.

4.10.2 II) Wave amplification

Due to constructive interference during reflection, internal waves within the double-diffusive staircase can become amplified relative to wave propagation through the corresponding

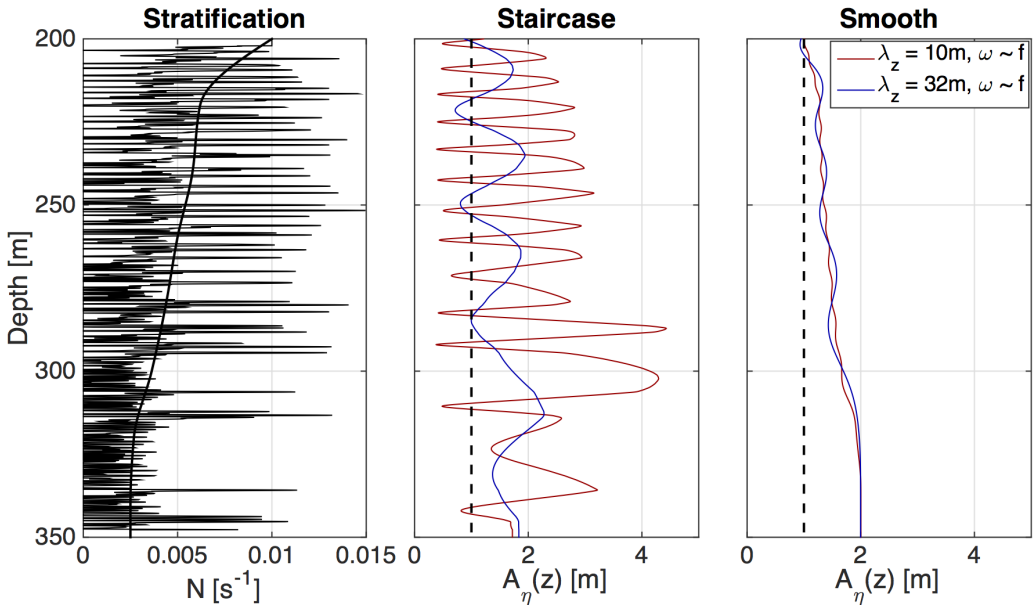

Figure 4.25: Example of wave amplitude amplification within the double-diffusive staircase and the corresponding smooth stratification for near-inertial waves with $\lambda_z = 10$m (red) and 33m (dark blue). Middle panel shows vertical displacement wave amplitude with depth for the staircase. Right panel shows $A_\eta(z)$ for the smooth stratification.

smooth stratification profile. This is somewhat apparent in Figure 4.22, with A_η reaching 2.5m within the staircase relative to 2m for the smoothed stratification. A particularly striking example is shown for a near-inertial wave in Figure 4.25. Note that there is an overall doubling of wave amplitude with depth even in the absence of a double-diffusive staircase due to the background gradient in stratification from $N_{Top} = 0.01$rad s^{-1} to $N_{Bot} = 0.0025$rad s^{-1}, since strong stratification suppresses isopycnal displacements.

Slow variations in stratification can be accounted for by WKB-normalization of the wave amplitude (Figure 4.26), which uses the scaling $A_\eta \times \sqrt{N_{Smooth}/N_{Top}}$, so that a wave that is initially $A_\eta = 1$m in amplitude remains 1m in amplitude while propagating through a smooth, slowly varying stratification. Waves within the staircase are frequently amplified to twice or three times as large as they would be in the equivalent slowly varying stratification

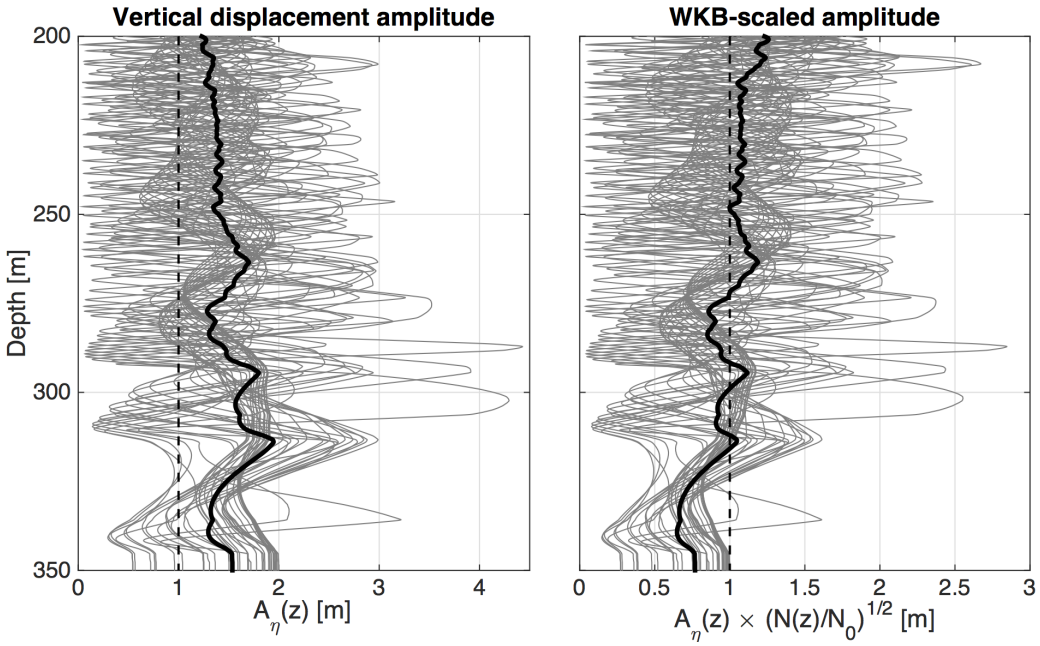

Figure 4.26: Vertical displacement wave amplitude with depth for near-inertial waves propagating through the double-diffusive staircase. Grey lines show $A_\eta(z)$ for incident vertical wavelengths from 10 to 50m, the black line is the average. Right panel shows the amplitude WKB-scaled: $A_\eta(z) \times \sqrt{N_{Smooth}/N_0}$, to adjust for the effect of the background stratification gradient. Here the reference value N_0 is taken to be N_{Top}, so that a WKB-scaled amplitude of 1m indicates complete transmission to that depth. Amplitudes from the smooth profile normalize to 1m.

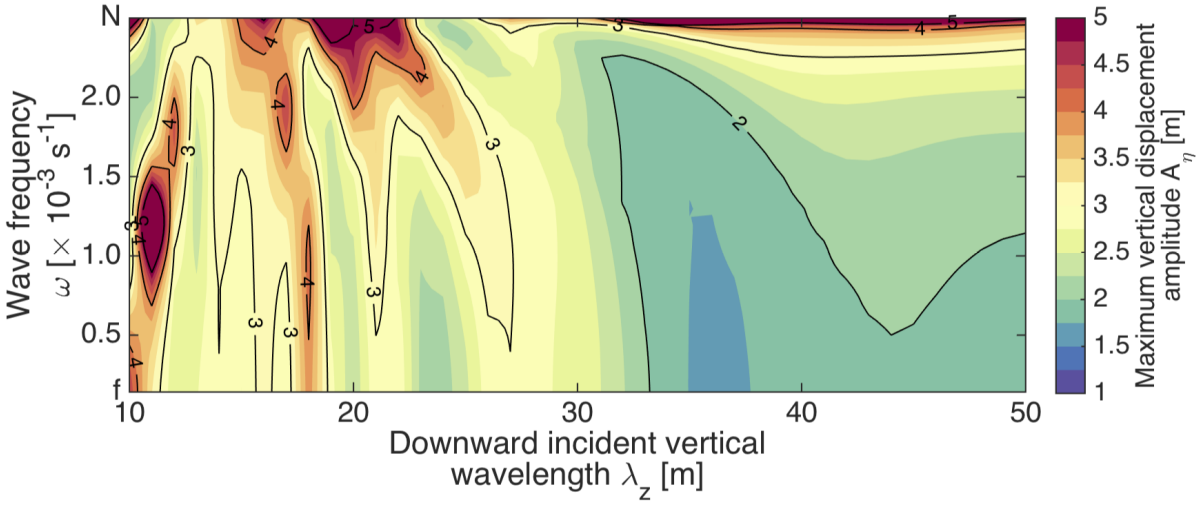

Figure 4.27: Maximum vertical displacement wave amplitude A_η attained within the staircase for internal waves propagating through the reference run staircase stratification with frequencies between f and N_{Bot} and incident vertical wavelengths between 10 and 50m.

with no staircase, for a broad range of λ_z.

The maximum vertical displacement wave amplitude within the staircase (Figure 4.27) is often 4x the incident amplitude or higher for $\lambda_z < 25$m. Even waves with larger incident vertical wavelengths often reach amplitudes up to twice their incident amplitude. This rapid vertical variation in wave energy with depth suggests that internal waves within the double-diffusive staircase may be more prone to instability.

4.10.3 III) Wave instability

The presence, persistence, and coherence of the double-diffusive staircase in the Canada Basin indicates that mixing due to internal wave instability and overturning within the staircase has been relatively rare. Persistent mixing due to internal wave instability in other regions of the Arctic Ocean dominates over double-diffusive convection, effectively preventing the formation of double-diffusive staircases in those locations.

However, the recent decline in sea ice and transition from predominantly multiyear to first-year ice in the Canada Basin has been connected to an increased probability of unusually large near-inertial waves in the upper ocean (Chapter 3: Dosser and Rainville (2015)). The stability of such large amplitude waves within the double-diffusive staircase stratification is certainly worth investigating.

Two types of internal wave instability are considered: gravitational overturning resulting in convective instability and shear instability for the vertical shear associated with the waves themselves. Gravitational overturning occurs if dense fluid is moved above light fluid by the passage of a wave:

$$\frac{\partial \rho_T}{\partial z} \equiv \frac{d\bar{\rho}}{dz} + \left\langle \frac{\partial \rho}{\partial z} \right\rangle < 0, \tag{4.25}$$

for a background stratification profile $\bar{\rho}(z)$ in which density increases with depth. Here ρ_T is the sum of the background density $\bar{\rho}$ and the perturbation density associated with the wave ρ, and $\langle\rangle$ indicates an average over one horizontal wavelength and one wave period.

Then $\langle\rho\rangle = \tilde{\rho}(z)$ can be related to the vertical displacement η determined from the numerical model via equation (4.14):

$$\frac{\rho_0}{g} N^2 + \frac{\rho_0}{g} N^2 \frac{d\tilde{\eta}}{dz} < 0 \tag{4.26}$$

$$\Rightarrow \frac{\rho_0}{g} N^2 \left(\frac{d\tilde{\eta}}{dz} + 1 \right) < 0 \tag{4.27}$$

$$\Rightarrow \frac{d\tilde{\eta}}{dz} < -1 \tag{4.28}$$

the condition for gravitational overturning as a function of depth.

For near-inertial waves, gravitation overturning is generally a sufficient condition for wave instability, however for higher frequency waves this is not always the case. Gravitational overturning results in convective instability only if the growth rate σ of the instability is

higher than the wave frequency (Sutherland, 2010):

$$\sigma = \sqrt{-\frac{g}{\rho_0}\frac{\partial \rho_T}{\partial z}} \geq \omega \tag{4.29}$$

$$\Rightarrow \sqrt{-N^2\left(\frac{d\tilde{\eta}}{dz}+1\right)} \geq \omega \tag{4.30}$$

where σ is real when the waves are overturning.

Internal waves also cause turbulent mixing as a result of shear instability. In the absence of background shear, the vertical shear is provided by gradients in the horizontal velocity associated with the internal waves themselves. If the shear contains sufficient kinetic energy to overcome the restoring force due to buoyancy, then the waves become unstable and overturn. Under the assumption that the horizontal velocity is a function of depth alone, instability is only able to occur when the gradient Richardson number is less than 0.25:

$$Ri = \frac{N^2 + \tilde{N}^2}{(d\tilde{u}/dz)^2} < \frac{1}{4}. \tag{4.31}$$

Here $\tilde{N}^2$ is the change in the buoyancy frequency caused by the passage of the internal wave and $\tilde{u}(z)$ can be related to the vertical displacement through equation (4.12).

The gradient Richardson number condition is:

$$Ri = \frac{(g/\rho_0)\partial\rho_T/\partial z}{\omega^2 m^2 (N^2-\omega^2)/(\omega^2-f^2)\tilde{\eta}^2} \tag{4.32}$$

$$= \frac{N^2}{\omega^2 m^2}\left(\frac{\omega^2-f^2}{N^2-\omega^2}\right)\frac{d\tilde{\eta}/dz+1}{\tilde{\eta}^2} < \frac{1}{4}. \tag{4.33}$$

where m is the incident vertical wavenumber and N is the stratification at each depth. This condition is necessary but not sufficient to guarantee shear instability for $\omega >> f$. Both conditions for instability can be determined using output from the numerical model, which provides $\tilde{\eta}$ and $d\tilde{\eta}/dz$ in the solution to the boundary value problem, eliminating the need to take vertical derivatives of the potentially rapidly varying wave vertical displacement field.

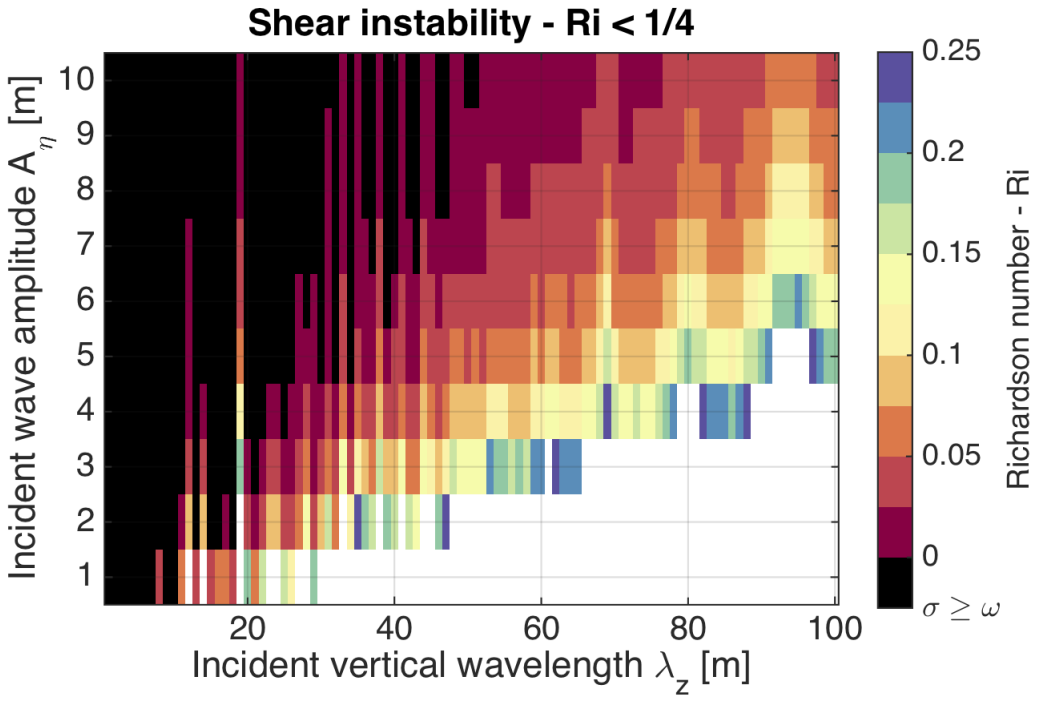

Figure 4.28: Near-inertial internal wave ($\omega = 1.05f$) shear instability as indicated by the gradient Richardson number, equation (4.34), for transmission through the reference run staircase, for a range of incident amplitudes A_η. White indicates waves are guaranteed shear stable, black indicates waves are gravitationally unstable and overturning.

Unlike higher frequency waves, near-inertial waves, whose velocity is primarily horizontal and generally slowly varying relative to the buoyancy period, will undergo shear instability before convective instability (Fritts and Rastogi, 1985). For a typical ocean internal wave frequency spectrum, the kinetic energy for turbulent mixing is largely provided by internal waves undergoing shear instability for a broad range of stratification variations (Kunze et al., 1990; Polzin, 1996).

The majority of near-inertial waves have $A_\eta \leq 5$m in the upper ocean, with an average amplitude of $A_\eta \approx 1$m (Chapter 3: Dosser and Rainville (2015)). Determining a vertical wavenumber spectrum from ITP data would result in prohibitively large uncertainty, however previous estimates of the vertical wavenumber spectrum of horizontal velocity or kinetic

energy for Arctic internal waves exist in the literature. D'Asaro and Morehead (1991) for example show a comparison between the vertical wavenumber spectrum for horizontal kinetic energy from AIWEX in the Western Arctic and two lower latitude sites (their Figure 6). In the Arctic, the wavenumber spectrum flattens for vertical wavelengths longer than $\lambda_z \approx 50$m, with a spectral slope near -0.5, in contrast to the increase in energy with wavelength at lower latitudes (spectral slope near -2).

Because of this, near-inertial wave velocity and isopycnal displacements will be statistically similar for waves with $\lambda_z \geq 50$m, and drop off roughly linearly for shorter wavelengths. As mentioned previously, the peak in the shear spectrum for Arctic internal waves is broad, with a maximum between $\lambda_z = 30-50$m. Therefore, the waves that are most likely to become shear unstable fall near and within the vertical wavenumber band that is most energetic, in contrast to the situation at lower latitudes.

Shear instability is estimated for near-inertial internal waves in Figure 4.28. A wave frequency of $\omega = 1.05f$ is chosen for consistency with the frequency used to determine ITP estimates of A_η (Chapter 3: Dosser and Rainville (2015)). A wave with a median near-inertial wave amplitude $A_\eta \approx 1$m is susceptible to shear instability for vertical wavelengths of 30m or less, and guaranteed stable at long wavelengths. These waves are only potentially unstable over a small fraction of all depths within the staircase (Figure 4.29), which is consistent with the lack of mixing necessary to maintain the double-diffusive staircase stratification.

For a wave with $A_\eta = 2$m, not uncommon in the upper ocean in the Canada Basin, the wavelength range that is shear unstable nearly doubles (Figure 4.28), with some wavelengths near 20m susceptible to shear instability over at least 20% of the vertical extent of the staircase (Figure 4.29). For an unusually large near-inertial wave with 5m vertical displacement amplitude, shear instability is possible for most wavelengths up to 100m, and likely over at least 10% of the staircase for many vertical wavelengths in the range 10m $< \lambda_z <$50m.

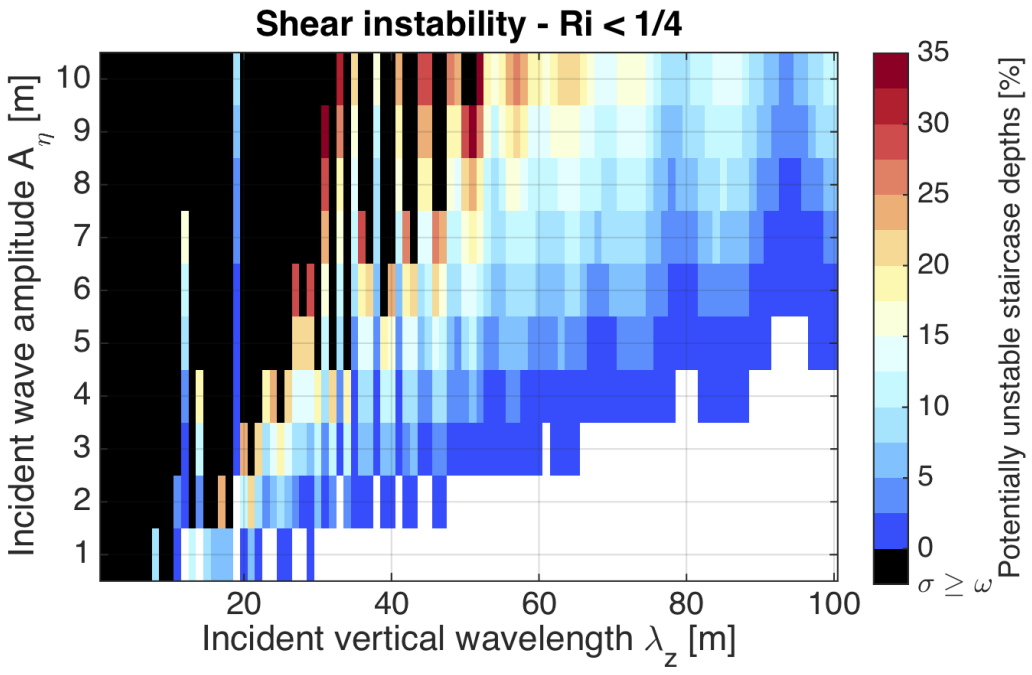

Figure 4.29: Percent of depths within the staircase where waves are susceptible to shear instability based on the Richardson number condition (Figure 4.28), for near-inertial waves ($\omega = 1.05f$) propagating through the reference run staircase. White indicates waves are guaranteed shear stable, black indicates waves are additionally gravitationally unstable and overturning.

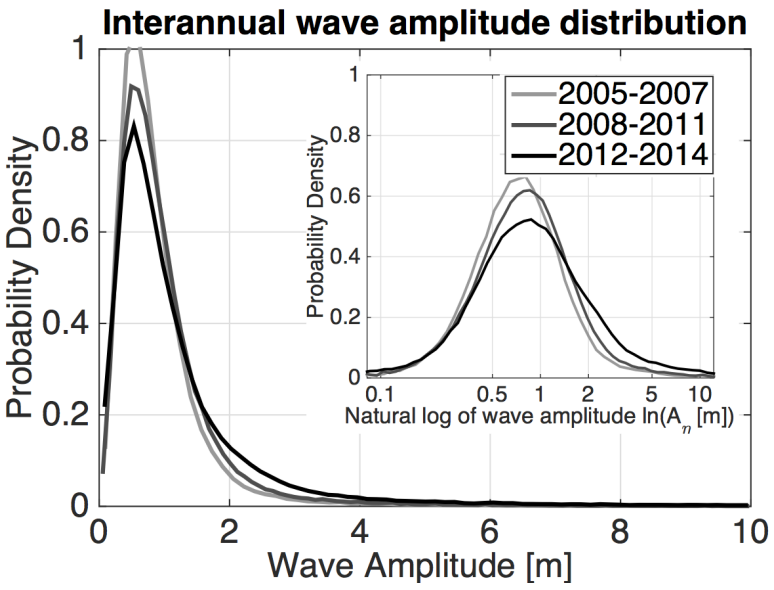

Figure 4.30: Probability distribution for near-inertial internal wave vertical displacement amplitudes determined from the ITP dataset in the Canada Basin during each of the time periods indicated. Inset shows the natural log of the distributions, with select amplitudes labeled. Note that each distribution is normalized so that the integral is equal to one.

4.10.4 Implications for mixing and heat flux

The results for internal wave stability in the double-diffusive staircase suggest that a typical Arctic near-inertial wave with $A_\eta \approx 1$m is stable within the staircase. Internal wave instability is likely intermittent, and caused by the generation of large amplitude waves, $A_\eta \geq 2$m, particularly for vertical wavelengths $\lambda_z \leq 50$m. The probability of mixing due to internal wave instability may have risen in recent years (Figure 4.30), as the variance in the distribution of vertical displacement wave amplitudes doubled (Chapter 3: Dosser and Rainville (2015)), with a significant increase in the number of large amplitude near-inertial waves.

The percentage of all near-inertial waves from the ITP dataset in the Canada Basin with amplitudes in certain ranges is shown in Table 4.1 for different years from Fall 2005 to Fall 2014. In particular, the percent of waves with vertical displacement amplitudes between 2m and 5m more than doubled between 2005-2007 and 2012-2014, while the percent of waves

	Near-inertial wave amplitude [m]			
Year range	$A_\eta \leq 1$	$1 < A_\eta \leq 2$	$2 < A_\eta \leq 5$	$5 < A_\eta \leq 10$
2005-2007	70.8±0.1%	23.7±0.1%	4.6±0.1%	0.7±0.1%
2008-2011	64.6±0.1%	27.6±0.1%	6.7±0.1%	1.0±0.1%
2012-2014	58.7±0.1%	26.8±0.1%	11.7±0.1%	2.4±0.1%

Table 4.1: Percent of near-inertial waves in the upper ocean in the Canada Basin with vertical displacement amplitudes in each range, for each time period listed between Fall 2005 and Fall 2014, from the ITP dataset. Percentage is determined from the empirical cumulative distribution function for each of the distributions plotted in Figure 4.30. Uncertainties are valid at the 95% confidence interval.

with $A_\eta \leq$ 1m dropped by more than 10%. Extremely large amplitude waves, with A_η between 5m and 10m, represent 2% of all waves in 2012-2014, also more than doubling from $\leq 1\%$ in earlier years.

During particularly stormy periods, the percent of large amplitude near-inertial waves can be significantly higher. For example, in the case study in Chapter 3: Dosser and Rainville (2015) for ITP 41, there is a period with consistently high wind forcing and elevated sea-ice speeds from mid-January to mid-February 2012. During this month-long period, only 20% of the waves measured had amplitudes of 1m or less, while 16% of the waves had amplitudes of 5m or greater. Based on the results for wave instability, something like 10-50% of these waves would be expected to become unstable within the double-diffusive staircase, assuming vertical wavelengths in the range 1-100m, potentially causing significant mixing.

The combined results of the numerical model and the ITP dataset suggest that mixing due to internal waves in the Western Arctic has likely increased in recent years, as the probability of generating an unusually large amplitude near-inertial wave in the upper ocean has increased. However, the average wave size remains too small for instability, so that this increase in mixing is likely occurring through intermittent high-energy storm events, increasing the difficulty of direct observation (internal wave instability is outside the ability of ITPs to detect).

The implications for heat flux from the double-diffusive staircase and the Atlantic Water layer can be roughly estimated following the logic of Timmermans et al. (2008a), who considered the potential for turbulent mixing within the staircase to elevate vertical heat fluxes. They assumed that a downward internal wave energy flux was completed dissipated within the thermocline, to get an upper bound on mixing. For a near-inertial wave with $\omega = 1.05f$, a median amplitude of $A_\eta = 1$m, and a typical vertical wavelength of $\lambda_z = 30$m, equation (4.16) suggests a typical vertical energy flux of $|F_z| \approx 0.07$mW m^{-2}. This is in line with estimates from (Halle and Pinkel, 2003), who measured energy fluxes between 0.02 and 0.15 mW m^{-1} for internal waves in the Western Arctic.

Assuming a 150m thick staircase and dividing by its depth H and the average background density ρ_0, the dissipation rate for the kinetic energy from the waves is $\epsilon = |F_z|/\rho_0 H \approx 5 \times 10^{-10}$ W kg^{-1}. The effective vertical diffusivity due to turbulence is then $K \approx \epsilon/5\overline{N^2} \approx 7 \times 10^{-6}$ m^2 s^{-1}, where $\overline{N^2}$ is the average buoyancy frequency across the staircase. (Rainville and Winsor (2008) measured K from microstructure at 10^{-6} m^2 s^{-1} in the deep central Basin, with higher values above the Atlantic Water.) Timmermans et al. (2008a) estimated the corresponding vertical heat flux out of the Atlantic Water using $F_H = K(\rho_0 c_P \overline{\partial\theta/\partial z})$, where $\overline{\partial\theta/\partial z}$ is the average potential temperature gradient across the staircase and c_P is the specific heat of ocean water. This gives $F_H \approx 0.4$W m^{-2} for an $A_\eta = 1$m wave, comparable to the small double-diffusive heat fluxes through the staircase ($F_H = 0.22$ W m^{-2} from Timmermans et al. (2008a)).

Thus, a typical near-inertial wave does not cause elevated vertical heat flux from the staircase and Atlantic Water layer. However, note that since the vertical energy flux from equation (4.16) scales as $|F_z| \propto A_\eta^2$, so does the estimated maximum vertical heat flux caused by the turbulent dissipation of the wave:

$$F_H \approx \frac{\rho_0 c_P}{5\overline{N^2}H}\frac{\overline{\partial\theta}}{\partial z}\frac{\omega}{m}(N_0^2 - \omega^2)A_\eta^2. \tag{4.34}$$

Here $N_0 = 0.01$rad s^{-1} is used as a typical buoyancy frequency in the upper ocean for

consistency with the numerical simulations, and H is the total depth of the staircase across which the wave energy is assumed to dissipate.

A near-inertial wave with an amplitude of 2m increases the heat flux estimate by a factor of 4, and a wave that is 5m in amplitude by a factor of 25, giving $F_H \approx 10\text{W m}^{-2}$, over an order of magnitude larger. This number is likely an overestimate, and certainly not the norm in the Canada Basin. Lique et al. (2014) found vertical heat fluxes from the Atlantic Water in the Canada Basin of only $0.1 - 0.2\text{W m}^{-2}$ on average, though the internal tide over rough topography has been shown to drive heat fluxes of more than 50W m^{-2} in other parts of the Arctic (Rippeth et al., 2015).

The fraction of near-inertial waves with vertical displacement amplitudes between 2m and 5m (Figure 4.30) has risen from 5% in 2005-2007 to almost 12% in 2012-2014 (Table 4.1). Even such a simple calculation for heat flux suggests that the internal wave field in the Western Arctic is capable of driving intermittent yet significant vertical heat fluxes from the Atlantic Water layer toward the upper ocean and the sea ice, with the likelihood of such events having more than doubled during recent years.

4.11 Summary

Results from the numerical model for the vertical evolution of an internal wave propagating through a layered double-diffusive staircase stratification indicate that the stratification has a significant impact on the structure and stability of the internal wave. In particular:

1) The staircase causes significant internal wave reflection, with resonant transmission restricted to certain wavenumber bands. Near-inertial waves experience up to 90% reflection of energy flux for a typical double-diffusive staircase for certain incident vertical wavelengths with $\lambda_z < 30\text{m}$, while other wavelengths experience near-complete transmission. The staircase stratification increases the total internal wave energy in the upper ocean, and acts as a filter on the vertical wavenumber spectrum.

2) Internal waves in the staircase are susceptible to instability and overturning. Near-inertial waves with vertical displacement amplitude typical for the Western Arctic, $A_\eta \approx 1\text{m}$,

are stable to both gravitational and shear instability, however the percent of near-inertial waves from the ITP dataset that are likely to experience instability within the staircase more than doubled between 2005-2007 and 2012-2014. These large amplitude waves, $A_\eta \geq 2$m, are intermittently generated, and now represent about 12% of the near-inertial wave field in the Western Arctic Ocean. They have the potential to episodically increase vertical heat flux from the Atlantic Water by up to an order of magnitude if and when they break, particularly for waves with vertical wavelength $\lambda_z \geq 50$m.

The near-inertial wave field in the western Arctic Ocean has evolved in recent years as sea ice has rapidly declined and multiyear ice has been replaced by first-year ice. The average energy of the wave field has not increased significantly, however highly energetic waves are now more likely to be generated. Internal wave theory suggests that the vertical structure of these waves is significantly modified by the stratification in the Western Arctic, in particular by the double-diffusive staircase within the Atlantic Water layer. This has the potential to drive wave instability for the most energetic near-inertial waves, possibly increasing episodic mixing and vertical heat flux.

4.12 Appendix: Sensitivity to boundary values of N

The numerical model solves a boundary value problem, with an incident internal wave specified outside the depth-varying stratification region, in this case above the double-diffusive staircase, and a transmitted wave below. Constant buoyancy frequency values N_{Top} and N_{Bot} are imposed above and below the staircase, chosen to be consistent with the corresponding smoothed density stratification (the stratification that would exist in the absence of double-diffusive convection).

The transmission is sensitive to the values of N_{Top} and N_{Bot} (Figure 4.31). N_{Bot} sets the maximum wave frequency allowed for a freely propagating internal wave, since ω is restricted to $f < \omega < N$ for the incident and transmitted wave, and $N_{Bot} < N_{Top}$ for a double-diffusive staircase. In Figure 4.31 (c) and (d), the frequency range is cut off at $N = 0.0025$rad s^{-1} for comparison purposes, but transmission occurs for ω up to $\omega = N_{Bot} = 0.005$rad s^{-1}.

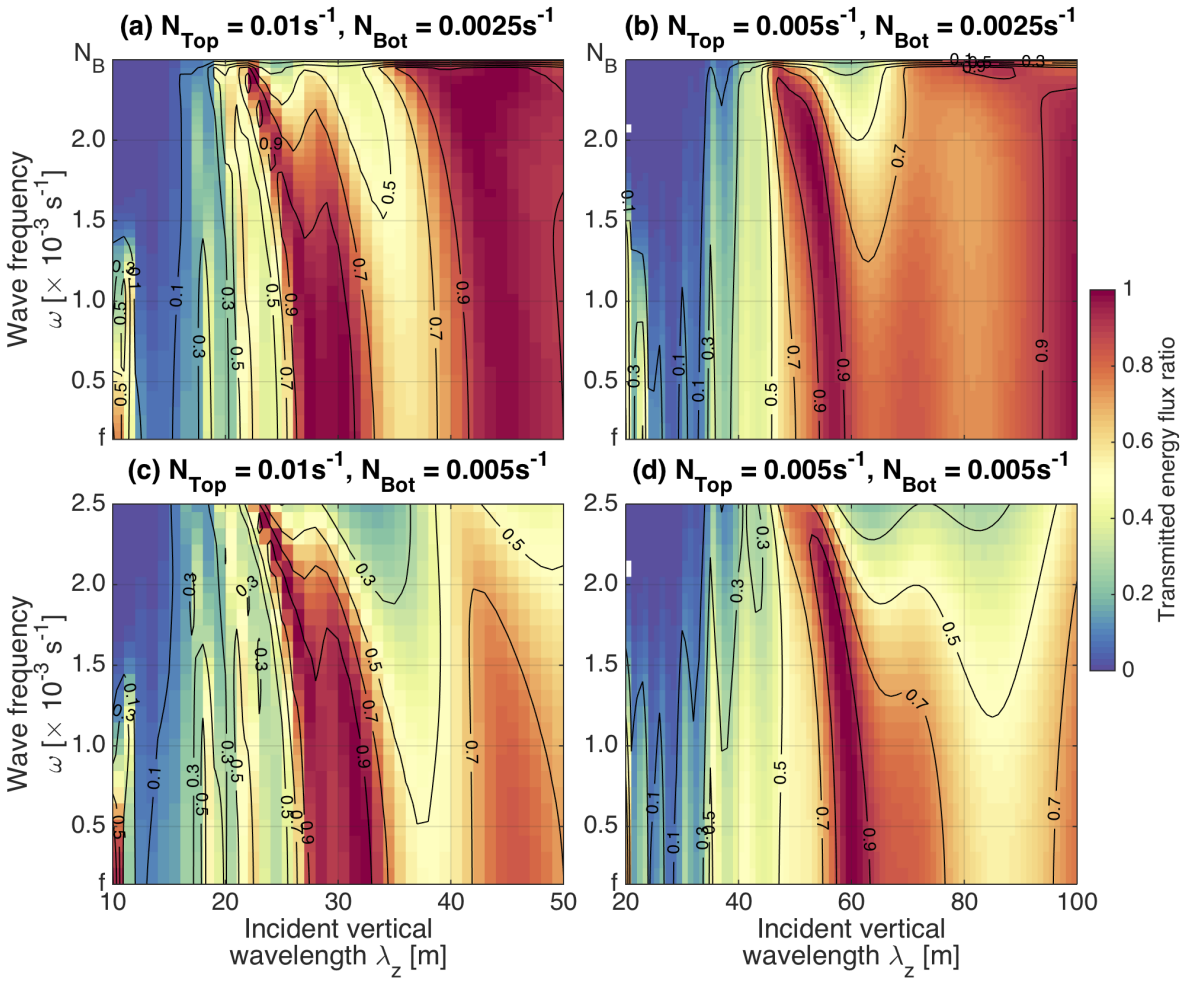

Figure 4.31: Internal wave transmission through the reference run double-diffusive staircase with: (a) the top and bottom values of the buoyancy frequency, N_{Top} and N_{Bot} consistent with the smooth stratification profile (values used in the reference run), (b) a top buoyancy frequency value that is half as large, (c) a bottom buoyancy frequency value that is twice as large, (d) top and bottom buoyancy frequency values that are equal.

N_{Top} affects the vertical wavelength of the incident internal wave. Since the horizontal wavelength and the frequency of a given incident wave are taken as fixed, the dispersion relation, equation (4.10), gives:

$$m_1 = \pm k\sqrt{\frac{N_{Top}^2 - \omega^2}{\omega^2 - f^2}} = \pm C_o\sqrt{(N_{Top}^2 - \omega^2)} \tag{4.35}$$

where m_1 is the incident vertical wavenumber and C_o is a constant. So an internal wave with a vertical wavelength λ_{z0} in a stratification with N_{Top0}, is equivalent to a wave with

$$\lambda_z = \sqrt{\frac{(N_{Top0}^2 - \omega^2)}{(a^2 N_{Top0}^2 - \omega^2)}}\lambda_{z0} \approx \frac{1}{a}\lambda_{z0} \tag{4.36}$$

in a stratification with $N_{Top} = aN_{Top0}$. As an example, a wave with an incident vertical wavelength of 10m with $N_{Top} = 0.01\text{rad s}^{-1}$ is equivalent to a wave with a vertical wavelength of around 20m for $N_{Top} = 0.005$. For this reason, the incident vertical wavelengths in Figure 4.31 (b) and (d) are double those in (a) and (c), for which N_{Top} is twice as large.

Lastly, internal waves experience lower transmission in general for reduced N_{Top} (Figure 4.31b) or increased N_{Bot} (Figure 4.31c), relative to top and bottom buoyancy frequencies that are determined from a smoothed version of the N profile (Figure 4.31a). The reduced value of N_{Top} or increased value of N_{Bot} means that incident waves encounter an unphysical increase in the average buoyancy frequency when they reach the staircase or that waves within the staircase encounter an unphysical increase in average buoyancy frequency when they exit the base of the staircase, respectively, inconsistent with the measured stratification profile. This in creases wave reflection, particularly for longer vertical wavelength waves.

The key points are, first, that the values of N above and below the staircase must be chosen with care to match the measured stratification, and second, that comparison of wave transmission through different stratifications must account for the effect of N_{Top} on the incident vertical wavelengths considered.

Chapter 5

SUMMARY AND IMPLICATIONS

5.1 Main results

The goal of my PhD research is to assess the importance of internal waves in the Western Arctic Ocean; to determine spatial and temporal variations in the internal wave field and the fate of the energy transported by surface generated internal waves.

The near-inertial internal wave field in the Canada Basin between Fall 2005 and Fall 2014 has been quantified using the Ice-Tethered Profiler dataset and the complex demodulation technique to determine over 7500 independent estimates of vertical displacement wave amplitude. Ensemble Monte-Carlo simulations are used to quantify the associated uncertainty.

The average near-inertial wave field is shown to have a large-scale spatial pattern, with a roughly linear decrease in wave amplitude of 12% per degree latitude to the north. This trend is only partially explained by spatial variations in sea ice, including thicker, older ice cover in the north-east of the Basin, and also by a slight temporal measurement bias in ITP sampling. ITPs are initially deployed as far north in the Canada Basin as possible during September, so that ITPs often reach the southern Basin the following summer.

Near-inertial waves have a seasonal cycle, with a median wave amplitude that is 16% larger during summer and fall (June to November), when compared to winter and spring (December to May). The peak in wave amplitude occurs in September, when sea-ice concentration is at a minimum and the ice moves rapidly in clockwise inertial rotation in response to wind forcing. A slight increase or plateau in wave amplitude is observed in December - January, corresponding to an increase in average wind speed, with numerous winter storms producing winds over 10m/s. The lowest wave energy is in March, when ice concentration is at 100%, and ice drift speeds are at their minimum, indicating that the wind is unable to

easily transfer momentum to the ice pack.

A slight, increasing interannual trend in average wave amplitude is found for both summer and winter, with the median wave amplitude increasing by 5% over the course of the 9-year record. Seasonal differences in average wave amplitude increased after 2007, becoming particularly extreme after 2012. The variance in the distribution of wave amplitudes doubles between the years 2005-2007 and 2012-2014, indicating a significant increase in the number of unusually energetic near-inertial waves in the Canada Basin in recent years.

The propagation and likely fate of internal waves in the Western Arctic Ocean is investigated by numerically solving the Taylor-Goldstein equation for the vertical evolution of a specific internal wave propagating through a given stratification. The double-diffusive staircase, a stratification feature at roughly 250-400m depth composed of a series of mixed layers of widths ranging from about a meter to tens of meters, separated by thin stratified interfaces, was shown to significantly affect internal wave propagation. The staircase was accurately defined using high-resolution CTD measurements in the Canada Basin.

For internal waves with vertical wavelengths between 1m and 100m - a representative range for the Arctic Ocean - the staircase causes significant reflection of wave energy back into the upper ocean. For short-wavelength near-inertial waves, $\lambda_z \leq 50$m, reflection of between 50-100% of the incident wave energy is predicted. For long-wavelength waves, $\lambda_z \geq 50$m, reflection of $\sim$10% of the incident wave energy is possible.

Certain vertical wavenumber bands are completely transmitted through the staircase stratification by resonant tunnelling. This occurs when the vertical wavelength of the incident wave is such that oscillations within the stratified interfaces are resonant over the full depth of the staircase, so that despite the evanescent decay of the internal waves within the mixed layers, energy is completely transferred. Due to the combination of reflection and resonant transmission, the double-diffusive staircase acts as a filter on the vertical wavenumber spectrum of the internal waves, modifying the wave field reaching the deep ocean.

Reflected or partially reflected internal waves are shown to constructively interfere within the double-diffusive staircase, amplifying wave amplitudes by a factor of 2 to 3 relative to

a wave propagating through an equivalent stratification in which the staircase is absent. This constructive interference affects internal wave stability, which is assessed for convective overturning and shear instabilities. Near-inertial waves with vertical displacement amplitudes typical of the Western Arctic, $A_\eta \leq$ 1m based on the median wave amplitude determined from the ITP record, are found to be stable, consistent with the low levels of mixing directly estimated from microstructure and required to maintain a double-diffusive staircase.

A wave with a 2m amplitude will be shear unstable for most vertical wavelengths shorter than 50m, and a wave with a 5m amplitude will be unstable for nearly all wavelengths up to 100m. The fraction of measured near-inertial waves with an amplitude $A_\eta >$ 2m has increased from $\sim$5% of the wave field during 2005-2007 to $\sim$14% of the wave field during 2012-2014. This suggests that episodic mixing due to large internal waves has increased within the Atlantic Water layer in the Canada Basin.

While a typical internal wave in the Western Arctic Ocean will not produce mixing, intermittent generation of high-energy internal waves is occurring with increasing frequency, both during summer as the amount of open water increases and during winter as strong storms accelerate the increasingly thin, weak first-year sea-ice cover. This represents a significant shift in the internal wave field in the Arctic Ocean, likely to continue into the future as sea ice declines, with implications for vertical transport of heat and nutrients in the upper ocean.

5.2 Comparison with recent studies

The main results of this thesis are consistent with recent observations of internal waves in the Western Arctic Ocean. Martini et al. (2014) used mooring data from the Beaufort slope, and Cole et al. (2014) used data from an ITP equipped with a velocity sensor, and found elevated internal wave energy levels during summer and fall, and low energy during late winter, in agreement with the seasonal cycle for near-inertial waves determined from the ITP dataset.

Guthrie et al. (2013) found no trend in internal wave energy in the Beaufort Sea over the last 30 years, in agreement with the interannual changes for near-inertial waves from ITPs from 2005 to 2014. In particular, the amplitude of a typical near-inertial wave has risen

only slightly, remaining just under 1m for the median vertical displacement amplitude in the upper ocean. Corresponding vertical energy flux values for typical near-inertial frequencies and vertical wavelengths are in agreement with those previously observed by Halle and Pinkel (2003), from 0.02 to 0.15 mW m^{-1}.

The major change identified using the distribution of near-inertial wave amplitudes determined from the ITP dataset is the dramatic doubling of variance over the course of the record, caused by an increase in unusually large waves. The average value of diffusivity from Guthrie et al. (2013) is consistent with the median near-inertial wave amplitude from this research, and does not preclude an increase in episodic, high energy internal wave generation.

Halle and Pinkel (2003) observed significant but episodic upward propagation of internal waves in the Beaufort Sea, comparable in energy to the downward propagating waves, as did Cole et al. (2014) over a 6 month period in the Beaufort, and Fer (2014) in the Central Arctic. The presence of these energetic upward propagating waves has been attributed in part to interaction between the internal waves and the vorticity of the background mesoscale field. The predicted reflection of internal waves from the double-diffusive staircase stratification ubiquitous in these regions provides an alternative and more plausible explanation for the similar energy levels of upward and downward propagating internal waves.

5.3 Open questions and potential implications

Due to limitations of the Ice-Tethered Profiler instruments and of the theoretical investigation of internal wave propagation and stability, a number of key questions remain. The results of this thesis suggest possible avenues of inquiry and could guide further research efforts.

5.3.1 Spatial pattern

The spatial pattern in average near-inertial wave amplitude determined using the ITP dataset has not been fully explained. Larger and more energetic waves to the south of the Canada Basin could be a result of any one of a number of processes, or a combination thereof:

- Sea-ice characteristics. Measurements of sea-ice thickness covering all dates and locations sampled by the ITPs are not available, however it is known that thick multi-year ice accumulates to the northeast of the Canada Basin, along the Canada Arctic Archipelago, where waves are generally found to be smaller. Ice properties such as the distribution of floe sizes and ice roughness in the region surrounding an ITP are unknown, though likely variable in both space and time.

- Southern propagation. Near-inertial waves are constrained to propagate equatorward from their generation location. If turbulent dissipation in the under ice boundary layer has been reduced in recent years - due to fewer ice floes with deep, ridged keels for example - waves could experience multiple reflections from the sea ice at the surface, allowing them to propagate further across the Basin. Typical vertical group speeds for near-inertial waves are on the order of 50-100m/week in the upper ocean (Pinkel (2005) observed 30-50m/week), increasing to 500-1000m/week in the deep ocean. One round-trip to the ocean floor and back would take a few months. For typical horizontal wave group speed on the order of 10km/week, a near-inertial wave might only travel $\sim$100km laterally from its generation location before being dissipated in the under ice boundary layer, compared to Basin scale lateral propagation for multiple reflections.

- Reflection from the double-diffusive staircase. Near the slope in the Beaufort, and on the Basin peripheries near topography, increased mixing has partially eroded the stratified interfaces between mixed layers in the double-diffusive staircase. This reduced stratification was shown to increase reflection of wave energy flux into the upper ocean by limiting resonant tunnelling through the staircase. If more wave reflection is occurring in the southern Basin, approaching the slope, this could explain the larger waves observed there, although not necessarily the latitudinal trend across the central Basin.

- Interactions with the mesoscale. In the southwest Canada Basin, observations have shown numerous near-surface eddies, possibly generated near Barrow Canyon, and

fronts associated with coastal currents, Pacific Water, and river inflow (as well as an internal tide south of the M2 critical latitude). Near-inertial waves in an active mesoscale may have larger wave amplitudes, for example through resonant interactions with eddies (Kunze and Boss, 1998).

If sea-ice thickness is the cause of the latitudinal trend in wave amplitude, internal wave energy in the northeast of the Basin will continue to increase as multiyear ice is replaced by first-year ice. Future studies might investigate the longitudinal dependence in the near-inertial wave spatial pattern, which does not show a clear trend. One possibility is the use of multivariate analysis to separate the relative contributions of latitudinal, longitudinal, and temporal variations to the variance in the wave field.

Determining whether near-inertial waves are undergoing multiple reflections across the Basin requires observations able to resolve the frequency content of the wave field, to look for a broader spectral peak around the local inertial frequency for locations further south. Determining reflection from the double-diffusive staircase requires observations of near-inertial wave propagation with depth from the near-surface to below the staircase, to identify the direction of propagation and energy level of waves above and below the staircase.

ITPs are unable to accurately resolve the exact frequency or vertical wavelength of a particular near-inertial wave, making any calculation of group velocity or wave energy flux highly uncertain. As an example, a near-inertial wave with a vertical displacement amplitude of 1m, propagating through near-surface stratification with $N = 0.01\text{s}^{-1}$ at 75^oN, could have a vertical energy flux of $F_z = 0.2\text{mW/m}$ for $\omega = 1.01f$ and $\lambda_z = 100\text{m}$, or $F_z = 0.02\text{mW/m}$ for $\omega = 1.1f$ and $\lambda_z = 10\text{m}$, with no way to distinguish the two cases using ITP data.

The combination of internal wave theory and numerical solutions used in this thesis can be extended to axisymmetric or 2-D simulations to investigate internal waves propagating through known background shear such as that associated with an eddy, or to investigate wave-wave interactions. For observed stratification and velocity profiles, such an approach can provide physical intuition and suggest whether wave instability is to be expected and

at what depth. Increased mixing near the slope (either due to reflection off the staircase or interactions with the mesoscale) could have significant implications for vertical heat flux and biological productivity, if the inflowing warm, nutrient rich Pacific Water were mixed vertically up to the euphotic zone.

5.3.2 Sea ice properties and internal wave energy

From the ITP data, it was determined that unusually large near-inertial waves are increasingly common in both summer and winter, while inertial motion of the sea ice is increasing in summer, in response to declining ice cover. The agreement between seasonal variations in wind factor and near-inertial wave amplitude suggests that ice properties such as roughness and internal rigidity - which affect how readily the ice responds to wind forcing - are important to how much energy is available for internal wave generation. The actual impact of different sea-ice properties on momentum and energy transfer from the wind to ocean is poorly understood, including:

- Ocean surface stress. The stress caused by wind or sea-ice motion over the ocean's surface is related to the speed and the drag of the wind or ice. Air-ice and ice-ocean drag depends on ice roughness, internal ice stresses, and form drag. Work by Martin et al. (2014) showed that ocean surface stress in a climate model was higher when some sea ice was present relative to 100% open water. In fact, the seasonal cycle in ocean surface stress is quite similar to that for the near-inertial internal wave field (personal communication - T. Martin, 2015).

- Inertial frequency band. Most climate models do not resolve the inertial frequency band for sea-ice velocity or ocean currents. In addition, reanalysis wind products do not capture the inertial band in the Arctic. An increase in wind energy input into inertial ice motion during the summer months could increase inertial currents in the mixed layer, followed by mixed layer deepening and / or downward radiation of near-inertial internal waves.

Current modelling efforts are working to incorporate the inertial band into short climate model runs, determine the relative importance of different ice properties to ocean surface stress in different seasons, and understand how increased open water affects momentum flux into the ocean. Observational efforts, including those reported in Cole et al. (2014) using an ITP equipped with a velocity sensor, are looking at how mixed layer depth and currents vary after storm events, and how that energy is subsequently transferred into the internal wave field. It might be possible to determine an empirical equation for the relative importance of sea-ice concentration, ice speed, and wind speed to near-inertial wave amplitude as determined from ITP data on daily or weekly timescales, however any such relationship is likely to vary seasonally and in response to changing ice drag.

Understanding how wind energy drives mixed layer deepening and internal wave generation has implications for biological productivity and sea-ice melt. If the mixed layer deepens following a storm, additional nutrients (nitrogen in particular) may become available to sea-ice algae and increase primary productivity in the mixed layer, provided sufficient sunlight is available. When energy radiates downwards as near-inertial waves, phytoplankton could be impacted directly by the vertical displacement of isopycnals at the base of the euphotic zone caused by the passage of the wave. For example, a wave with a 5m vertical displacement amplitude will locally elevate the base of the euphotic zone by up to 5m over a 12 hour period (and lower it by up to 5m over the next 12 hours). Near-inertial waves can extend horizontally for tens to hundreds of kilometers and propagate vertically at speeds of 100m per week or less in the upper ocean, so that this effect could be significant intermittently.

5.3.3 Wave-stratification interactions

Predictions of internal wave reflection from the double-diffusive staircase and near-inertial wave instability within the staircase show that interactions between internal waves and the stratification are important. However, the 1-D theory used assumes a fixed stratification, and does not account for feedbacks between the waves and the stratification.

As an example, an increase in mixing within the staircase will reduce the strength of the

stratification in the interfaces between mixed layers, which was shown to reduce resonant wave tunnelling and increase reflection of wave energy into the upper ocean. A buildup of wave energy in the upper ocean increases the likelihood of wave-wave interactions causing instability and mixing. In the upper ocean, mixing might transport nutrients vertically toward the euphotic zone, or bring heat from the Pacific Water up towards the sea ice.

It may be possible to track changes in the coherence of the double-diffusive staircase in the Canada Basin in recent years, following the approach of Timmermans et al. (2008a). Individual layers within the staircase appear as distinct bands on a T-S diagram. Changes to the staircase would smear these bands, and could potentially be compared to periods of high near-inertial wave energy, though other processes such as the passage of eddies are also known to affect staircase structure.

An increase in mixing due to internal wave instabilities anywhere within the halocline will also weaken the strength of the stratification, making direct wind or buoyancy driven mixing more effective. Storms could more easily mix to the Pacific Water layer in the central Canada Basin, and to the Atlantic Water layer on the shelves or in the Eastern Arctic.

The energy flux associated with a large $A_\eta = 5$m amplitude near-inertial wave will be roughly $F_z = 0.5{-}5\text{mW/m}$, depending on vertical wavelength. Crudely estimating diffusivity from these energy fluxes assuming all the energy is evenly spread over 100m in the vertical gives $K \sim 10^{-4}\text{m}^2/\text{s}$, comparable to low-latitude values. No currently available datasets can confirm whether or not such episodic and highly energetic mixing events, caused by unusually large amplitude near-inertial waves, are occurring in the Western Arctic Ocean.

As always in the Arctic Ocean, this investigation has led to many new questions, which may be able to guide future observational, theoretical, and modelling efforts. The results presented in this thesis show an internal wave field closely tied to the rapidly changing sea ice and unusual stratification in the Western Arctic Ocean, and hint at many interesting interactions and feedbacks yet to be explored.

BIBLIOGRAPHY

Alford, M. H., 2003: Improved global maps and 54-year history of wind-work on ocean inertial motions. *Geophys. Res. Lett.*, **30 (8)**, doi:10.1029/2003GL018026.

Alford, M. H., M. F. Cronin, and J. M. Klymak, 2012: Annual cycle and depth penetration of wind-generated near-inertial internal waves at Ocean Station Papa in the Northeast Pacific. *J. Phys. Oceanogr.*, **42**, 889–909, doi:10.1175/JPO-D-11-092.1.

Andreas, E. L., T. W. Horst, A. A. Grachev, P. O. G. Persson, C. W. Fairall, P. S. Guest, and R. E. Jordan, 2010: Parametrizing turbulent exchange over summer sea ice and the marginal ice zone. *Q. J. R. Meteorol. Soc.*, **136**, 927–943, doi:10.1002/qj.618.

Ardyna, M., M. Babin, M. Gosselin, E. Devred, L. Rainville, and J.-E. Tremblay, 2014: Recent Arctic Ocean sea ice loss triggers novel fall phytoplankton blooms. *Geophysical Research Letters*, **41 (17)**, 6207–6212, doi:10.1002/2014GL061047.

Cavalieri, D., C. Parkinson, P. Gloersen, and H. J. Zwally, 1996, updated 2008: *Sea ice concentrations from Nimbus-7 SMMR and DMSP SSM/I passive microwave data*. Boulder, Colorado USA: National Snow and Ice Data Center, Digital media. pp.

Cole, S. T., M.-L. Timmermans, J. M. Toole, R. a. Krishfield, and F. T. Thwaites, 2014: Ekman veering, internal waves, and turbulence observed under Arctic sea ice. *J. Phys. Oceanogr.*, **44**, 1306–1328, doi:10.1175/JPO-D-12-0191.1.

Comiso, J. C., 2002: A rapidly declining perennial sea ice cover in the Arctic. *Geophys. Res. Lett.*, **29**, doi:10.1029/2002GL015650.

Comiso, J. C., C. L. Parkinson, R. Gersten, and L. Stock, 2008: Accelerated decline in the Arctic sea ice cover. *Geophys. Res. Lett.*, **35**, doi:10.1029/2007GL031972.

D'Asaro, E., 1982: Absorption of internal waves by the benthic boundary layer. *Journal of Physical Oceanography*, **12**, 323–336.

D'Asaro, E. A., 1985: The energy flux from the wind to near-inertial motions in the surface mixed layer. *J. Phys. Oceanogr.*, **15**, 1043–1059, doi:10.1175/1520-0485(1985)015.

D'Asaro, E. A., C. C. Eriksen, M. D. Levine, C. A. Paulson, P. Niiler, and P. Van Meurs, 1995: Upper-ocean inertial currents forced by a strong storm. Part I: Data and comparisons with linear theory. *Journal of Physical Oceanography*.

D'Asaro, E. A., and M. D. Morehead, 1991: Internal waves and velocity fine structure in the Arctic Ocean. *J. Geophys. Res.*, **96**, 12 725–12 738, doi:10.1029/91JC01071.

D'Asaro, E. A., and J. H. Morison, 1992: Internal waves and mixing in the Arctic Ocean. *Deep. Res. Part a-Oceanographic Res. Pap.*, **39**, S459–S484, doi:10.1016/s0198-0149(06)80016-6.

Dee, D. P., and Coauthors, 2011: The ERA-Interim reanalysis: configuration and performance of the data assimilation system. *Q. J. R. Meteorol. Soc.*, **137**, 553–597, doi:10.1002/qj.828.

Dosser, H. V., and L. Rainville, 2015: Dynamics of the changing near-inertial internal wave field in the arctic ocean. *Journal of Physical Oceanography*, in Revision.

Dosser, H. V., L. Rainville, and J. M. Toole, 2014: Near-inertial internal wave field in the Canada Basin from Ice-Tethered Profilers. *J. Phys. Oceanogr.*, **44 (2)**, 413–426, doi:10.1175/JPO-D-13-0117.1.

Eckart, C., 1961: Internal waves in the ocean. *Physics of Fluids*, **4**, 791–799.

Efron, B., and R. J. Tibshirani, 1993: *An Introduction to the Bootstrap*. Springer-Science+Business Media.

Egbert, G., and S. Erofeeva, 2002: Efficient inverse modeling of barotropic ocean tides. *J. Atmos. Ocean. Technol.*, **19 (2)**, 183–204.

Ekman, V. W., 1905: On the influence of the earth's rotation on ocean-currents. *Arkiv för matematik, astronomi och fysik*, **2 (11)**.

Emery, W. J., and R. E. Thompson, 1998: *Data Analysis Methods in Physical Oceanography.* Elsevier Science & Technology.

Fer, I., 2009: Weak vertical diffusion allows maintenance of cold halocline in the central Arctic. *Atmos. Ocean. Sci. Lett.*, **2 (3)**, 148–152.

Fer, I., 2014: Near-inertial mixing in the Central Arctic Ocean. *J. Phys. Oceanogr.*, **44**, 2031–2049, doi:10.1175/JPO-D-13-0133.1.

Fer, I., R. Skogseth, and F. Geyer, 2010: Internal waves and mixing in the Marginal Ice Zone near the Yermak Plateau. *J. Phys. Oceanogr.*, **40 (7)**, 1613–1630, doi: 10.1175/2010JPO4371.1.

Fritts, D., and P. Rastogi, 1985: Convective and dynamical instabilities due to gravity wave motions in the lower and middle atmosphere: Theory and observations. *Radio Sci.*, **20**, 1247–1277.

Fritts, D., and L. Yuan, 1989: An analysis of gravity wave ducting in the atmosphere: Eckart's resonances in thermal and doppler ducts. *Journal of Geophysical Research*, **94**, 18,455–18,466.

Garrett, C., 2001: What is the 'near-inertial' band and why is it different from the rest of the internal wave spectrum? *J. Phys. Oceanogr.*, **31**, 962–971, doi:10.1175/1520-0485(2001)031.

Garrett, C., and E. Kunze, 2007: Internal tide generation in the deep ocean. *Annu. Rev. Fluid Mech.*, **39**, 57–87, doi:10.1146/annurev.fluid.39.050905.110227.

Garrett, C., and W. Munk, 1972: Oceanic mixing by breaking internal waves. *Deep Sea Res.*, **19 (12)**, 823–832, doi:10.1016/0011-7471(72)90001-0.

Ghaemsaidi, S. J., T. Dauxois, S. Joubaud, P. Odier, and T. Peacock, 2015a: Forced internal waves in nonuniform stratications. *Physics of Fluids*, in Revision.

Ghaemsaidi, S. J., H. V. Dosser, L. Rainville, and T. Peacock, 2015b: The impact of multiple layering on internal wave transmission. *Journal of Fluid Mechanics*, in Revision.

Gimbert, F., N. C. Jourdain, D. Marsan, J. Weiss, and B. Barnier, 2012a: Recent mechanical weakening of the Arctic sea ice cover as revealed from larger inertial oscillations. *J. Geophys. Res. Ocean.*, **117**, doi:10.1029/2011JC007633.

Gimbert, F., D. Marsan, J. Weiss, N. C. Jourdain, and B. Barnier, 2012b: Sea ice inertial oscillations in the Arctic Basin. *Cryosphere*, **6**, 1187–1201, doi:10.5194/tc-6-1187-2012.

Gregg, M., E. D'Asaro, T. Shay, and N. Larson, 1986: Observations of persistent mixing and near-inertial internal waves. *Journal of Physical Oceanography*, **16**, 856–885.

Gregg, M. C., 1989: Scaling turbulent dissipation in the thermocline. *J. Geophys. Res.*, **94**, 9686, doi:10.1029/JC094iC07p09686.

Gregg, M. C., and E. Kunze, 1991: Shear and strain in Santa-Monica Basin. *Journal of Geophysical Research-Oceans*, **96 (C9)**, 16 709–16 719.

Guthrie, J. D., J. H. Morison, and I. Fer, 2013: Revisiting internal waves and mixing in the Arctic Ocean. *J. Geophys. Res.*, **118**, 3966–3977, doi:10.1002/jgrc.20294.

Hakkinen, S., A. Proshutinsky, and I. Ashik, 2008: Sea ice drift in the Arctic since the 1950s. *Geophys. Res. Lett.*, **35 (19)**, doi:10.1029/2008GL034791.

Halle, C., and R. Pinkel, 2003: Internal wave variability in the Beaufort Sea during the winter of 1993/1994. *J. Geophys. Res.*, **108**, doi:10.1029/2000JC000703.

Hebert, D., and J. N. Moum, 1994: Decay of a near-inertial wave. *Journal of Physical Oceanography*, **24**, 2334–2351.

Jackson, J. M., E. C. Carmack, F. A. McLaughlin, S. E. Allen, and R. G. Ingram, 2010: Identification, characterization, and change of the near-surface temperature maximum in the Canada Basin, 1993-2008. *Journal of Geophysical Research-Oceans*, **115**.

Jakobson, M., and et al., 2012: The International Bathymetric Chart of the Arctic Ocean (IBCAO) Version 3.0. *Geophysical Research Letters*, **39**, doi:10.1029/2012GL052219.

Johnson, G. C., J. M. Toole, and N. G. Larson, 2007: Sensor corrections for sea-bird SBE-41CP and SBE-41 CTDs. *Journal of Atmospheric and Oceanic Technology*, **24 (6)**, 1117–1130.

Johnson, H. L., and C. Garrett, 2004: Effects of noise on Thorpe scales and run lengths. *Journal of Physical Oceanography*, **34 (11)**, 2359–2372.

Kalnay, E., and Coauthors, 1996: The NCEP/NCAR 40-year reanalysis project. *Bull. Am. Meteorol. Soc.*, **77 (3)**, 437–471, doi:10.1175/1520-0477(1996)077.

Kanamitsu, M., W. Ebisuzaki, J. Woollen, S.-K. Yang, J. J. Hnilo, M. Fiorino, and G. L. Potter, 2002: NCEP-DOE AMIP-II Reanalysis (R-2). *Bull. Am. Meteorol. Soc.*, **83**, 1631–1643, doi:10.1175/BAMS-83-11-1631.

Kelley, D., 1984: Effective diffusivities within ocean thermohaline staircases. *Journal of Geophysical Research*, **89**, 10 484–10 488.

Kowalik, Z., and A. Y. Proshutinsky, 1994: The Arctic Ocean tides. *The Polar Oceans and Their Role in Shaping the Global Environment, Geophys. Monogr. Ser.*, **85**, 137–158.

Krishfield, R., J. Toole, A. Proshutinsky, and M. L. Timmermans, 2008: Automated Ice-Tethered Profilers for seawater observations under pack ice in all seasons. *J. Atmos. Ocean. Technol.*, **25 (11)**, 2091–2105, doi:10.1175/2008JTECHO587.1.

Krishfield, R., and Coauthors, 2006: Ice-Tethered Profilers for real-time seawater observations in the Polar Oceans. Technical report of the Woods Hole Oceanographic Institution. 81 pp.

Kunze, E., and E. Boss, 1998: A model for vortex-trapped internal waves. *Journal of Physical Oceanography*, **28**.

Kunze, E., A. Williams III, and B. M.G., 1990: Observations of shear and vertical stability from a neutrally buoyant float. *Journal of Geophysical Research*, **95**, 18 127– 18 142.

Leaman, K. D., and T. B. Sanford, 1975: Vertical energy propagation of inertial waves - vector spectral analysis of velocity profiles. *Journal of Geophysical Research*, **80 (15)**, 1975–1978.

Lenn, Y.-D., T. P. Rippeth, C. P. Old, S. Bacon, I. Polyakov, V. Ivanov, and J. Hölemann, 2011: Intermittent intense turbulent mixing under ice in the Laptev Sea Continental Shelf. *J. Phys. Oceanogr.*, **41**, 531–547, doi:10.1175/2010JPO4425.1.

Levine, M. D., C. A. Paulson, and J. H. Morison, 1985: Internal waves in the Arctic Ocean - Comparison with lower-latitude observations. *J. Phys. Oceanogr.*, **15**, 800–809, doi:10.1175/1520-0485(1985)015.

Levine, M. D., C. A. Paulson, and J. H. Morison, 1987: Observations of internal gravity waves under the Arctic pack ice. *J. Geophys. Res.*, **92**, 779, doi:10.1029/JC092iC01p00779.

Lighthill, M., 1978: *Waves in Fluids*. Cambridge University Press, Cambridge, MA, 504 pp.

Lindsay, R., and A. Schweiger, 2015: Arctic sea ice thickness loss determined using subsurface, aircraft, and satellite observations. *Cryosph.*, **9**, 269–283, doi:10.5194/tc-9-269-2015.

Lique, C., J. D. Guthrie, M. Steele, A. Proshutinsky, J. H. Morison, and R. Krishfield, 2014: Diffusive vertical heat flux in the Canada Basin of the Arctic Ocean inferred from

moored instruments. *Journal of Geophysical Research: Oceans*, **119 (1)**, 496–508, doi: 10.1002/2013JC009346.

Marmorino, G., and D. Caldwell, 1976: Heat and salt transport through a diffusive thermohaline interface. *Deep-Sea Research*, **23**, 59–67.

Martin, T., M. Steele, and J. Zhang, 2014: Seasonality and long-term trend of Arctic Ocean surface stress in a model. *J. Geophys. Res. Ocean.*, **119**, 1723–1738, doi: 10.1002/2013JC009425.

Martini, K. I., H. L. Simmons, C. A. Stoudt, and J. K. Hutchings, 2014: Near-inertial internal waves and sea ice in the Beaufort Sea. *J. Phys. Oceanogr.*, **44 (8)**, 2212–2234, doi:10.1175/JPO-D-13-0160.1.

Mathur, M., and T. Peacock, 2009: Internal wave beam propagation in non-uniform stratifications. *Journal of Fluid Mechanics*, **639**, 133, doi:10.1017/S0022112009991236.

McCabe, G. J., M. P. Clark, and M. C. Serreze, 2001: Trends in Northern Hemisphere surface cyclone frequency and intensity. *J. Clim.*, **14 (12)**, 2763–2768, doi:10.1175/1520-0442(2001)014.

McLaughlin, F. A., and E. C. Carmack, 2010: Deepening of the nutricline and chlorophyll maximum in the Canada Basin interior, 2003-2009. *Geophysical Research Letters*, **37**.

McLaughlin, F. A., E. C. Carmack, W. J. Williams, S. Zimmermann, K. Shimada, and M. Itoh, 2009: Joint effects of boundary currents and thermohaline intrusions on the warming of Atlantic water in the Canada Basin, 1993-2007. *Journal of Geophysical Research: Oceans*, **114 (C1)**, doi:10.1029/2008JC005001.

McPhee, M. G., and L. H. Kantha, 1989: Generation of internal waves by sea ice. *J. Geophys. Res.*, **94**, 3287, doi:10.1029/JC094iC03p03287.

Merrifield, M. A., and R. Pinkel, 1996: Inertial currents in the Beaufort Sea: Observations of response to wind and shear. *J. Geophys. Res.*, **101**, 6577, doi:10.1029/95JC03625.

Morison, J. H., C. E. Long, and M. D. Levine, 1985: Internal wave dissipation under sea ice. *J. Geophys. Res.*, **90**, 11 959, doi:10.1029/JC090iC06p11959.

Munk, W., and C. Wunsch, 1998: Abyssal recipes II: Energetics of tidal and wind mixing. *Deep Sea Research Part I Oceanographic Research Papers*, **45 (12)**.

Munk, W. H., 1966: Abyssal recipes. *Deep Sea Res.*, **13**, 707–730, doi:10.1016/0011-7471(66)90602-4.

Mysak, L., and M. Howe, 1976: A kinetic theory for internal waves in a randomly stratified fluid. *Dynamics of Atmospheres and Oceans*, **1**, 3–31, doi:http://dx.doi.org/10.1016/0377-0265(76)90003-8.

Mysak, L. A., 1978: Wave propagation in random media, with oceanic applications. *Reviews of Geophysics*, **16 (2)**, 233–261, doi:10.1029/RG016i002p00233.

Nault, J. T., and B. R. Sutherland, 2007: Internal wave transmission in nonuniform flows. *Physics of Fluids*, **19 (1)**, 016 601, doi:10.1063/1.2424791.

Nishino, S., Y. Kawaguchi, J. Inoue, T. Hirawake, A. Fujiwara, R. Futsuki, J. Onodera, and M. Aoyama, 2015: Nutrient supply and biological response to wind-induced mixing, inertial motion, internal waves, and currents in the northern Chukchi Sea. *Journal of Geophysical Research: Oceans*, **120 (3)**, 1975–1992, doi:10.1002/2014JC010407.

Overland, J. E., 2009: Meteorology of the Beaufort Sea. *Journal of Geophysical Research-Oceans*, **114**.

Padman, L., and T. M. Dillon, 1987: Vertical heat fluxes through the beaufort sea thermohaline staircase. *Journal of Geophysical Research: Oceans*, **92 (C10)**, 10 799–10 806, doi:10.1029/JC092iC10p10799.

Padman, L., and T. M. Dillon, 1988: On the horizontal extent of the Canada Basin thermohaline steps. *Journal of Physical Oceanography*, **18**, 1458–1462, doi:10.1175/1520-0485(1988)018¡1458:OTHEOT¿2.0.CO;2.

Padman, L., and T. M. Dillon, 1989: Thermal microstructure and internal waves in the Canada Basin diffusive staircase. *Deep Sea Research Part A. Oceanographic Research Papers*, **36 (4)**, 531–542, doi:10.1016/0198-0149(89)90004-6.

Padman, L., and S. Erofeeva, 2004: A barotropic inverse tidal model for the Arctic Ocean. *Geophys. Res. Lett.*, **31**, doi:10.1029/2003GL019003.

Palmer, M. A., G. L. van Dijken, B. G. Mitchell, B. J. Seegers, K. E. Lowry, M. M. Mills, and K. R. Arrigo, 2013: Light and nutrient control of photosynthesis in natural phytoplankton populations from the Chukchi and Beaufort seas, Arctic Ocean. *Limnology and Oceanography*, **58**, 2185–2205.

Pedlosky, J., 2003: *Waves in the Ocean and Atmosphere: Introduction to Wave Dynamics*. Springer, New York.

Peralta-Ferriz, C., and R. A. Woodgate, 2015: Seasonal and interannual variability of pan-Arctic surface mixed layer properties from 1979 to 2012 from hydrographic data, and the dominance of stratification for multiyear mixed layer depth shoaling. *Progress in Oceanography*, **134**, 19 – 53, doi:http://dx.doi.org/10.1016/j.pocean.2014.12.005.

Pinkel, R., 2005: Near-inertial wave propagation in the Western Arctic. *J. Phys. Oceanogr.*, **35**, 645–665, doi:10.1175/JPO2715.1.

Pinkel, R., 2008: The wavenumber-frequency spectrum of vortical and internal-wave shear in the Western Arctic Ocean. *Journal of Physical Oceanography*, **38**, 277–290, doi: http://dx.doi.org/10.1175/2006JPO3558.1.

Plueddemann, A. J., 1992: Internal wave observations from the Arctic environmental drifting buoy. *J. Geophys. Res.*, **97**, 12 619, doi:10.1029/92JC01098.

Plueddemann, A. J., R. Krishfield, T. Takizawa, K. Hatakeyama, and S. Honjo, 1998: Upper ocean velocities in the Beaufort Gyre. *Geophys. Res. Lett.*, **25 (2)**, 183–186, doi: 10.1029/97GL53638.

Polzin, K., 1996: Statistics of the Richardson number: Mixing models and fine structure. *Journal of Physical Oceanography*, **26**, 1409–1425.

Proshutinsky, A., and Coauthors, 2009: Beaufort Gyre freshwater reservoir: State and variability from observations. *Journal of Geophysical Research-Oceans*, **114**.

Rainville, L., C. M. Lee, and R. A. Woodgate, 2011: Impact of wind-driven mixing in the Arctic Ocean. *Oceanography*, **24 (3)**, 136–145.

Rainville, L., and P. Winsor, 2008: Mixing across the Arctic ocean: Microstructure observations during the Beringia 2005 expedition. *Geophys. Res. Lett.*, **35**, doi: 10.1029/2008gl033532.

Rainville, L., and R. A. Woodgate, 2009: Observations of internal wave generation in the seasonally ice-free Arctic. *Geophys. Res. Lett.*, **36**, doi:10.1029/2009GL041291.

Rampal, P., J. Weiss, and D. Marsan, 2009: Positive trend in the mean speed and deformation rate of Arctic sea ice, 1979-2007. *J. Geophys. Res. Ocean.*, **114**, doi:10.1029/2008JC005066.

Rigor, I. G., J. M. Wallace, and R. L. Colony, 2002: Response of sea ice to the Arctic Oscillation. *Journal of Climate*, **15**, 2648–2663.

Rippeth, T. P., B. J. Lincoln, Y.-D. Lenn, J. A. M. Green, A. Sundfjord, and S. Bacon, 2015: Tide-mediated warming of Arctic halocline by Atlantic heat fluxes over rough topography. *Nature Geoscience*, **8**, 191–194, doi:10.1038/ngeo2350.

Rothrock, D. A., D. B. Percival, and M. Wensnahan, 2008: The decline in Arctic sea-ice thickness: Separating the spatial, annual, and interannual variability in a quarter century of submarine data. *J. Geophys. Res.*, **113**, doi:10.1029/2007jc004252.

Rudels, B., N. Kuzmina, U. Schauer, T. Stipa, and V. Zhurbas, 2009: Double-diffusive convection and interleaving in the Arctic Ocean - Distribution and importance. *Geophysica*, **45**, 199–213.

Serreze, M. C., F. Carse, R. G. Barry, and J. C. Rogers, 1997: Icelandic low cyclone activity: climatological features, linkages with the NAO, and relationships with recent changes in the northern hemisphere circulation. *J. Clim.*, **10**, 453–464.

Serreze, M. C., M. M. Holland, and J. Stroeve, 2007: Perspectives on the Arctic's shrinking sea-ice cover. *Science*, **315**, 1533–1536, doi:10.1126/science.1139426.

Shimada, K., T. Kamoshida, M. Itoh, S. Nishino, E. Carmack, F. McLaughlin, S. Zimmermann, and A. Proshutinsky, 2006: Pacific Ocean inflow: Influence on catastrophic reduction of sea ice cover in the Arctic Ocean. *Geophysical Research Letters*, **33**, doi: 10.1029/2005GL025624.

Simmons, H. L., R. W. Hallberg, and B. K. Arbic, 2004: Internal wave generation in a global baroclinic tide model. *Deep. Res. Part II Top. Stud. Oceanogr.*, Vol. 51, 3043–3068, doi:10.1016/j.dsr2.2004.09.015.

Spreen, G., R. Kwok, and D. Menemenlis, 2011: Trends in Arctic sea ice drift and role of wind forcing: 1992-2009. *Geophys. Res. Lett.*, **38**, doi:10.1029/2011GL048970.

Steele, M., W. Ermold, and J. Zhang, 2011: Modeling the formation and fate of the near-surface temperature maximum in the Canadian Basin of the Arctic Ocean. *Journal of Geophysical Research-Oceans*, **116**.

Steele, M., R. Morley, and W. Ermold, 2001: PHC: A global ocean hydrography with a high-quality Arctic Ocean. *Journal of Climate*, **14**, 2079–2087.

Stroeve, J. C., V. Kattsov, A. Barrett, M. Serreze, T. Pavlova, M. Holland, and W. N. Meier, 2012: Trends in Arctic sea ice extent from CMIP5, CMIP3 and observations. *Geophys. Res. Lett.*, **39**, doi:10.1029/2012GL052676.

Sutherland, B. R., 2010: *Internal Gravity Waves*. Cambridge University Press, Cambridge, MA, 394 pp.

Sutherland, B. R., and K. Yewchuk, 2004: Internal wave tunnelling. *Journal of Fluid Mechanics*, **511**, 125–134, doi:10.1017/S0022112004009863.

Thorndike, A. S., and R. Colony, 1982: Sea ice motion in response to geostrophic winds. *Journal of Geophysical Research*, **87**, 5845–5852.

Thorpe, S. A., 1977: Turbulence and mixing in a Scottish Loch. *Philosophical Transactions of the Royal Society of London. Series A, Mathematical and Physical Sciences*, **286 (1334)**, 125–181, doi:10.1098/rsta.1977.0112.

Timmermans, M., L. Rainville, L. Thomas, and A. Proshutinsky, 2010: Moored observations of bottom-intensified motions in the deep Canada Basin, Arctic Ocean. *Journal of Marine Research*, **68 (3-4)**, 625–641, doi:10.1357/002224010794657137.

Timmermans, M. L., J. Toole, R. Krishfield, and P. Winsor, 2008a: Ice-Tethered Profiler observations of the double-diffusive staircase in the Canada Basin thermocline. *Journal of Geophysical Research-Oceans*, **113**.

Timmermans, M. L., J. Toole, A. Proshutinsky, R. Krishfield, and A. Plueddemann, 2008b: Eddies in the Canada Basin, Arctic Ocean, observed from Ice-Tethered Profilers. *Journal of Physical Oceanography*, **38 (1)**, 133–145.

Toole, J. M., R. A. Krishfield, M.-L. Timmermans, and A. Proshutinsky, 2011: The Ice-Tethered Profiler: Argo of the Arctic. *Oceanography*, **24 (3)**, 126–135.

Toole, J. M., M. L. Timmermans, D. K. Perovich, R. a. Krishfield, a. Proshutinsky, and J. a. Richter-Menge, 2010: Influences of the ocean surface mixed layer and thermohaline stratification on Arctic Sea ice in the central Canada Basin. *J. Geophys. Res. Ocean.*, **115**, 1–14, doi:10.1029/2009JC005660.

Tremblay, J.-E., and J. Gagnon, 2009: The effects of irradiance and nutrient supply on the productivity of Arctic waters: a perspective on climate change. *Influence of Climate Change on the Changing Arctic and Sub-Arctic Conditions*, J. C. Nihoul, and A. G. Kostianoy, Eds., NATO Science for Peace and Security Series C: Environmental Security, Springer Netherlands, 73–93.

Tremblay, J.-E., K. Simpson, J. Martin, L. Miller, Y. Gratton, D. Barber, and N. M. Price, 2008: Vertical stability and the annual dynamics of nutrients and chlorophyll fluorescence in the coastal, southeast Beaufort Sea. *Journal of Geophysical Research: Oceans*, **113 (C7)**, doi:10.1029/2007JC004547.

Turner, J., 1968: The behaviour of a stable salinity gradient heated from below. *Journal of Fluid Mechanics*, **33**, 183–200.

Turner, J., 2010: The melting of ice in the Arctic Ocean: The influence of double-diffusive transport of heat from below. *Journal of Physical Oceanography*, doi: 10.1175/2009JPO4279.1.

Wadhams, P., 2000: *Ice in the Ocean*. Gordon and Breach Science Publishers, Amsterdam.

Walsh, D., and E. Carmack, 2003: The nested structure of Arctic thermohaline intrusions. *Ocean Modelling*, **5 (3)**, 267–289.

Walsh, J. J., and et al., 1989: Carbon and nitrogen cycling within the Bering Chukchi Seas - Source regions for organic matter effecting AOU demands of the Arctic Ocean. *Progress in Oceanography*, **22**, 277–359.

Waterhouse, A. F., and Coauthors, 2014: Global patterns of diapycnal mixing from measurements of the turbulent dissipation rate. *J. Phys. Oceanogr.*, **44 (7)**, 1854–1872, doi: 10.1175/JPO-D-13-0104.1.

Woodgate, R. A., T. Weingartner, and R. Lindsay, 2010: The 2007 Bering Strait oceanic heat flux and anomalous Arctic sea-ice retreat. *Geophysical Research Letters*, **37**.

Wunsch, C., and R. Ferrari, 2004: Vertical Mixing, Energy, and the General Circulation of the Oceans. *Annu. Rev. Fluid Mech.*, **36**, 281–314, doi: 10.1146/annurev.fluid.36.050802.122121.

Yang, J., J. Comiso, D. Walsh, R. Krishfield, and S. Honjo, 2004: Storm-driven mixing and potential impact on the Arctic Ocean. *Journal of Geophysical Research: Oceans*, **109**, doi:10.1029/2001JC001248.

Zhang, J., and M. Steele, 2007: Effect of vertical mixing on the Atlantic Water layer circulation in the Arctic Ocean. *J. Geophys. Res.*, **112**, doi:10.1029/2006JC003732.

Zhang, X., J. E. Walsh, J. Zhang, U. S. Bhatt, and M. Ikeda, 2004: Climatology and interannual variability of Arctic cyclone activity: 1948-2002. *J. Clim.*, **17 (12)**, 2300–2317, doi:10.1175/1520-0442(2004)017.